

# Advances in lithium niobate photonics: development status and perspectives

Guanyu Chen<sup>1</sup>,<sup>a</sup> Nanxi Li,<sup>b</sup> Jun Da Ng,<sup>a</sup> Hong-Lin Lin,<sup>a</sup> Yanyan Zhou<sup>1</sup>,<sup>b</sup> Yuan Hsing Fu<sup>1</sup>,<sup>b</sup> Lennon Yao Ting Lee,<sup>b</sup> Yu Yu,<sup>c,\*</sup> Ai-Qun Liu,<sup>d</sup> and Aaron J. Danner<sup>1</sup>,<sup>a,\*</sup>

<sup>a</sup>National University of Singapore, Department of Electrical and Computer Engineering, Singapore

<sup>b</sup>A\*STAR (Agency for Science, Technology and Research), Institute of Microelectronics, Singapore

<sup>c</sup>Huazhong University of Science and Technology, School of Optical and Electronic Information, Wuhan National Laboratory for Optoelectronics, Wuhan, China

<sup>d</sup>Nanyang Technological University, Quantum Science and Engineering Centre, Singapore

**Abstract.** Lithium niobate (LN) has experienced significant developments during past decades due to its versatile properties, especially its large electro-optic (EO) coefficient. For example, bulk LN-based modulators with high speeds and a superior linearity are widely used in typical fiber-optic communication systems. However, with ever-increasing demands for signal transmission capacity, the high power and large size of bulk LN-based devices pose great challenges, especially when one of its counterparts, integrated silicon photonics, has experienced dramatic developments in recent decades. Not long ago, high-quality thin-film LN on insulator (LNOI) became commercially available, which has paved the way for integrated LN photonics and opened a hot research area of LN photonics devices. LNOI allows a large refractive index contrast, thus light can be confined within a more compact structure. Together with other properties of LN, such as nonlinear/acousto-optic/pyroelectric effects, various kinds of high-performance integrated LN devices can be demonstrated. A comprehensive summary of advances in LN photonics is provided. As LN photonics has experienced several decades of development, our review includes some of the typical bulk LN devices as well as recently developed thin film LN devices. In this way, readers may be inspired by a complete picture of the evolution of this technology. We first introduce the basic material properties of LN and several key processing technologies for fabricating photonics devices. After that, various kinds of functional devices based on different effects are summarized. Finally, we give a short summary and perspective of LN photonics. We hope this review can give readers more insight into recent advances in LN photonics and contribute to the further development of LN related research.

Keywords: lithium niobate; etching; photonics; integrated optics; nanotechnology; devices.

Received Jan. 16, 2022; revised manuscript received Apr. 12, 2022; accepted for publication Apr. 26, 2022; published online Jun. 8, 2022.

© The Authors. Published by SPIE and CLP under a Creative Commons Attribution 4.0 International License. Distribution or reproduction of this work in whole or in part requires full attribution of the original publication, including its DOI.

[DOI: [10.1117/1.AP.4.3.034003](https://doi.org/10.1117/1.AP.4.3.034003)]

## 1 Introduction

Lithium niobate ( $\text{LiNbO}_3$ , LN) is one of the most important artificial materials and has been widely used in the photonics area since it was first discovered to have a ferroelectric property in 1949.<sup>1</sup> Compared with other material systems, LN has various superior characteristics, such as a wide transparency window (400 nm to 5  $\mu\text{m}$ ) and large electro-optic (EO)/nonlinear-optic

(NLO)/acousto-optic (AO)/pyroelectric coefficients, as well as stable chemical and physical properties.<sup>2-9</sup> Based on these effects, various kinds of photonics devices have been demonstrated. For example, the large EO property of LN can be used for the realization of high-speed modulators. As there is no carrier dynamic process involved, such as the case in its counterparts including silicon (Si)<sup>10</sup> and indium phosphide (InP),<sup>11</sup> both the speed and linearity of LN modulators show advantages compared with other kinds of modulators. Therefore, in current fiber-optic communication systems, LN-based modulators have been widely used.<sup>3</sup> The second- and third-order nonlinear effects

\*Address all correspondence to Yu Yu, [yuyu@mail.hust.edu.cn](mailto:yuyu@mail.hust.edu.cn); Aaron J. Danner, [adanner@nus.edu.sg](mailto:adanner@nus.edu.sg)

in LN can also be used for various nonlinear optic conversions, covering both classical and quantum application scenarios.<sup>12–15</sup> Other properties of LN are also widely utilized for fabricating high-performance functional devices.<sup>16–18</sup>

For LN photonics, one of the challenges is how to effectively confine the light and thus enhance its interaction with the LN crystal. In a typical bulk LN (planar device), light is confined inside a planar waveguide formed by ion-in diffusion or proton exchange (PE).<sup>19–21</sup> In such a method, the refractive index contrast is usually very small ( $\sim 0.02$ ), therefore bulk LN-based devices have a large feature size and relatively poor performance even though they have been successfully used for decades. The problem of a poor index contrast hampers further development of LN photonics as high power and large device sizes are not compatible with desired trends in energy efficiency and integration. In the meantime, integrated platforms, such as silicon photonics,<sup>22–28</sup> have gotten more attention as silicon photonics in particular has become one of LN's strongest competitors due to its complementary metal oxide semiconductor (CMOS) compatibility, even though it lacks EO effects. This situation may yet change, though, as high-quality thin film LN (TFLN) with a controlled thickness has become available through the lapping and polishing<sup>29,30</sup> and crystal ion slicing (CIS) methods.<sup>8,9</sup> These high-quality TFLNs can be bonded onto an insulator with a lower refractive index (such as silicon oxide), and then an LN on insulator (LNOI) structure similar to silicon on insulator (SOI) is realized. The principal benefit from the large refractive index contrast of LNOI is that much more compact devices

can be integrated on the same single chip by patterning three-dimensional (3D) structures using various developed etching technologies.<sup>31–33</sup> In addition, TFLN can also be bonded to other material platforms that are lithographically patterned, where LN serves as a thin layer of unpatterned film and the light from waveguides or devices fabricated in the bonded platform interacts with it.<sup>34,35</sup> Relying on developed processing technologies, LN-based photonics devices with a high performance, especially integrated devices, have experienced a rapid development during recent years and many different structures for various application scenarios have been demonstrated,<sup>2–9</sup> showing that an era of LN photonics is coming.

In this review, we try to comprehensively summarize recent advances of LN photonics. The content of this review is not only focused on the integrated LN photonics devices that have appeared in recent years, but rather some bulk LN-based devices and related processing technologies; in this way, the research community can reach a better, comprehensive understanding of the technology evolution of LN photonics. We hope readers may be inspired by this review and then contribute to the further development of LN photonics. This review is organized as follows. In Sec. 2, we first introduce the material properties of LN, which form the basis of different kinds of applications. Then, we introduce several key processing technologies of LN photonics in Sec. 3. In Sec. 4, various kinds of functional devices are demonstrated, ranging from passive to active and innovative devices. Last, we give a summary and outlook of LN photonics. An illustration of the overall content of this review is shown in Fig. 1.

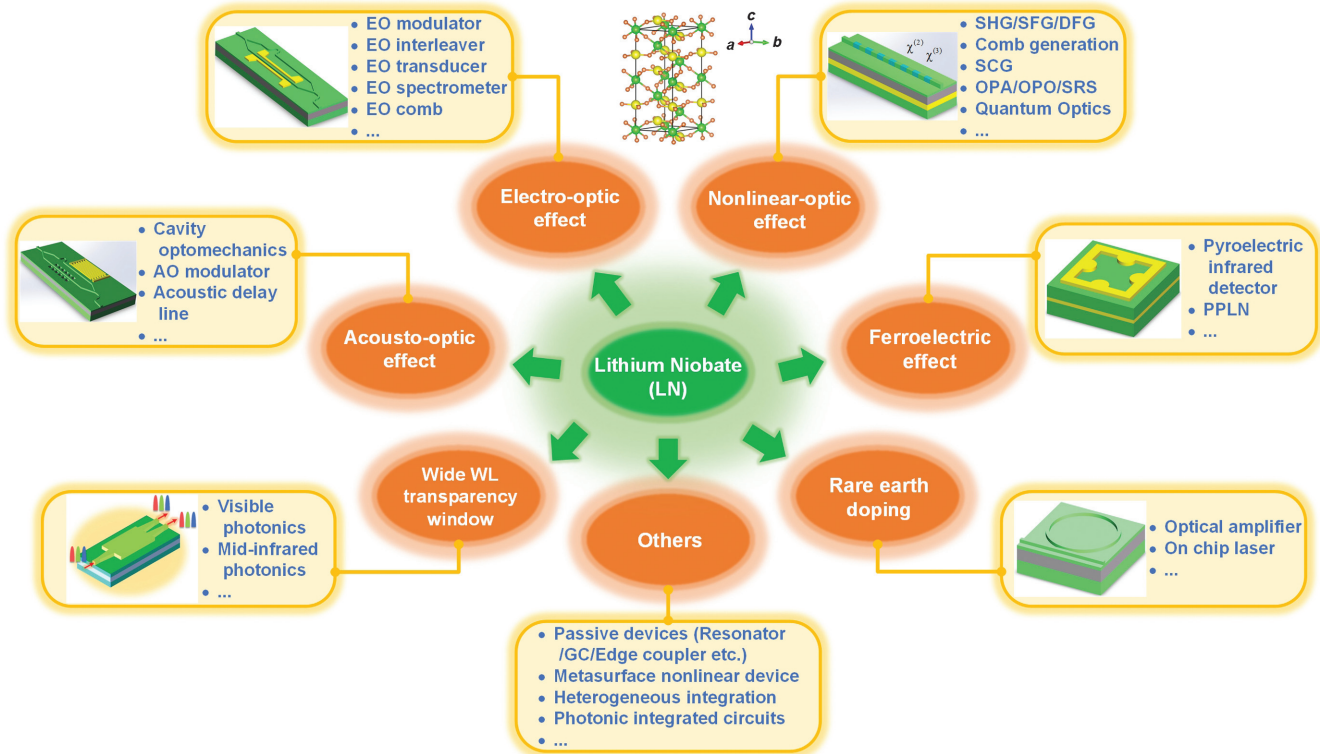


**Fig. 1** Overview of LN photonics. Top middle inset is LN crystal structure. EO, electro-optic; SHG, second harmonic generation; SFG/DFG, sum/difference frequency generation; SCG, super-continuum generation; OPA/OPO, optical parametric amplification/oscillation; SRS, stimulated Raman scattering; PPLN, periodically poled lithium niobate; GC, grating coupler; WL, wavelength; AO, acousto-optic.

## 2 Material Properties

LN does not exist in the natural world and is a purely artificial inorganic material. It is composed of lithium, niobium, and oxygen. People usually refer to LN as a distorted perovskite type of crystal. In 1966, Bell Labs demonstrated single crystal LN and analyzed its material properties comprehensively.<sup>36–40</sup> LN has a trigonal crystal structure (as shown in Fig. 1; top middle inset) and lacks inversion symmetry. There are many unique features of LN, such as a wide operational wavelength window, electro-optic (Pockels) effect, nonlinear optical polarizability, AO effect, rare earth doping possibility, pyroelectric effect, etc. These effects can be used for various applications, especially in photonics devices.

### 2.1 Basic Properties

LN is a birefringent crystal, and its ordinary ( $n_o$ ) and extraordinary ( $n_e$ ) refractive indices are 2.341 and 2.2547 at 500 nm wavelength,<sup>41</sup> respectively. It has a wide wavelength transparency window, covering from the visible (400 nm) to the mid-infrared (5  $\mu\text{m}$ ),<sup>42</sup> which makes it an attractive platform for many different applications. In the visible range, some applications, such as frequency metrology, quantum communication/computation, and light detection and ranging (LiDAR), can be realized based on the LN platform.<sup>42</sup> While in the short infrared range, especially near 1550 nm which is important for telecommunications, LN has been widely used for light modulation based on both bulk LN and TFLN.<sup>31,43</sup> For longer infrared wavelengths, some nonlinear optic conversions can be realized

using LN.<sup>44</sup> Ferroelectric LN has a large bandgap, which is calculated to be about 4.71 eV.<sup>45</sup> A summary of LN material properties is shown in Table 1. Some details of these properties will be discussed in the remaining subsections and more details related to functional devices that exploit the various properties shown in Table 1 can be found in Sec. 4.

### 2.2 Electro-Optic Properties

In an anisotropic material, the coefficients of the impermeability tensor  $(1/n^2)_i$ , which change with increasing electric field strength, can be described by Eq. (1), where  $r_{ij}$  are known as the EO coefficients. As LN is a class 3m (ditrigonal-pyramidal) crystal, the EO coefficients can be described according to Eq. (2). The largest ( $z$ -oriented) refractive index changes with respect to an applied ( $z$ -oriented) voltage can be described by Eq. (3), where  $n_e$  is the extraordinary refractive index and  $E_z$  is the applied positive electrical field. As the relation between the refractive index change and the applied electrical field is linear, such an effect is also recognized as a linear EO effect or Pockels effect. By controlling the direction of the electric field, either an increase or a decrease in refractive index change can be obtained. For LN,  $r_{33}$  ( $\sim 30.9$  pm/V) is most widely used for the design of EO devices,<sup>41</sup> and this relatively high value is one of its main advantages. Many different kinds of modulators and EO tuning devices are reported based on such a property:<sup>31,52</sup>

$$\Delta\left(\frac{1}{n^2}\right)_i = \sum_j r_{ij} E_j, \quad (1)$$

**Table 1** Material property summary of LN.

Category	Typical values/characteristics	Reference
Crystal structure	Trigonal	38
Refractive index	$n_o/n_e$ : 2.341/2.2547 @ 500 nm	41
Transparency window	400 to 5000 nm	42
Bandgap	4.71 eV	45
Electro-optic coefficients	$r_{13} = 9.6$ pm/V; $r_{22} = 6.8$ pm/V; $r_{33} = 30.9$ pm/V; $r_{42} = 32.6$ pm/V	41
Second-order nonlinear susceptibility	$d_{22}$ (1.058 $\mu\text{m}$ ) = $2.46 \pm 0.23$ pm/V; $d_{31}$ (1.058 $\mu\text{m}$ ) = $-4.64 \pm 0.66$ pm/V; $d_{33}$ (1.058 $\mu\text{m}$ ) = $-41.7 \pm 7.8$ pm/V	46
Third-order nonlinear susceptibility	$\chi^{(3)}$ = $(0.61 \pm 0.092) \times 10^4$ pm <sup>2</sup> /V <sup>2</sup> @ 1.047 $\mu\text{m}$	47
Photo-elastic constants	$p_{11} = -0.026$ ; $p_{12} = 0.09$ ; $p_{13} = 0.133$ ; $p_{14} = -0.075$ ; $p_{31} = 0.179$ ; $p_{33} = 0.071$ ; $p_{41} = -0.151$ ; $p_{44} = 0.146$ (dimensionless)	2
Pyroelectric coefficient	$-4 \times 10^{-9}$ C $\cdot$ cm <sup>-2</sup> $\cdot$ °C <sup>-1</sup> at 25°C	48
Thermal conductivity	$\sim 5.234$ W/(m $\cdot$ K) ( $a$ - or $c$ -oriented)	49
Thermo-optic coefficient	$\sim 2.5 \times 10^{-6}$ K <sup>-1</sup> (337 K, 1523 nm, ordinary) $\sim 4 \times 10^{-5}$ K <sup>-1</sup> (337 K, 1523 nm, extraordinary) <sup>a</sup>	50
Piezoelectric strain coefficients	$d_{15} = 6.8 \times 10^{-11}$ C $\cdot$ N <sup>-1</sup> ; $d_{22} = 2.1 \times 10^{-11}$ C $\cdot$ N <sup>-1</sup> ; $d_{31} = -0.1$ C $\cdot$ N <sup>-1</sup> ; $d_{33} = 0.6$ C $\cdot$ N <sup>-1</sup>	51

<sup>a</sup>Extracted from the measured data shown in the figures of Ref. 50.

$$r_{ij} = \begin{bmatrix} 0 & -r_{22} & r_{13} \\ 0 & r_{22} & r_{13} \\ 0 & 0 & r_{33} \\ 0 & r_{42} & 0 \\ r_{42} & 0 & 0 \\ r_{22} & 0 & 0 \end{bmatrix}, \quad (2)$$

$$\Delta n = -\frac{1}{2} n_e^3 r_{33} E_z. \quad (3)$$

### 2.3 Nonlinear Optic Properties

Another attractive property of LN is its high second- ( $\chi^{(2)}$ ) and third-order ( $\chi^{(3)}$ ) nonlinear susceptibilities. The second-order non-susceptibility of LN can be described by the two dimensional (2D) matrix shown in Eq. (4), where  $P_x, P_y, P_z$  are the electric polarization components,  $E_x, E_y, E_z$  are the electric field components, and  $d_{ij}$  are the second-order nonlinear susceptibility coefficients. For LN, typical values of  $d_{22}, d_{31}$ , and  $d_{33}$  are 2.46,  $-4.64$ , and  $-41.7$  pm/V,<sup>46</sup> respectively. In addition, the third-order nonlinearity coefficient ( $\chi^{(3)}$ ) of LN is estimated to be around  $(0.61 \pm 0.092) \times 10^4$  pm<sup>2</sup>/V<sup>2</sup>.<sup>47</sup> Both the high second- and third-order nonlinearities make LN an attractive platform for various kinds of applications, such as second harmonic generation (SHG),<sup>12,13,53–66</sup> sum frequency generation (SFG),<sup>67,68</sup> difference frequency generation (DFG),<sup>44</sup> third harmonic generation (THG),<sup>62,69</sup> optical parametric amplification/oscillation (OPA/OPO),<sup>70,71</sup> stimulated Raman scattering (SRS),<sup>72,73</sup> frequency comb,<sup>74–77</sup> supercontinuum generation (SCG),<sup>64,78,79</sup> and photon pair generation.<sup>80–83</sup> Section 4 discusses these applications in detail.

$$\begin{pmatrix} P_x \\ P_y \\ P_z \end{pmatrix} = 2 \times \begin{pmatrix} 0 & 0 & 0 & 0 & d_{31} & -d_{22} \\ -d_{22} & d_{22} & 0 & d_{31} & 0 & 0 \\ d_{31} & d_{31} & d_{33} & 0 & 0 & 0 \end{pmatrix} \begin{pmatrix} E_x^2 \\ E_y^2 \\ E_z^2 \\ 2E_z E_y \\ 2E_z E_x \\ 2E_x E_y \end{pmatrix}. \quad (4)$$

### 2.4 Acousto-Optic Properties

When acoustic waves pass through a medium, they will cause elongation and local compression of the medium to produce elastic strain. The strain changes periodically with space and time, causing a medium to appear dense and then rare, just like a phase grating. Diffraction will appear when light passes through such a medium disturbed by acoustic waves, which is known as the AO effect (sometimes, it is also regarded as the photoelastic effect). The anisotropic AO relationship between the strain and the refractive index can be described by Eq. (5),<sup>2</sup> where  $\Delta(1/n^2)_{ij}$  is a second rank tensor describing the refractive index change,  $S_{kl}$  is the second rank strain tensor, and  $p_{ijkl}$  is the fourth rank AO/photoelastic tensor. The detailed

photoelastic coefficients of LN are shown in Table 1. The large photoelastic coefficients of LN together with its significant piezoelectric effect (for efficient acoustic waves launching) make multiphysics functional devices possible, such as AO modulators. Different from EO modulators, an AO modulator has band-pass frequency selectivity, which can complement low pass EO modulators:

$$\Delta\left(\frac{1}{n^2}\right)_{ij} = \sum_{k,l} p_{ijkl} S_{kl}. \quad (5)$$

### 2.5 Ferroelectric Properties

LN was reported to have ferroelectric properties as early as 1949,<sup>1</sup> which means it exhibits spontaneous polarization characteristics with a nonzero electric dipole moment when there is no external electrical field. Such a property is commonly used for photonics application. For example, periodically inverting the crystal polarization direction of LN by applying a high electric field ( $\sim 22$  kV/mm) to form periodically poled LN (PPLN) can be used for improving nonlinear conversion (examples are discussed in Sec. 4.3).<sup>80</sup> For ferroelectric materials such as LN, the relationship between temperature variation and polarization intensity is usually described by the pyroelectric effect.<sup>2</sup> In a pyroelectric crystal, varying the temperature will modify the positions of the atoms within the crystal structure; thus, its spontaneous material polarization will change correspondingly. Such a change in polarization state will result in a voltage rise across the crystal.<sup>2</sup> If two surfaces (such as the top and bottom surfaces of Z-cut LN) of a crystal are covered with electrodes, there can be a current in the externally connected circuit. Such a current is proportional to the rate of temperature change and can be described by Eq. (6),<sup>84</sup> where  $I$  is the current,  $P(T)$  is the pyroelectric coefficient,  $A$  is the surface area, and  $dT/dt$  is the temperature change rate. For LN,  $P(T)$  was measured to be  $-4 \times 10^{-9}$  C · cm<sup>-2</sup> · °C<sup>-1</sup> at 25°C.<sup>48</sup> An intrinsically high pyroelectric coefficient in LN makes it a suitable platform for low cost and uncooled pyroelectrical photodetectors.

$$I = P(T)A \frac{dT}{dt}. \quad (6)$$

### 2.6 Thermo-Optic Properties

The thermal-optic (TO) coefficient of LN can be described by Eq. (7),<sup>50</sup> where  $n_i$  is the refractive index ( $i = o$  represents ordinary,  $i = e$  represents extraordinary),  $T$  is the temperature,  $\lambda_L$  is the wavelength,  $l$  is the etalon length,  $\Delta T_{\pi/2}$  is the temperature variation needed for complete detuning of the optical cavity, and  $\alpha(T)$  is the thermal expansion of LN along the light propagation direction. Due to the birefringence property of LN, the thermal optical coefficient of LN is different for ordinary and extraordinary light. According to one measured result,<sup>50</sup> the thermal optical coefficients of LN at around 337 K and 1523 nm are about  $2.5 \times 10^{-5}$  and  $4 \times 10^{-5}$  K<sup>-1</sup> for ordinary and extraordinary light, respectively. The thermal conductivity of LN can be calculated according to Eq. (8), where  $\kappa$  is the thermal conductivity,  $\rho$  is the density,  $C_p$  is the specific heat, and  $\eta$  is the thermal diffusion coefficient. The thermal conductivity of LN is also crystal orientation dependent. However, the difference is

too small to distinguish. A typical value of thermal conductivity for either *a*- or *c*-oriented LN is around 5.234 W/(m · K).<sup>49</sup> Although these properties are not the highest among other materials, the TO effect in LN has still attracted some attention as it has a higher tuning efficiency and superior DC stability than the EO effect.<sup>85–87</sup> Slower TO effect-based devices can be good complements to EO devices, especially in some areas where switching speed is not the primary consideration, such as in the case during calibration or tuning. One example is that the thermal tuning blocks can be used as phase shifters to control modulation bias points of an IQ modulator.<sup>88</sup> For TFLN devices, the thermal tuning efficiency can also be improved by etching away underlying oxide.<sup>85,87</sup> With the development of integrated LN photonics, TO-based devices will have more and more application scenarios.

$$\frac{dn_i}{dT} = \frac{\lambda_L}{4\Delta T_{\pi/2}} n_i \alpha(T), \quad (7)$$

$$\kappa = \rho C_p \eta. \quad (8)$$

## 2.7 Rare Earth Doping

Rare earth ions are solid state emitters with stable optical transitions with long lifetimes, making them good gain materials for optical amplification and lasers.<sup>89</sup> In a typical fiber optic communication system, the silica fiber is doped with rare earth ions to form a fiber-optic amplifier/laser. Recently, rare earth doped integrated lasers, including different rare earth elements and laser cavity designs, have also been demonstrated on silicon photonics platforms.<sup>90</sup> LN can also be doped with rare earth ions to realize interesting devices.<sup>91</sup> With the development of TFLN technology, rare earth doped amplifiers<sup>92</sup> and lasers<sup>93</sup> have been demonstrated that can solve the chip-scale light source problem and pave the way toward large-scale photonic integrated circuits (PICs). The doping with these rare earth ions can take place either during the crystal growth phase<sup>94</sup> or with postprocessing.<sup>95</sup> More details about rare earth doped devices can be found in Sec. 4.5.

## 3 Processing Technology

### 3.1 Planar Device Technology

Light confinement is a fundamental problem in photonics applications generally. The refractive index of LN is around  $2.341(n_o)/2.2547(n_e)$ .<sup>41</sup> Optical confinement and waveguiding require index contrast. In a typical planar bulk LN crystal, methods to introduce a refractive index contrast to form waveguides or other confinement structures can be divided into four main types:<sup>96</sup> (1) Li-out diffusion, (2) metal ion-in diffusion, (3) PE, and (4) ion implantation. All of them form a planar device configuration.

#### 3.1.1 Li-out diffusion

The Li-out diffusion method was first demonstrated by Kaminow and Carruthers.<sup>97</sup> As LN can crystallize in a slightly nonstoichiometric form  $(\text{Li}_2\text{O})_y(\text{Nb}_2\text{O}_5)_{1-y}$ , its extraordinary index  $n_e$  will increase linearly when the alloying variable  $y$  decreases within a narrow range between 0.48 and 0.5. The change of  $y$  can be realized by the Li-out diffusion of  $\text{Li}_2\text{O}$  from the LN

surface since the lithium ion has high mobility. Therefore, by applying a thermal treatment of an LN sample for several hours at high temperature, the refractive index will be changed in an LN target area as Li is diffused away.<sup>96</sup> This method has two main disadvantages. One is that the refractive-index change occurs only in  $n_e$ , and the other is that it is difficult to achieve selective diffusion.<sup>98</sup> Therefore, although Li-out diffusion is proposed in principle and has been demonstrated in experiment,<sup>97,99,100</sup> it is seldom used for photonics device fabrication. Alternatively, ion-in diffusion is more frequently adopted for LN device fabrication.<sup>19</sup>

#### 3.1.2 Metal ion-in diffusion

During the metal ion-in diffusion process, a thin layer of metal is first evaporated onto an LN crystal surface, and then the crystal is heated at a temperature in a nonreactive atmosphere for several hours to make the metal diffuse into the crystal.<sup>19,98,101–112</sup> A schematic of a photonic waveguide fabrication process based on ion-in diffusion is shown in Fig. 2(a). Different metals have been used for ion-in diffusion. Some of these are summarized in Table 2. The most widely used metal is titanium (Ti).<sup>19</sup> The metal ion-in diffusion method is an easy and economical method for fabricating photonics devices. For experimental demonstration, as shown in Table 2, propagation loss below 1 dB/cm in photonics wires using such method has been realized.<sup>98,113–115</sup> Before the appearance of TFLN devices, metal ion-in diffusion was widely used in photonic device fabrication. However, the refractive index difference formed by this method is very small (normally < 0.02). Another method called PE can result in a slightly larger refractive index contrast,<sup>20,21</sup> although also not very high overall.

#### 3.1.3 Proton exchange

In 1981, PE was first used to fabricate optical waveguides in LN.<sup>20,21</sup> Different from metal ion-in diffusion, hydrogen ions are diffused into an LN crystal and are then exchanged with lithium ions during the PE process. The lithium ions then diffuse out of the crystal and finally the LN crystal is partially transformed into a new chemical with composition  $\text{H}_x\text{Li}_{1-x}\text{NbO}_3$  within a certain surface depth. The  $\text{H}_x\text{Li}_{1-x}\text{NbO}_3$  compound has several different phase states depending on the component proportion ( $x$ ), as validated by X-ray rocking curve analysis results and some other techniques.<sup>116</sup> Several proton sources have been used for the PE process, such as benzoic, octanoic, adipic, glutaric, stearic acids, and their mixtures.<sup>117–119</sup> Among them, benzoic acid is the most widely used proton source, as it has a high boiling point and stability throughout its liquid phase.<sup>116</sup> A typical process flow for photonic device fabrication using PE is shown in Fig. 2(b). Compared with the metal ion-in diffusion method, the PE process has a much higher photorefractive damage threshold for visible light confining and transmission,<sup>120</sup> as well as a higher resulting refractive index contrast.<sup>121</sup> The PE process has been widely used to fabricate photonics devices in LN crystals with different orientations.<sup>116,121–126</sup> Other than PE, a few other ions have also been used in such an exchange process with lithium to realize a refractive index change in LN.<sup>127–130</sup> For example, Shah et al. demonstrated a kind of LN waveguide by immersing X-cut LN crystals in silver nitrate at 360°C temperature for several hours, and lithium/silver ion exchange was observed.<sup>127</sup> Although with the more recent development of TFLN, direct dry etching has recently received more attention as it results in a much larger index contrast than either PE or

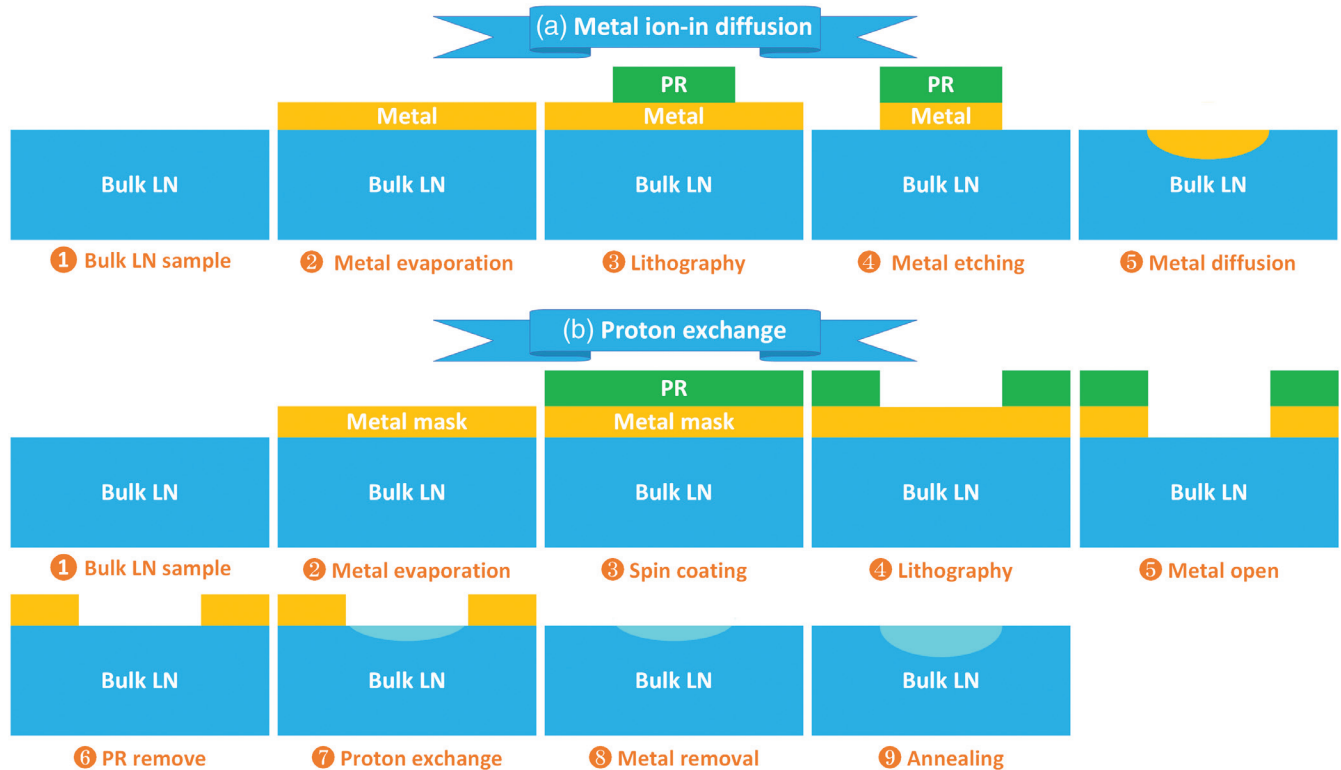


**Fig. 2** Process flow of planar LN device fabrication. Illustration of (a) metal ion-in diffusion and (b) PE methods for planar photonic device fabrication in bulk LN crystals (dimensions are not drawn to scale). PR, photoresist.

**Table 2** Summaries of metal ion-in diffusion method.  $T$ , temperature; TE, transverse electric; TM, transverse magnetic; N.A., not available/applicable; Zn, Zinc.

Year	Metal	Depth ( $\text{\AA}$ )	Atmosphere	Time (h)	$T$ ( $^{\circ}\text{C}$ )	$\Delta n_o/n_e$	Loss	Ref.
1974	Ti/V/Ni	500	Argon (Ar)	6	960/970/800	Ti: 0.01/0.04 V: 0.0005/0.004 Ni: 0.0095/0.006	1 dB/cm at 630 nm	19
1975	TiO <sub>2</sub>	200	Oxygen	10	900 to 1150	0.002	TE: 0.8 dB/cm TM: 0.7 dB/cm	98
1977	Co, Ni, Cu, Zn	10,000	Air	N.A.	900 to 1100	N.A.	N.A.	101
1978	Ti	400 to 600	Air	5	1050	N.A.	2 dB/cm at 633 nm	102
1978	Ti	500	Air	10	1000 to 1100	0.0077/0.0105	N.A.	103
1979	Ti	500	N.A.	5.5	1060	N.A.	1.25 dB/cm	104
1979	Ti	75	Ar	4.5	940	N.A.	N.A.	105
1980	Ti	500	Air	5	975 to 1075	0.005	0.5 dB/cm	113
1982	Ti	740	Ar	6	1050	0.00051/0.00049	0.62 dB/cm at 1.3 $\mu\text{m}$	114
1983	Ti	950	O <sub>2</sub> and H <sub>2</sub> O	6	1050	N.A.	N.A.	106
1984	TiO <sub>2</sub>	50 to 150	Oxygen	5 to 10	1000	N.A.	N.A.	107
1994	Ti/Ni	200/180	N.A.	8/2.5	1050/960	N.A.	N.A.	108
1995	Ni	220	N.A.	1.5	800	0.0112	N.A.	109
1996	Ni	100	N.A.	4 to 6	900	$\sim$ 0.002 to 0.016	TE: 0.7 dB/cm TM: 1.4 dB/cm	110
1999	Zn	N.A.	N.A.	N.A.	700 to 800	$\sim$ 0.0033 to 0.0077	N.A.	111
2006	Zn	N.A.	Zn	2	500	0.0012	N.A.	112
2019	Ti	700	Wet oxygen	Several	1010	N.A.	0.5 dB/cm	115

ion-in diffusion, the PE method still has certain advantageous application scenarios, especially to assist dry/wet etching technologies to realize some innovative photonic devices.<sup>131</sup>

### 3.1.4 Ion implantation

Ion implantation can also be used for fabricating waveguides in LN crystals.<sup>132–137</sup> Different from the above-mentioned methods, ion implantation results in a decrease of refractive index around the target area. Destefanis et al. implanted helium (He) ions into LN surfaces with about 1 to 2 MeV energies.<sup>132</sup> They formed a low refractive index layer in the 2 to 4  $\mu\text{m}$  range just below the LN surface. Such a region of lower refractive index can form sufficient refractive index contrast for light confinement. It is worth mentioning that such a low index layer is very easy to etch by wet etchant, compared with these areas without damage. Therefore, such a buried layer can also be etched away to obtain a much larger refractive index difference.<sup>138</sup> We will introduce this method again when we discuss wet etching. Other than the He ion, other ions have also been demonstrated for ion implantation of LN.<sup>133,135</sup> Although a very large index difference can be obtained based on such methods, many more crystal defects will also be produced during the physical bombardment. Therefore, ion implantation has not been widely used for the formation of photonics devices in LN crystals. But He ion implantation is widely used in CIS technology, which is used for fabrication of TFLN. More details about TFLN process technologies are introduced in the subsequent sections.

## 3.2 Thin Film Lithium Niobate Fabrication Technology

Though bulk LN devices have been widely adopted during the past decades, their low index contrast and therefore weak light

confinement have severely limited its further development toward large scale and dense integration. TFLN is thus proposed and developed to meet the advanced requirements of future devices. There are many different methods that have been proposed to create the TFLN. For example, TFLN can be directly sputtered onto a glass substrate,<sup>139</sup> or grown on GaAs by pulsed laser deposition,<sup>140</sup> or grown on a lithium tantalate substrate by the chemical vapor deposition (CVD) method.<sup>141</sup> However, the directly grown/sputtering method may cause damage to the crystal quality as the measured EO properties are not as good as the bulk counterpart.<sup>139–141</sup>

### 3.2.1 Crystal ion slicing

In contrast, CIS technology can realize high-quality single crystal TFLN wafers and has widely been used since 1998.<sup>5,142–146</sup> Figure 3(a) shows a schematic of CIS technology. The processing starts from a bulk LN wafer, which is usually grown using the Czochralski method.<sup>147</sup> Then, the bulk LN is implanted with He ions to a specific layer thickness (which depends on the desired TFLN thickness) to form a sacrificial layer. Helium (He) implantation is performed using an ordinary ion implanter. The He ion is the most widely used ion due to its small atomic mass.<sup>142</sup> As the ion implantation will cause LN crystal damage that results in a different subsequent etch rate or thermal properties compared with undamaged areas, it can be comparatively easy to separate the top thin film layer from a bulk LN using a simple etching method, such as hydrofluoric acid (HF) etching. Then, the thin film layer is bonded to a bottom insulator layer using mature wafer bonding methods.<sup>9</sup> Usually, the bottom insulator is selected to be a material with a lower refractive index, such as silicon oxide. The large resulting refractive index contrast between the LN and the bottom insulator enables strong

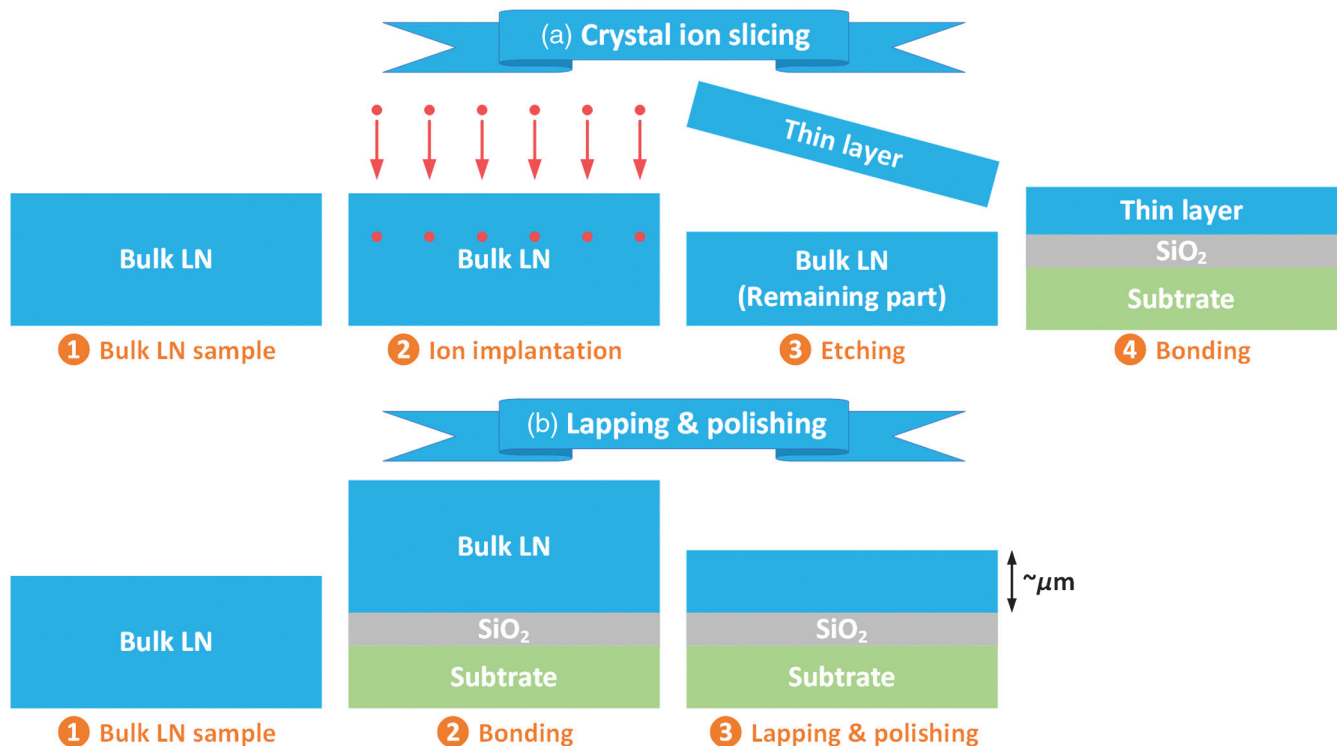


**Fig. 3** Process flows of (a) CIS and (b) lapping and polishing technologies. Dimensions are not drawn to scale.

light confinement within the LN layer. It is worth mentioning that the bottom substrate is not only restricted to LN, glass or Si is also possible. Furthermore, a thin layer of metal can also be inserted between the substrate and insulator layer to form a bottom metal electrode.

### 3.2.2 Lapping and polishing

In addition to CIS technology, the lapping and polishing method has also been developed for LN film fabrication. Figure 3(b) shows the process flow of the lapping and polishing method. The thick bulk LN wafer is first bonded onto a substrate with an insulator (of lower refractive index) inserted between them. Then, the top LN layer is thinned down to a few microns thickness by successive lapping and polishing.<sup>29,30</sup> Compared with the CIS method, the LN film thickness after lapping and polishing is a little bit thick (typically around a few microns) and thus results in a larger device size. However, there are some advantages of LN films made by this technology. First, lapping and polishing is a purely mechanical process and thus has a smaller influence on crystal quality compared with CIS technology. In addition, the larger waveguide core in thick LN films enables a better coupling efficiency and a much higher laser-damaged threshold compared with thinner LN films.<sup>29,30,148–154</sup> Therefore, lapping and polishing is a good complement to CIS technology.

### 3.3 Heterogeneous Integration

In the previous subsection, we introduced a kind of TFLN by wafer bonding a thin layer of LN onto an insulator with a lower refractive index (LNOI structure). In such a structure, 3D waveguides are directly etched to enable light transmission, and thus most of the optical field can be confined within the LN layer. There is another way to realize interaction of light with LN crystal, though, where the LN is not patterned at all. We refer to such a method as heterogeneous integration of LN with other material systems. As far back in 2009, Solmaz et al. demonstrated a type of integrated  $\text{As}_2\text{S}_3$  ring with Ti-diffused LN. As the refractive index of  $\text{As}_2\text{S}_3$  is very close to LN ( $\text{As}_2\text{S}_3$  is 2.4, LN is 2.2), the transmitted light inside a Ti diffused LN waveguide can be vertically coupled into an  $\text{As}_2\text{S}_3$  waveguide.<sup>155</sup> Since then, various kinds of heterogeneous integration schemes have been demonstrated, as summarized in Table 3.

These schemes can be divided into two categories. The first involves directly bonding/growing TFLN onto other mature material platforms,<sup>156,157,160,161,166,170</sup> such as SOI wafers. Here, the light is confined inside these mature material layers with patterned structures, and the optical mode is designed to partially overlap with a top bonded/grown LN layer. Figures 4(a)–4(c) show an example of an LN on silica hybrid micro-resonator.<sup>161</sup> About 15.47-nm root mean square (RMS) surface roughness is

**Table 3** Summary of heterogeneous integration of LN with other material systems. ALD, atomic layer deposition; N.A., not available/applicable; a-Si, amorphous silicon.

Year	Cut	Structure	Thickness	Device	Integration method	Ref.
2009	X-cut	$\text{As}_2\text{S}_3/\text{Ti}:\text{LN}$	470 nm/N.A.	Ring	Magnetron sputtering	155
2011	Z-cut	$\text{LN}/\text{Si}/\text{SiO}_2$	$\sim 1 \mu\text{m}/250 \text{ nm}/2 \mu\text{m}$	Ring	Bonding	156
2012	Z-cut	$\text{LN}/\text{Si}/\text{SiO}_2$	600 nm/250 nm/2 $\mu\text{m}$	Ring <i>E</i> -field sensor	Bonding	157
2013	Y-cut	$\text{Ta}_2\text{O}_5/\text{LN}/\text{SiO}_2$	200 nm/400 nm/1.6 $\mu\text{m}$	Ring modulator	Bonding and deposition	158
2014	X-cut	a-Si:H/LN	90 nm/N.A.	MZI modulator	PECVD	159
2014	Z-cut	$\text{LN}/\text{Si}/\text{SiO}_2$	1 $\mu\text{m}/250 \text{ nm}/1 \mu\text{m}$	Ring modulator	Bonding	160
2015	N.A.	$\text{LN}/\text{silica}$	290 nm/2 $\mu\text{m}$	Whispering-gallery-mode resonator	Excimer laser ablation	161
2015	X-cut	$\text{SiN}_x/\text{LN}/\text{SiO}_2$	260 nm/700 nm/2 $\mu\text{m}$	MZI modulator	PECVD	162
2015	Z-cut	$\text{TiO}_2/\text{LN}/\text{SiO}_2$	95 nm/600 nm/N.A.	Waveguide	Magnetron sputtering	163
2015	Y-cut	$\text{Ge}_{23}\text{Sb}_7\text{S}_{70}/\text{LN}/\text{SiO}_2$	350 nm/400 nm/2 $\mu\text{m}$	MZI modulator	Bonding and E-beam evaporation	164
2016	X-cut	$\text{SiN}/\text{LN}/\text{SiO}_2$	390 nm/700 nm/2 $\mu\text{m}$	PPLN waveguide	Magnetron sputtering	54
2016	Y-cut	$\text{SiN}/\text{LN}/\text{SiO}_2$	500 nm/400 nm/2 $\mu\text{m}$	MZI modulator	Bonding and PECVD	165
2017	X-cut	$\text{LN}/\text{Si}_3\text{N}_4/\text{SiO}_2$	300 nm/850 nm/N.A.	Waveguide	LPCVD and Bonding	166
2017	X-cut	$\text{Si}/\text{LN}$	145 nm/N.A.	Resonator	Bonding	167
2019	X-cut	a-Si/LN/SiO <sub>2</sub>	100 nm/300 nm/2 $\mu\text{m}$	Photodetector	PECVD	34
2020	X-cut	$\text{SiN}_x/\text{LN}/\text{SiO}_2$	220 nm/300 nm/4 $\mu\text{m}$	MZI modulator	PECVD	168
2020	X-cut	$\text{SiN}_x/\text{LN}/\text{SiO}_2$	200 nm/300 nm/4.7 $\mu\text{m}$	MZI modulator	LPCVD	169
2020	X-cut	$\text{LN}/\text{SiN}_x/\text{SiO}_2$	200 nm/225 nm/N.A.	MZI modulator	Bonding	170
2020	X-cut	$\text{Si}_3\text{N}_4/\text{LN}/\text{SiO}_2$	200 nm/300 nm/N.A.	Spectrometer	PECVD	171
2020	Z-cut	$\text{NbN}/\text{HfO}_2/\text{LN}/\text{SiO}_2$	5 nm/10 nm/615 nm/2 $\mu\text{m}$	Superconducting SPD	ALD	172
2020	N.A.	$\text{Polymer}/\text{LN}/\text{SiO}_2$	500 nm/400 nm/N.A.	Mode (de)multiplexer	Spin coating	35

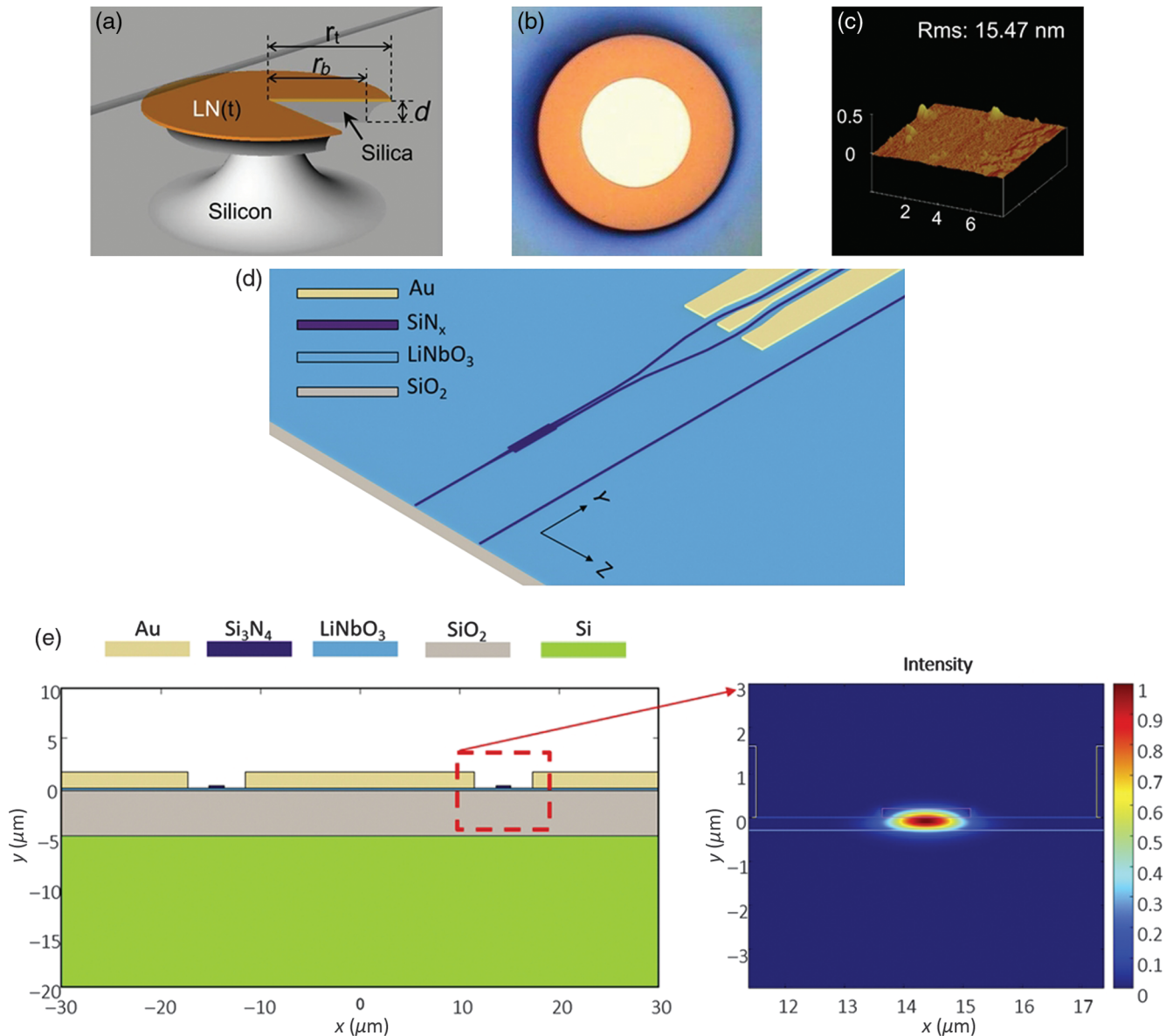


**Fig. 4** Heterogeneous integrated LN devices. (a) Schematic structure, (b) optical, and (c) atomic force microscopic images of an LN on silica hybrid micro-resonator. (a)–(c) Adapted from Ref. 161 © 2015 Wiley-VCH Verlag GmbH and Co. (d) 3D schematic structure, (e) cross section and optical field distribution of a  $\text{SiN}_x$  on LN hybrid MZI modulator. (d) and (e) Adapted from Ref. 169; all article content, except where otherwise noted, is licensed under a Creative Commons Attribution (CC BY) license.

measured, which supports highly efficient EO application. The other scheme involves integrating or depositing a thin layer of a specific material (which is typically easier to dry etch than LN itself) that has a similar refractive index with LN above/onto the TFLN.<sup>34,35,54,155,158,159,162–165,167–169,171–174</sup> Usually, these materials are directly grown on the LN surface, with a method such as magnetron sputtering,<sup>54,155,163</sup> plasma-enhanced chemical vapor deposition (PECVD),<sup>34,159,162,168,171</sup> or low-pressure chemical vapor deposition (LPCVD).<sup>166,169</sup> As shown in Figs. 4(d) and 4(e), by patterning the deposited  $\text{SiN}_x$  above the LN, the optical mode can be confined well inside the waveguide and an EO modulator can thus be realized.<sup>169</sup> In such a scenario, the introduced material together with the LN layer forms the light confinement

structure. Thus, the overlap of the optical mode and the LN layer is designed to be large. In addition, an etchless TFLN platform with photonic bound states in the continuum (BIC) has also been demonstrated recently through direct patterning of the above integrated organic polymer.<sup>35,173,174</sup> In both methods, the LN layer is usually not patterned, and the geometry of the structure is defined in the other material with a more mature processing technology. Therefore, these methods avoid the well-known problem of LN crystals being difficult to etch.<sup>175</sup> When there are no good etching solutions of LN available, heterogeneous integration becomes a good choice. Various types of devices have been realized based on these two schemes, as shown in Table 3. It is worth noting that the applications presented are not limited to

active devices, as passive devices can also be realized. For example, hybrid grating couplers (GCs) for light coupling based on patterned Si<sup>176</sup> and gold (Au)<sup>177</sup> have been demonstrated. As the propagating optical field is only partially overlapping the LN crystal, the interactions between the light and LN are not maximized relative to what they would be if the light were instead fully confined within the LN. However, such methods are still attractive as they combine both the advantages of LN and the other well-developed material platform chosen, while avoiding difficulties associated with LN fabrication processes.

### 3.4 Etching Technology

#### 3.4.1 Dry etching

For both bulk LN and TFLN, there are strong motivations toward direct etching to form 3D structures.<sup>178</sup> Dry etching is one of the main methods to realize such a goal. The plasma of a chemically active gas together with an inert ion plays the main roles during dry etching. As summarized in Table 4, many different kinds of dry etching methods have been demonstrated during the past decades. These demonstrations can be divided into three categories. One involves using the plasma of pure halogen ions,<sup>179,180,182,183,194,196</sup> such as sulfur hexafluoride (SF<sub>6</sub>), carbon tetrafluoride (CF<sub>4</sub>), and boron trichloride (BCl<sub>3</sub>). As halogen ions will chemically react with the lithium, the reactant

produced in the process of dry etching will be a problem and later affect device performance. Figures 5(a) and 5(b) show the scanning electron microscopy (SEM) image and current changed along the etching depth in end point detection after SF<sub>6</sub> etching, which clearly shows the byproduct layer.<sup>182</sup> Nagata et al. tried to remove the reactant using an additional wet etching method.<sup>179</sup> The second category involves mixing the halogen ions with argon (Ar) in the plasma.<sup>178,182,185,186,188,189,191,193,195</sup> Ar ion-based etching is a pure physical bombardment process. By engineering the gas flow ratio between the Ar and halogen element, the etch rate, profile, and surface conditions can be improved. In such a method, the halogen ions can still be a problem and affect the etching quality. Therefore, people have developed the third category of using pure Ar gas for etching.<sup>175,184,190,195</sup> Compared with the first two methods, pure Ar-based etching has a lower etching rate, as the ion bombardment is a pure physical process. Its advantages are flat and clear surface condition, as evidenced by the SEM, AFM, and X-ray photoelectron spectroscopy (XPS) results shown in Figs. 5(c)–5(e).<sup>175</sup> By using Ar-based etching, nearly vertical side walls<sup>52,175,197</sup> and ultralow propagation loss<sup>197</sup> have been observed; this method can then find wide use for photonics device fabrication. During such dry etching processes, a hard mask is typically used in addition to photoresist to improve the etching selectivity, as summarized in Table 4.

**Table 4** Summary of LN dry etching technologies. PMMA, polymethyl methacrylate; HSQ, hydrogen silsesquioxane; MMA, methyl methacrylate; N.A., not available/applicable; RIE, reactive ion etching; ICP, inductively coupled plasma.

Year	Cut	Type	Etch gas	Resist	Mask	Etch rate	Selectivity <sup>a</sup>	Etch type	Ref.
1981	X-cut	Bulk	CCl <sub>2</sub> F <sub>2</sub> , Ar, O <sub>2</sub>	AZ 1350-J	Ni/Cr	55 nm/min	~4 <sup>b</sup>	RIE	178
1998	Z-cut	Bulk	CF <sub>4</sub>	N.A.	Ni	800 nm/h	N.A.	Plasma etching	179
2000	X-cut	Bulk	CF <sub>4</sub>	N.A.	SiO <sub>2</sub>	~60 nm/min <sup>c</sup>	N.A.	Plasma etching	180
2007	Z-cut	TFLN	Ar	SU-8	N.A.	N.A.	N.A.	Plasma etching	181
2008	X/Y/Z-cut	Bulk	CF <sub>4</sub> , O <sub>2</sub> /SF <sub>6</sub> /SF <sub>6</sub> , O <sub>2</sub>	N.A.	Ni/NiCr	2 to 3/10 to 53/37 to 195 nm/min	3–10	RIE/ICP/ICP	182
2009	Y-cut	Bulk	SF <sub>6</sub>	TI09 XR	Ni	20 to 50 nm/min	20	RIE	183
2009	Z-cut	TFLN	Ar	OIR 907-17	N.A.	7.67 nm/min <sup>c</sup>	N.A.	ICP	184
2010	X-cut	Bulk	CHF <sub>3</sub> , Ar	AZ5214	Cr	97.5 nm/min	8.1–16	ICP	185
2010	X-cut	Bulk	CHF <sub>3</sub> , Ar	N.A.	Cr	92.5 nm/min	N.A.	ICP	186
2011	X-cut	Bulk	SF <sub>6</sub> , CF <sub>4</sub> , He	PMMA	Cr	280 nm/min	N.A.	ICP	187
2012	Z-cut	Bulk	SF <sub>6</sub> , Ar	AZ5214E	Cr	98.6 nm/min	12	ICP	188
2015	Z-cut	Bulk	BCl <sub>3</sub> , Ar	N.A.	Ni	100 nm/min	7	ICP	189
2016	X-cut	TFLN	Ar	S1828	N.A.	12 nm/min	N.A.	ICP	190
2018	Z-cut	TFLN	CHF <sub>3</sub> , Ar	N.A.	Cr	N.A.	7	Plasma etching	191
2018	X-cut	TFLN	Ar	N.A.	N.A.	N.A.	N.A.	RIE	192
2019	Z-cut	TFLN	Cl <sub>2</sub> , BCl <sub>3</sub> , Ar	PMMA	SiO <sub>2</sub>	200 nm/min	0.69	RIE	193
2019	X-cut	TFLN	Ar	HSQ	N.A.	N.A.	N.A.	ICP	52
2019	Z-cut	Bulk	SF <sub>6</sub> , O <sub>2</sub>	N.A.	Cr/Cu	812 nm/min	77	ICP	194
2021	X/Z-cut	TFLN	Ar	ma-N 1400	Cr	15 to 30 nm/min	1.4	ICP	175
2021	X-cut	TFLN	CF <sub>4</sub> , Ar; Cl <sub>2</sub> , Ar; Ar	MMA/PMMA	Cr	35 to 50 nm/min; 20 to 33 nm/min; 12 to 18 nm/min;	N.A.	ICP	195

<sup>a</sup>Selectivity is defined by the etch rate ratio between LN and the mask.

<sup>b</sup>Extracted from demonstrated pictures.

<sup>c</sup>Calculated based on the demonstrated data.

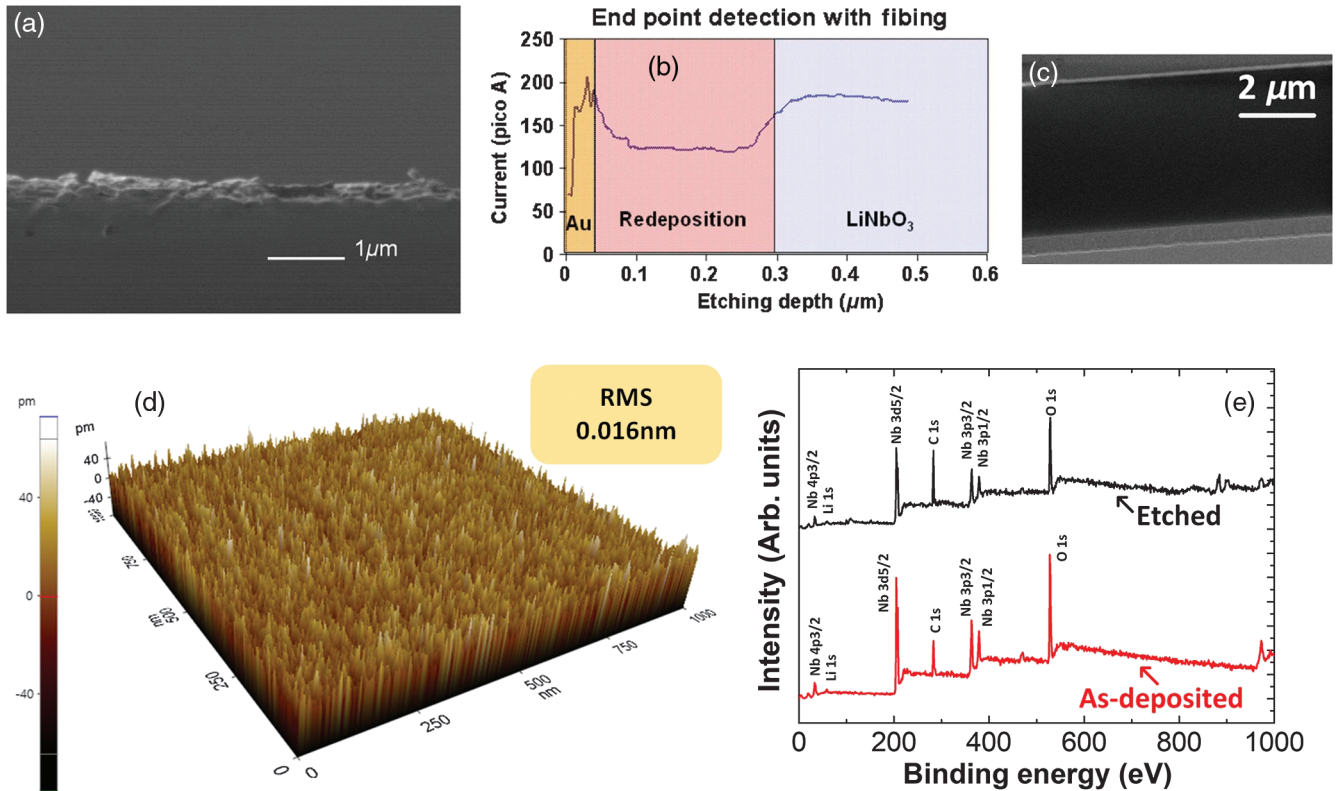


**Fig. 5** Dry etching results of LN. (a) SEM image of the LN cross section and (b) current changed along etching depth in end point detection after  $\text{SF}_6$  based etching. (a) and (b) Adapted from Ref. 182 © 2008 American Institute of Physics (AIP). (c) SEM, (d) AFM, and (e) XPS images of LN sample after Ar-based dry etching. (c)–(e) Adapted with permission from Ref. 175.

### 3.4.2 Wet etching

LN can also be etched by the wet etching method. Compared with dry etching, wet etching can realize a more uniform surface and much higher etch rates.<sup>198</sup> In addition, wet etching is an economical and simple method compared with other etching technologies and is widely used in other material systems.<sup>109</sup> It has been demonstrated that after the PE process, for instance, LN shows a larger etch rate using the mixture of HF and nitric acid ( $\text{HNO}_3$ ), compared with LN areas that are not subjected to the PE process.<sup>199</sup> Therefore, the combination of PE and a mixture of HF and  $\text{HNO}_3$  etchant is widely used for LN wet etching.<sup>109,199–204</sup> Compared with dry etching, its etched sidewall is not too deep and there can be an underetching problem. Ting et al. demonstrated that the etching depth and aspect ratio can be improved using a diluted PE source with a lithium compound.<sup>198</sup> By optimizing different molar percentages of adipic acid and lithium compounds, a very high aspect ratio [defined as etched depth  $D$  divided by horizontal distance of the slant  $H$ , as shown in Figs. 6(a)–6(f)] has been realized. Such an improvement can be clearly seen from the SEM images shown in Figs. 6(a)–6(f). The underetching problem can be alleviated by annealing (improve the adhesion of hard mask), as demonstrated by Hu et al.<sup>205</sup> Some researchers also demonstrated that by adding some ethanol into the HF –  $\text{HNO}_3$  mixture, the etched surface of LN can be much smoother.<sup>205</sup> PE is not the only way to cause a subsequent LN etching rate difference. Wang et al. found that  $\text{O}^+$  and  $\text{Si}^+$  ion implanted regions can be etched more easily

than those protected by a photoresist mask using a mixture of HF and  $\text{HNO}_3$  at room temperature.<sup>206</sup> Si et al. demonstrated that He ion implantation caused crystal damage in LN, which consequently also showed a higher chemical etching rate,<sup>138</sup> and photonic crystal waveguides were successfully realized using such a method, as shown in Fig. 6(g). Using an ion beam enhanced etching method, a similar damaged layer can also be obtained.<sup>207</sup> Copper (Cu) ion implantation with the assistance of HF solution has also been validated as a good way to achieve wet etching of LN crystals, and an etching rate of around 100 nm/s has been observed.<sup>32</sup> Up until now, most of the reported wet etching methods have been demonstrated in bulk LN crystals. But we believe wet etching is also suitable for TFLN devices, especially in some scenarios where cantilever structures are needed.

### 3.4.3 Other patterning/etching technologies

In addition to the above-mentioned methods, some other methods have also been used for the patterning/etching of LN. Most of them have been based on the physical polishing/milling process, such as focused ion beam (FIB) milling,<sup>208–211</sup> dicing,<sup>212,213</sup> femtosecond laser micromachining,<sup>214–218</sup> and chemomechanical polish lithography (CMPL).<sup>214,215,217,219–223</sup> FIB itself is a pure mechanical milling process, which either can be used along<sup>208,209,211</sup> or together with other dry etching methods for layout patterning.<sup>208,210</sup> For prototype validation, FIB is a good choice. But it will not be suitable for mass production of devices

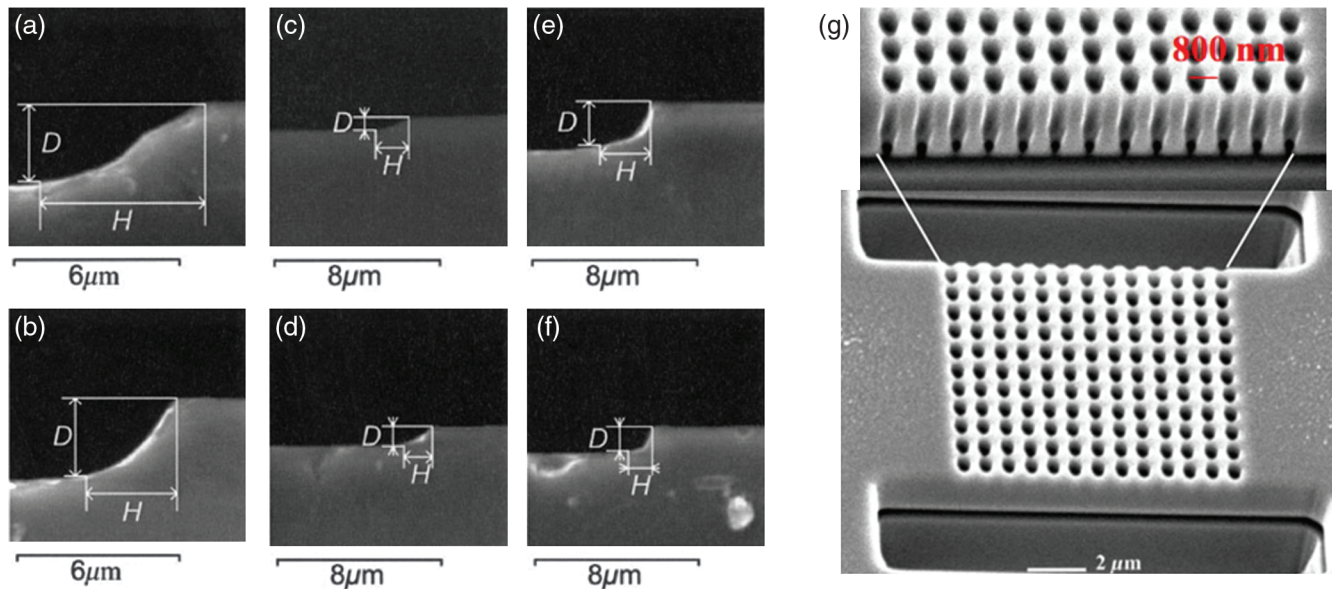


**Fig. 6** Wet etching results of LN. SEM images of the LN etched cross section using undiluted (a) 0% and (b) 20% of adipic acid, (c) 0% and (d) 20% of adipic acid with 0.6% of lithium benzoate, (e) 20% and (f) 30% of adipic acid with 0.3% of lithium carbonate (concentrations in percent represent mole fractions). (a)–(f) Adapted from Ref. 198 © 2006 Wiley Periodicals, Inc. (g) SEM image of photonic crystals (PhCs) using ion implantation and wet etching. Adapted with permission from Ref. 138 © 2010 American Vacuum Society.

of any type due to economic and operability considerations. By contrast, dicing is an efficient method for quick fabrication of optical waveguides, as it can realize smooth sidewalls and a high aspect ratio.<sup>212,213</sup> Recently, femtosecond laser ablation combined with FIB<sup>214–218</sup> or CMPL<sup>214,215,217,219–221</sup> has also been demonstrated for LN crystal patterning, which has received wide attention. Such a method can be divided into three steps. First, the LN crystal or metal mask is ablated with tightly focused femtosecond laser pulses, which is usually performed in water to reduce the possibility of debris and cracks.<sup>215</sup> Second, the LN crystal is polished by the FIB or CMPL process. Third, the underlying oxide is partially etched using a wet etching method. Very high quality factor ( $Q$  factor) ( $\sim 10^8$ ) microresonators have been demonstrated based on such a method,<sup>224</sup> which proves the very high quality of the etched sidewall. These mechanical milling methods together with the above introduced processing technologies pave the way for the fabrication of various LN photonics devices.

## 4 Functional Devices

Compared with other materials systems, LN has many unique features, such as large EO, NLO, and AO effects. The details of these effects are described in Sec. 2. For a long time, LN-based photonics devices were demonstrated only in bulk LN crystals, such as the Ti diffused EO modulator that is widely used in current fiber-optic communication systems due to its large bandwidth and superior linear EO response.<sup>3</sup> The recently developed high-quality TFLN together with various etching technologies, however, has made significant headway toward integrated LN photonics. Many different kinds of photonics devices fabricated in bulk LN have now been demonstrated in TFLN, including passive devices, EO devices, nonlinear optical devices,

AO devices, rare earth doping devices, pyroelectric devices, TO devices, etc.

In this section, we will give a review of functional devices demonstrated in LN during recent years. These devices cover both bulk LN and TFLN, which make use of the effects discussed in Sec. 2 and some key technologies demonstrated in Sec. 3. Here, bulk LN based devices are introduced for comparison with TFLN devices and will not be the main focus as they have been widely discussed in other reviews.<sup>23</sup> From a comprehensive history of LN device evolution, we hope readers can be inspired to achieve improved designs of high-performance devices in the future and contribute to the further development of LN photonics generally.

### 4.1 Passive Devices

The waveguide is the most basic photonic device, as it confines light inside a specific region through refractive index contrast. As discussed in Sec. 2, there are many different ways to realize such a refractive index contrast. In a typical bulk LN crystal, ion-in diffusion, PE, and ion implantation are mostly used to define planar waveguides, while for TFLN, direct etching, including dry etching, wet etching, and a few other types of physical etching can be used to form waveguides for light confinement. Compared with ion-in diffused or PE bulk LN, the large refractive index contrast present at the interface of the top LN layer and the underlying bottom insulator in TFLN makes some compact and low loss devices possible. Researchers have developed several ways to characterize waveguide loss, such as cutback, sliding-prism, Fabry–Perot resonance, and scattered light methods.<sup>225,226</sup> In addition, the propagation loss can also be extracted from the  $Q$  factor of a microresonator,<sup>42,192</sup> which is inversely proportional to the  $Q$  factor of the microresonator.

#### 4.1.1 Microresonator

In past years, various kinds of microresonators have been demonstrated both in bulk LN and TFLN platforms.<sup>43,181,192,193,197,214–218,221,222,224,227–240</sup> In bulk periodically poled Z-cut LN crystals, a high  $Q$  factor of  $2 \times 10^7$  was measured by mechanically polishing the LN crystal,<sup>227</sup> as shown in Fig. 7(a). The  $Q$  factor of the TFLN-based microresonator is increased gradually. In 2014, Wang et al. demonstrated a kind of microdisk in TFLN using Ar-based electron-cyclotron resonance (ECR) reactive ion etching (RIE), and its measured  $Q$  factor was around  $10^5$  [Fig. 7(b)].<sup>228</sup> This was just at the early stage of TFLN devices. Such a value can be further improved by optimizing design and processing technologies. For example, a microring with a  $Q$  factor up to  $10^7$  was demonstrated in 2017 using an optimized Ar-based dry etching process, which corresponds to a propagation loss as low as 2.7 dB/cm.<sup>192</sup> An SEM image of this kind of etched microring and its corresponding measured transmission spectrum are shown in Figs. 7(c) and 7(d), respectively. These results validate the fact that Ar-based etching is a suitable method for TFLN patterning. Meanwhile, many other groups have also demonstrated high  $\sim 10^5$   $Q$  factor based on such a method.<sup>197,230,231,234,236,237</sup> More recently, a record-high  $Q$  factor up to  $10^8$  (calibrated by considering transmission rates of modes) at 1550 nm wavelength was achieved using the femtosecond laser-assisted CMPL method<sup>224</sup> [as shown in Figs. 7(e) and 7(h)], which indicates a propagation loss of around 0.28 dB/m. Such a result is realized using a pure mechanical polishing process, thus avoiding the possible ion-induced lattice damage. This ultralow loss device opens up many prospects toward broad application of LN photonics, especially for various nonlinear applications. Compared with bulk LN devices, low loss or high  $Q$  factors are not the main advantages of TFLN-based microresonator, however, as ultrahigh  $Q$  factors have also been demonstrated in bulk LN devices.<sup>227</sup> More advantageous is the fact that the larger refractive index contrast in TFLN enables various microresonator forms that are ordinarily extremely difficult or impossible to realize in bulk LN. Here, our discussion on microresonators is limited to microrings or microdisks. Actually, some other types of microresonators have also been demonstrated in LN (mainly TFLN), such as photonics crystal (PhC)<sup>241</sup> and distributed Bragg reflector (DBR)-based Fabry–Perot (DBR-FP)<sup>242,243</sup> resonators. Recent progress of EO modulators based on PhC and Fabry–Perot microresonators is discussed in Sec. 4.2.1.

#### 4.1.2 Grating coupler

Due to the strong mode confinement in TFLN, many other passive blocks have subsequently been demonstrated.<sup>85,131,176,177,223,244–269</sup> The fiber to chip interface is a basic function as it determines how much light can be coupled into a photonic device. There are two types of methods to couple the external light into a chip. One is vertical coupling of light onto a chip using a GC.<sup>176,177,245,247,248,252,254,259,265,266,268,269</sup> The other is based on edge coupling,<sup>223,246,249,258</sup> which couples light into a chip horizontally. According to the operation principle, GCs can also be divided into two categories, one is the one-dimensional (1D) GC and the other is the 2D GC, both of which have been demonstrated in the LN platform. For a 1D GC, the design strategy is to optimize the periodic structure to realize the phase matching condition for best coupling efficiency. A high coupling efficiency of  $-1.42/-2.1$  dB ( $\sim 72\%/61.6\%$ ) has been realized in Z-cut TFLN with a bottom Au reflector, and the grating has been designed

with a chirped structure to improve its coupling efficiency,<sup>259</sup> as shown in Figs. 8(a)–8(c). The typical coupling efficiency of a 1D GC is between  $-3$  and  $-7$  dB.<sup>176,177,245,247,248,252,254,268,269</sup> A 2D GC is more functional as it can realize the demultiplexing of orthogonal polarization multiplexed signals while coupling light into on-chip devices.<sup>270</sup> Although there are many reports about 2D GC in other material systems, similar research is very limited in TFLN. Chen et al. demonstrated a kind of 2D GC in TFLN with measured coupling efficiencies of  $-5.13$  dB at 1561 nm for P-polarized light and  $-7.6$  dB at 1568 nm for S-polarized light,<sup>265</sup> as shown in Figs. 8(d)–8(f). Their measured 1-dB bandwidths for both P- and S-polarized lights are around 30 nm. Such demonstrated results are far from comparable to those of its counterparts and hence need more efforts to improve. Both 1D and 2D GCs allow for wafer scale on-chip testing without the need of chip dicing. GCs are more difficult to realize in bulk LN compared with TFLN due to its smaller refractive index contrast.

#### 4.1.3 Edge coupler

Compared with the vertical GC, an edge coupler is less sensitive to polarization, has a larger operating bandwidth, and enables lower insertion loss. Its main drawbacks are that accurate facet polishing and sample dicing are needed. For edge coupling, the main optical loss mechanism is the mode mismatch between the fiber and on-chip waveguide. Therefore, design strategies are to tailor both the fiber and waveguide modes to reduce the mode mismatch and thus improve the coupling efficiency. By adiabatically tapering a standard single-mode fiber to match a specially designed LN waveguide, Yao et al. demonstrated a measured  $-1.32/-1.88$  dB coupling efficiency for transverse electric (TE)/magnetic (TM) modes.<sup>223</sup> Using a monolithic bilayer mode size converter, He et al. also demonstrated a measured 1.7-dB/facet coupling loss,<sup>246</sup> as shown in Figs. 9(a)–9(c). By combining a silicon oxynitride cladding waveguide with the bilayer LN taper, the coupling efficiency is further reduced to 0.54/0.59 dB per facet at 1550 nm for TE/TM light.<sup>266</sup> A multiple layer mode size converter shows a possible solution for low loss edge coupling in TFLN. Compared with the SOI platform, the refractive index contrast in TFLN is smaller and thus results in weaker mode confinement and larger waveguide bending radii. However, a comparable low coupling loss can also be obtained in TFLN by reducing the mode size mismatch between the fiber and waveguide. We believe there is still room for performance enhancement of edge coupling in the LN platform, as lower coupling loss ( $<0.5$  dB/facet) has already been demonstrated in ion-in diffused bulk LN devices.<sup>271</sup>

#### 4.1.4 Other passive devices

In addition, mode-related devices,<sup>131,244,250,251,255,261,262,267</sup> TO-based devices,<sup>85–87</sup> Bragg grating filters,<sup>253,256,257,264</sup> optical true delay lines,<sup>263</sup> and optical phased arrays<sup>260</sup> have also been demonstrated in the LN platform. Most of them rely on the large refractive index contrast available in TFLN. Similar to its counterpart, which is SOI, these passive blocks can be combined together to form more powerful chip scale PICs. And researchers have already tried to do so. For example, a two-mode (de)multiplexer is realized by combining a passive Mach–Zehnder interferometer (MZI) and an EO tuning electrode.<sup>131</sup> This will be a trend as PICs can solve power consumption and device size problems that are inherent in conventional bulk LN devices.

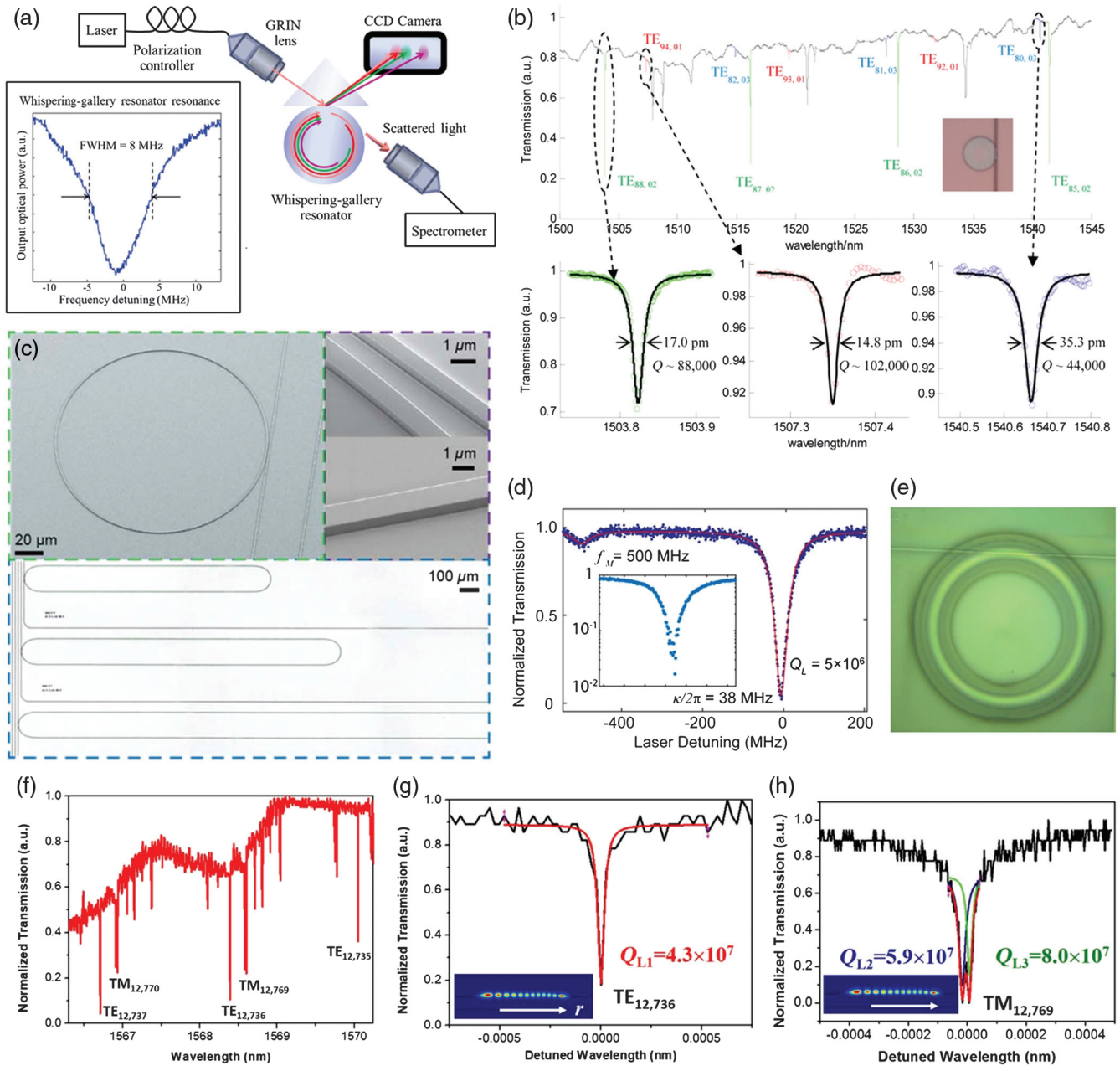


**Fig. 7** LN-based microresonators. (a) Schematic experimental setup for characterizing a mechanical polishing bulk LN whispering-gallery resonator and its corresponding measured  $Q$  factor. Adapted from Ref. 227 © 2011 AIP. (b) Resonance spectra of the fabricated microdisk using ECR RIE technology in TFLN. Inset shows the microscope image of tapered fiber coupling on top of the device. Zoom in views are the details of representative resonance dips. Adapted with permission from Ref. 228 © 2014 Optical Society of America (OSA). (c) SEM (top) and microscopic images (bottom) of microring and microracetrack ring with various lengths, and (d) its measured transmission spectrum. (c) and (d) Adapted with permission from Ref. 192 © 2017 OSA. (e) Microscope image of the waveguide coupled TFLN microring and (f) its measured transmission spectrum. The  $Q$  factors for (g) TE and (h) TM modes fitted by Lorentz-shape curves. (e)–(h) Adapted with permission from Ref. 224 © 2022 Chinese Optical Society (COS).

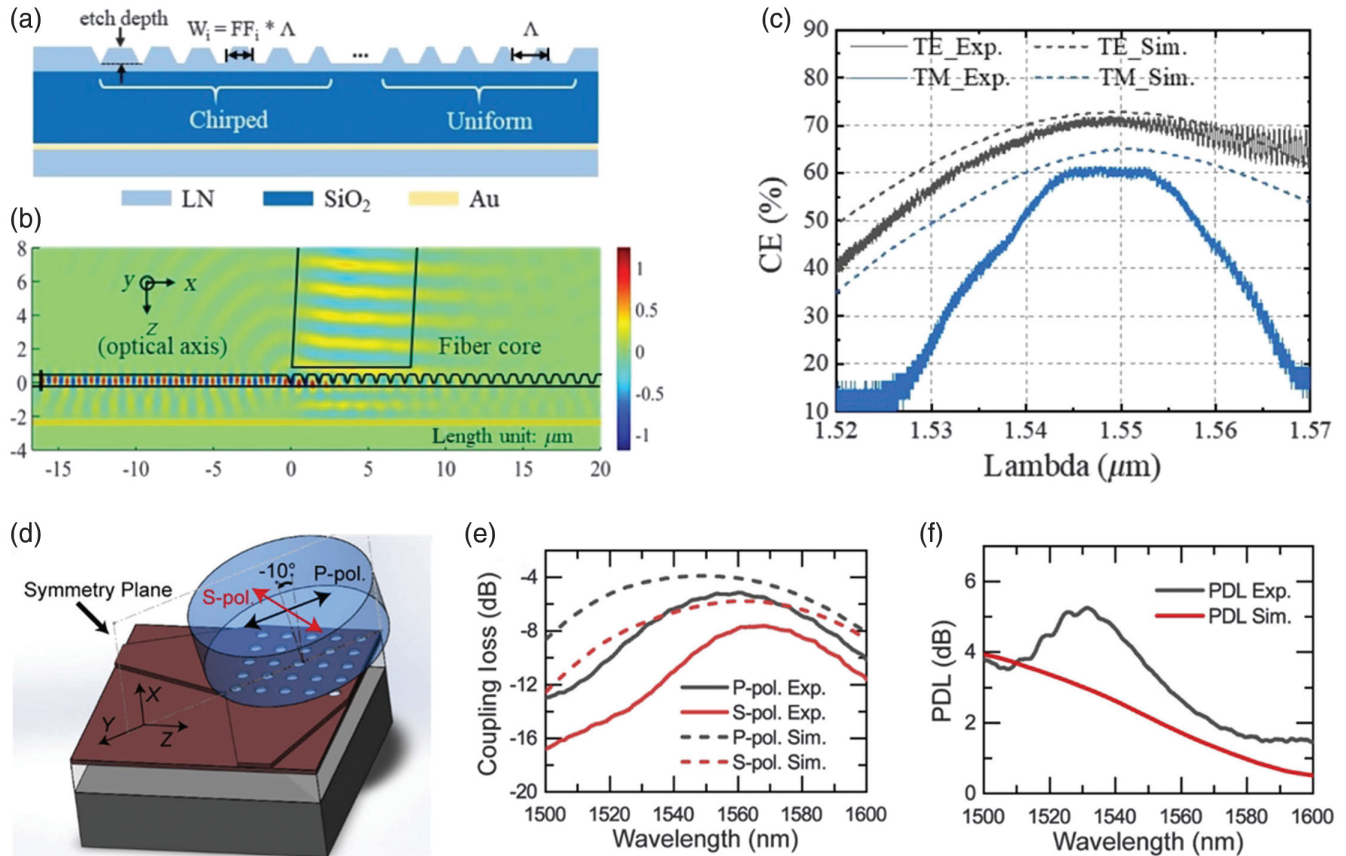


**Fig. 8** LN-based GCs. (a) Schematic structure, (b) simulated electric field distribution and (c) measured transmission spectrum of 1D chirped GC in TFLN. (a)–(c) Adapted with permission from Ref. 259 © 2020 OSA. (d) Schematic structure of a 2D GC in TFLN. Measured and simulated (e) transmission spectra and (f) polarization dependence loss of the TFLN 2D GC. (d)–(f) Adapted with permission from Ref. 265 © 2021 OSA.

## 4.2 EO devices

### 4.2.1 Electro-optic modulator

Compared with other material systems, the most attractive feature of LN is its large EO coefficient, which can be used for fabricating high-performance modulators. Different from the plasma dispersion effect-based modulators in silicon photonics<sup>10</sup> and the electro-absorption-based modulators in III–V platforms,<sup>11</sup> there is no carrier dynamic process in LN-based modulators where the speed is mainly limited by the microwave electrode. Therefore, Pockels effect-based linear LN modulators can achieve higher modulation speeds.<sup>31,52</sup> Therefore, LN-based modulators are widely used in current fiber-optical communication systems. For a long time, these modulators have been fabricated in bulk LN crystals using the technologies described in Sec. 2. For example, a Ti-diffused ring resonator in a bulk LN crystal can achieve around a 1.565 pm/V tuning efficiency.<sup>43</sup> However, these bulky devices have a large device size and cannot meet the requirements of dense integration in current/future large capacity optical interconnect systems. The TFLN platform is well poised to solve these problems. In the same year, Guarino et al. demonstrated an EO tunable microring resonator in TFLN using CIS and wafer bonding technology.<sup>181</sup> Its structure is

shown in Fig. 10(a), where the Z-cut TFLN is directly etched and inserted between the top and bottom electrodes. As shown in Fig. 10(b), the measured tuning efficiency is about 0.105 pm/V from the observed wavelength shift.<sup>181</sup> Such a value is lower than results demonstrated in bulk LN, which is probably due to the lower electric field strength inside the waveguide and can perhaps be improved by changing the design. Subsequently, with the high-quality TFLN that is now commercially available, various kinds of modulators have been demonstrated.<sup>31,52,88,241–243,272–288</sup> Some of the reported modulators in LN platforms are summarized in Table 5.

In terms of device configuration, there are some structures such as microrings,<sup>272,292</sup> MZIs,<sup>31,52,88,272,274,275,277,278,281–285,287</sup> Michelson interferometers,<sup>273,276,279</sup> PhC cavities,<sup>241</sup> and DBR-FP modulators,<sup>242,243</sup> as shown in Table 5 and Fig. 11. Different configurations have different advantages. For example, microring-based modulators have compact sizes,<sup>272,292</sup> and Michelson interferometer modulators (MIMs) [Fig. 11(f)] can realize reduced half-wave voltage-length product ( $V_{\pi}L$ ) due to doubled interaction between the light wave and electric field compared with MZI structures.<sup>273,276,279</sup> The improved tuning efficiency of PhC-based [Figs. 11(d) and 11(e)] and DBR-FP-based [Figs. 11(g)–11(i)] modulators is based on a similar principle.<sup>241–243</sup>

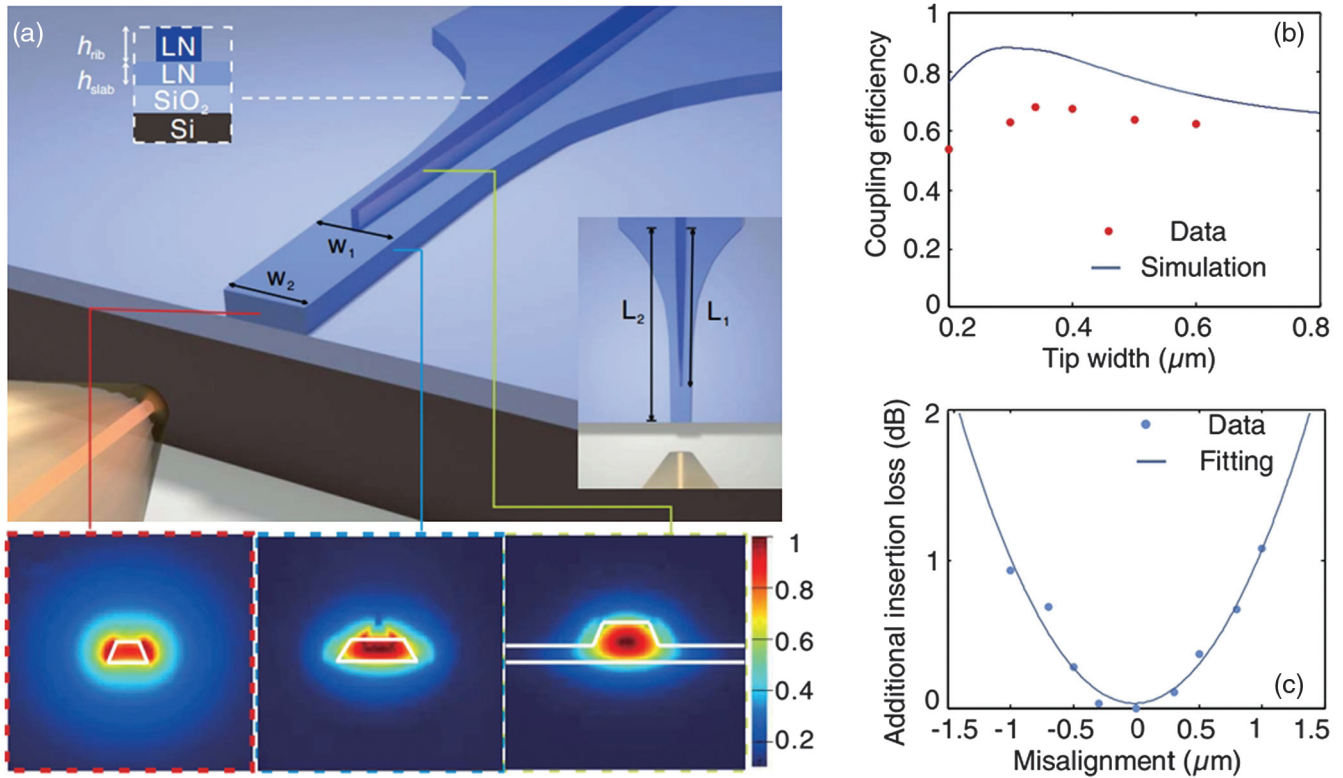


**Fig. 9** LN-based edge coupler. (a) Schematic structure of the bilayer edge coupler and its corresponding mode profiles at different positions. (b) Simulated and measured coupling efficiency versus different tip widths in the tapered slab region. (c) Additional insertion loss with respect to coupling misalignment (TE mode). (a)–(c) Adapted with permission from Ref. 246 © 2019 OSA.

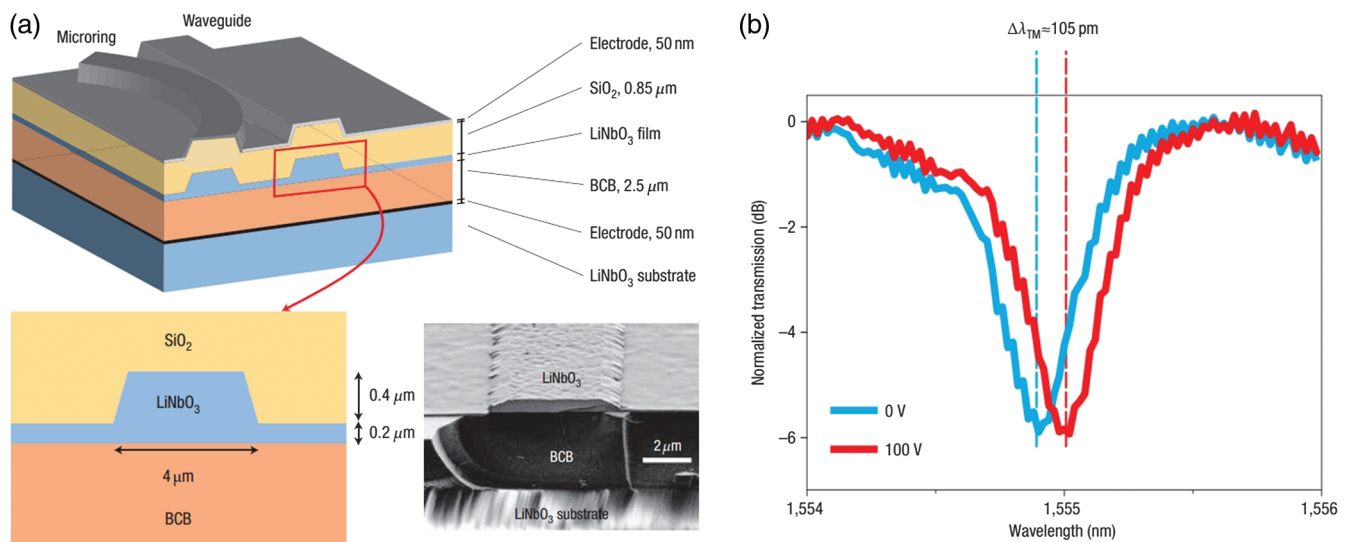


**Fig. 10** TFLN EO tunable microring resonator. (a) Schematic structure (top), cross section (bottom left), and SEM images of the Z-cut TFLN microring modulator, and (b) its EO resonance shift curve. (a) and (b) Adapted with permission from Ref. 181 © 2007 Nature Publishing Group.

**Table 5** Summary of LN-based EO modulators. HI, heterogeneous integration; DMT, discrete multitone; APE, annealed proton exchange; N.A., not available/applicable.

Year	Cut	Type	$V_{\pi}L$	Performance	Process	IL <sup>a</sup> /Q factor	Ref.
2002	X-bulk	MZI	$\sim 12 \text{ V} \cdot \text{cm}$	$S_{21}$ : 30 GHz; ER: 25 dB; data: 40 Gb/s (NRZ)	Ti diffusion	5.4 dB <sup>b</sup>	289
2007	Z-bulk	Ring	N.A.	EO shift: 1.565 nm/V (TM); 0.6912 nm/V (TE)	Ti diffusion and wet etch	N.A.	43
2007	Z-TFLN	Ring	N.A.	EO shift: 0.105 pm/V (TM)	HI and Ar etch	$Q: 4 \times 10^3$	181
2009	Z-bulk	MZI	$5.35 \text{ V} \cdot \text{cm}$	ER: 20 dB	Ti diffusion and wet etch	0.5/0.15 dB/cm (TM/TE)	290
2014	X-bulk	PhC	$0.0063 \text{ V} \cdot \text{cm}$	EO shift: 0.6 nm/V; ER: $\sim 11.2 \text{ dB}$ ; $S_{21}$ : $\sim 1 \text{ GHz}$	APE and FIB	21 dB <sup>b</sup>	291
2018	Y-TFLN	Ring	N.A.	$S_{21}$ : 4 GHz; EO shift: 0.32 pm/V; ER: $>10 \text{ dB}$	$\text{Cl}_2$ ICP	2.3 dB/cm	292
2018	X-TFLN	MZI	$2.2 \text{ V} \cdot \text{cm}^{\text{c}}$	$S_{21}$ : 100 GHz (length: 5 mm); data: 210 Gb/s (8-ASK)	Ar ICP-RIE	$<0.5 \text{ dB}/0.2 \text{ dB/cm}$	31
2018	X-TFLN	MZI Ring	$1.8 \text{ V} \cdot \text{cm}$ (MZI) $7 \text{ pm/V}$ (ring)	$S_{21}$ : 15 GHz (MZI); $S_{21}$ : 30 GHz (ring)	Ar ICP-RIE	MZI: 2 dB; ring: 1.5 dB	272
2019	X-TFLN	MZI	$2.2 \text{ V} \cdot \text{cm}$	$S_{21}$ : $>70 \text{ GHz}$ ; data: 100 Gb/s (NRZ)	HI and Ar ICP	2.5 dB	52
2019	X-TFLN	MIM	$1.4 \text{ V} \cdot \text{cm}$	$S_{21}$ : 12 GHz; data: 35 Gb/s (NRZ)	Ar ICP	4 dB	273
2019	X-TFLN	MZI	$5.3 \text{ V} \cdot \text{cm}$	ER: $>53 \text{ dB}$	ICP	3 dB/cm	274
2019	X-TFLN	MZI	7 to 9 V · cm	$V_{\pi}$ : 3.5 to 4.5 V at 5 to 40 GHz	Ar RIE	$\sim 1 \text{ dB}$	275
2019	X-TFLN	MIM	$1.2 \text{ V} \cdot \text{cm}$	$S_{21}$ : 17.5 GHz; data: 40 Gb/s (NRZ); ER: 6.6 dB	HI and Ar ICP	3.3 dB	276
2019	X-TFLN	MZI	$7.2 \text{ V} \cdot \text{cm}$	$S_{21}$ : 20 GHz	Ti-diffusion	9 dB <sup>d</sup>	293
2020	X-TFLN	PhC	N.A.	EO shift: 16 pm/V; $S_{21}$ : 17.5 GHz; data: 11 Gb/s (NRZ)	Ar ICP	2.2 dB	241
2020	X-TFLN	DBR-FP	N.A.	$S_{21}$ : 60 GHz; data: 100 Gb/s (NRZ); ER: 53.8 dB	Ar ICP	0.2 dB	243
2020	X-TFLN	MZI	$2.7 \text{ V} \cdot \text{cm}$	$S_{21}$ : $>70 \text{ GHz}$ ; data: 128 Gb/s (PAM4); ER: $\sim 40 \text{ dB}$	Ar ICP	1.8 dB	277
2020	X-TFLN	MZI	$2.47 \text{ V} \cdot \text{cm}^{\text{c}}$	$S_{21}$ : $>67 \text{ GHz}$ (7.5 mm arm); data: 320 Gb/s (16 QAM)	Ar ICP	1.8 dB	88
2021	X-TFLN	MZI	$2.74 \text{ V} \cdot \text{cm}$	$S_{21}$ : 55 GHz	ICP	8.5 dB	278
2021	X-TFLN	MIM	$1.06 \text{ V} \cdot \text{cm}$	$S_{21}$ : 40 GHz; data: 70 Gb/s (NRZ)	HI with SiN	4.1 dB	279
2021	X-TFLN	WG	$1.91 \text{ V} \cdot \text{cm}$	Operating at 1064 nm	$\text{CF}_4$ and Ar ICP	7.7 dB	280
2021	X-TFLN	MZI	$0.64 \text{ V} \cdot \text{cm}$	$S_{21}$ : 3 GHz	Ion milling	1.77 dB/cm	281
2021	X-TFLN	MZI	$2.3 \text{ V} \cdot \text{cm}$	$S_{21}$ : $>50 \text{ GHz}$ ; ER: 20 dB	Ar RIE	$<1 \text{ dB}$	282
2021	X-TFLN	MZI	$1.7 \text{ V} \cdot \text{cm}$	$S_{21}$ : $>67 \text{ GHz}$	Ar RIE	17 dB <sup>b</sup>	283
2021	X-TFLN	MZI	$1.75 \text{ V} \cdot \text{cm}$	$S_{21}$ : $>40 \text{ GHz}$	Ar ICP	0.7 dB/cm	284
2021	X-TFLN	MZI	$3.67 \text{ V} \cdot \text{cm}$	$S_{21}$ : 22 GHz; data: 25 Gb/s (NRZ); ER: $>20 \text{ dB}$	Ar ICP	6 dB (2 $\mu\text{m}$ )	285
2021	X-TFLN	DBR-FP	N.A.	EO shift: 15.7 pm/V; $S_{21}$ : 18 to 24 GHz; data: 56 Gb/s (NRZ)	ICP	$<1.65 \text{ dB}$	242
2021	X-TFLN	MZI	$3.068 \text{ V} \cdot \text{cm}$	$S_{21}$ : 60 GHz; data: 200.4 Gb/s DMT data	Ar ICP	3 dB <sup>b</sup>	287
2022	X-TFLN	MZI	$2.35 \text{ V} \cdot \text{cm}$	$S_{21}$ : 110 GHz (1 V); data: 1.96 Tb/s (400 QAM)	Ar ICP	$6.5 \pm 0.5 \text{ dB}$	294

<sup>a</sup>Insertion loss (IL) is typically defined by the device intrinsic without considering coupling loss if there is no specific noting. Due to different characterization methods reported in the literature, here we also list the propagation loss if the original literature did not report the IL data. For the ring modulator, the  $Q$  factor is provided as it also reflects waveguide loss information.

<sup>b</sup>Including coupling loss.

<sup>c</sup>Calculated based on reported data.

<sup>d</sup>Not sure if coupling losses are included.

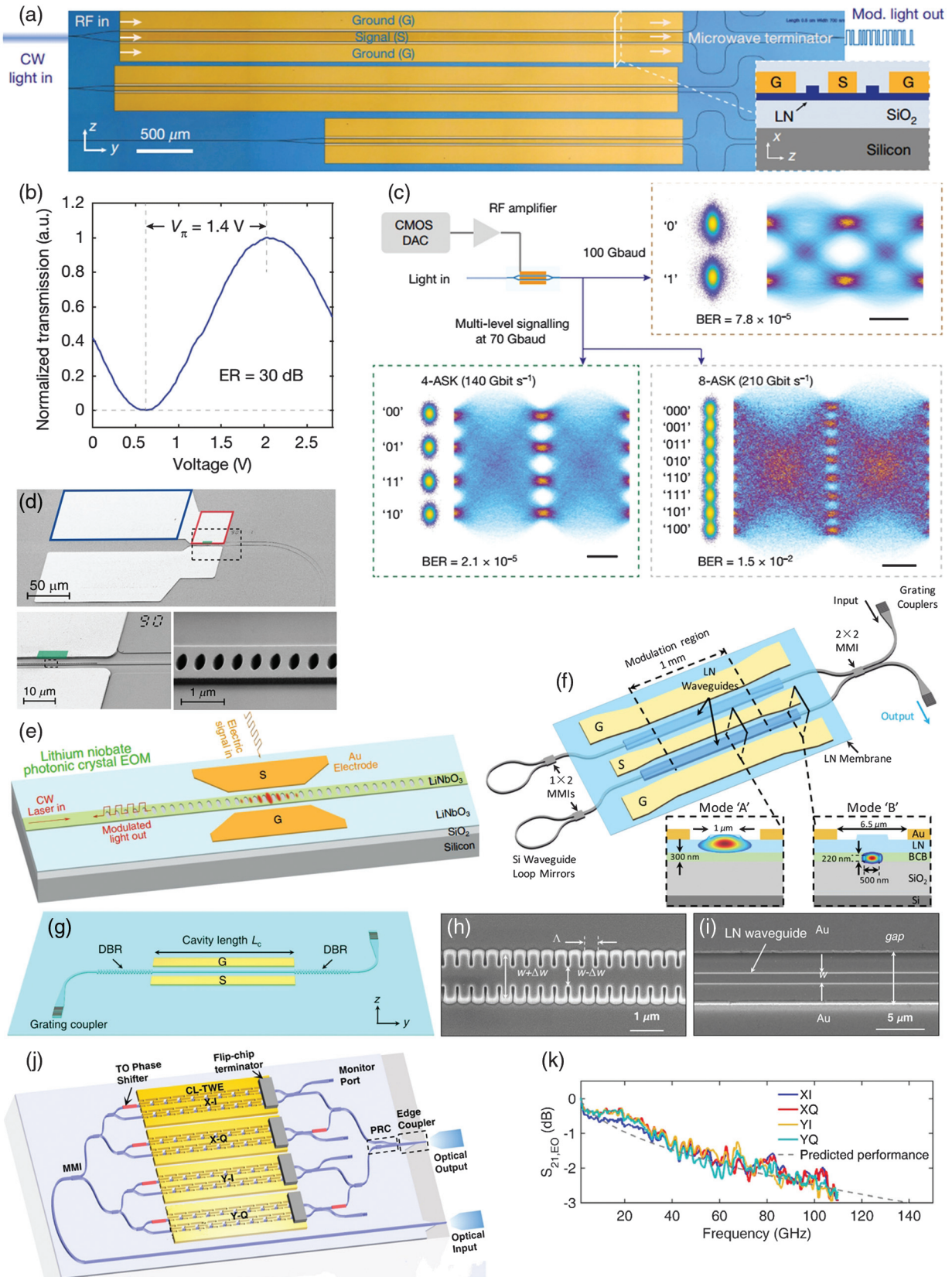


**Fig. 11** TFLN-based modulators. (a) Microscopic image of TFLN MZI modulator (inset is its schematic cross section). (b) Measured transmission spectrum of a 2-cm long device. (c) Measured high speed data transmission results of 100 Gb/s NRZ, 140 Gb/s 4-ASK, and 210 Gb/s 8-ASK signals. (a)–(c) Adapted with permission from Ref. 31 © 2018 Springer Nature Limited (SNL).

**Fig. 11** (*Continued*) (d) SEM images (top: full SEM image; bottom: zoom-in image of the PhC details). (e) Schematic structure of the TFLN PhC modulator. (d) and (e) Adapted with permission from Ref. 241. (f) Schematic structure of the MIM, and insets are cross section mode profiles at different positions. Adapted from Ref. 276. (g) Schematic structure of the TFLN DBR modulator, and SEM images of the (h) DBR and (i) modulation region. (g)–(i) Adapted with permission from Ref. 242 © 2021 COS. (j) Schematic structure and (k) measured  $S_{21}$  curves of the TFLN-based DP-IQ modulator. X and Y represent two orthogonal polarization states, I and Q represent in-phase and quadrature branches. (j) and (k) Adapted with permission from Ref. 294 © 2022 Optica.

In most reported results, the amplitude of the input light is modulated by an applied electrical signal (amplitude modulation). As shown in Figs. 11(a)–11(c), around 100 Gb/s non-return to zero (NRZ) and up to 210 Gb/s 8-ASK (8 level amplitude modulation) are measured using an optimized MZI TFLN modulator. For a 20-mm long arm length, its measured  $S_{21}$  (defined as the forward transmission coefficient from port 1 as input to port 2 as output when port 2 is matched for a two-port network and was widely used to characterize the speed of optoelectronic devices) is above 40 GHz. The authors also demonstrated that its  $S_{21}$  can be improved up to above 80 GHz by reducing the arm length.<sup>31</sup> Some other modulation dimensions can also be added into the TFLN modulator.<sup>88,294</sup> In 2020, Xu et al. first introduced the phase modulation dimension into a TFLN modulator and realized transmission speeds up to 320 Gb/s based on the 16 quadrature amplitude modulation (QAM) format.<sup>88</sup> More recently, researchers from the same group further demonstrated a TFLN-based dual-polarization in-phase (DP-IQ) modulator with record 1.96 Tb/s data rate.<sup>294</sup> Figures 11(j) and 11(k) show a schematic of the DP-IQ modulator with a 2.35-cm long arm and its corresponding measured  $S_{21}$  curves. The researchers used double polarizations and a quadrature amplitude phase modulation format. For each single MZM, the measured  $S_{21}$  is above 110 GHz under 1 V voltage. Such a high bandwidth enables 400-QAM and thus realized a record 1.96 Tb/s total data capacity. By engineering the electrode transmission line<sup>282,295</sup> or introducing more multiplexing dimensions, such as mode division multiplexing,<sup>24</sup> the transmission speed/volume can be further improved.

In addition to speed, some other key metrics are also critical to evaluating modulator performance, such as  $V_{\pi}L$ , as well as insertion loss (IL). As shown in Table 5, most reported results have an average  $V_{\pi}L$  between 1 and 3 V · cm.<sup>52,88,272,273,276–280,282–285,287</sup> Using a dual-capacitor electrode layout, the  $V_{\pi}L$  can be reduced to as low as 0.64 V · cm.<sup>281</sup> Such a factor is highly related to the device structure and can likely be improved by optimizing the design. The overall low  $V_{\pi}L$  values of LN-based modulators are highly desirable for their application scenarios.

It can be observed from Table 5 that most of the reported LN-based modulators have low IL (excluding coupling loss),<sup>31,52,88,241–243,272,275,277,282,287</sup> which depends on the device dimension and fabrication technology. A typical bulk LN-based modulator is usually fabricated using ion-in diffusion technology. For TFLN modulators, Ar plasma-based dry etching is widely used to pattern the LN waveguide structures, which can realize a low propagation loss (also depends on etching conditions) compared with bulk devices. By optimizing the processing technology, the TFLN waveguide with a more prevailing propagation loss of lower than 0.2 dB/cm can be obtained.<sup>31</sup> Thus, high-performance LN-based modulators with lower IL can be expected in the future.

Extinction ratio (ER) is another metric to characterize a modulator's performance. In most published LN-related results, ER is defined by the valley value [such as the minimum value shown in Fig. 10(b)] of the transmission spectrum.<sup>181</sup> A high ER gives a better modulation signal quality, such as more open eye diagrams during data transmission experiments. The typical ER in literature is between 10 and 30 dB,<sup>282,285,292</sup> which can be improved by optimizing either process technology or design. Take the MZI as an example, and usually the Y-branch is used as the power splitter. However, if the optical power difference between the two arms is too large due to the imperfect fabrication process technology, its ER will be degraded. By optimizing the fabrication process, or changing the Y-branch structure with a multi-mode interferometer (MMI, more tolerant to fabrication process error compared with Y-branch),<sup>296</sup> a higher ER can be realized. In addition, using cascaded MZI<sup>274</sup> or Bragg grating waveguide,<sup>243</sup> ultrahigh ERs have been demonstrated, which are other examples of improving ER by optimizing design.

In summary, there are many different criteria to evaluate a modulator's performance. Although there are many different kinds of LN-based modulators that have been demonstrated, none of them can realize all the best metrics at the same time. The tradeoffs exist, thus there are still optimizing spaces for the research community.

#### 4.2.2 Other electro-optic devices

The superior EO effect of LN is not only limited to the modulator application, as it can also be extended to various other kinds of application scenarios. One of the key benefits that may result from the development of TFLN is that a variety of different components can be integrated on the same chip to enable more functionality overall. The physics behind them is generally the same as EO modulators, which is by changing the material refractive index and thus the phase. Some typical EO-based applications demonstrated on TFLN platform have been summarized here.

First, the fast EO tuning features can be used in optical fiber communication or optical interconnects. For example, Fig. 12(a) shows EO tunable interleavers,<sup>297</sup> which can be used as tunable filters or wavelength-selective switches. Their measured tuning sensitivity is  $\sim 18$  [Fig. 12(b)] and  $\sim 16$  pm/V [Fig. 12(c)] for TE and TM modes, respectively. Compared with TO-based tuning, EO tuning enables a much higher speed and thus has broader application perspectives.

Second, the EO effect of LN can also be used for controlling the optical frequency, which enables broad applications, such as advanced photonic computation and frequency-domain photonic quantum computers.<sup>298,299</sup> Figure 13(a) shows an example of a programmable photonic two-level system for controlling gigahertz microwave signals, and its working principle is

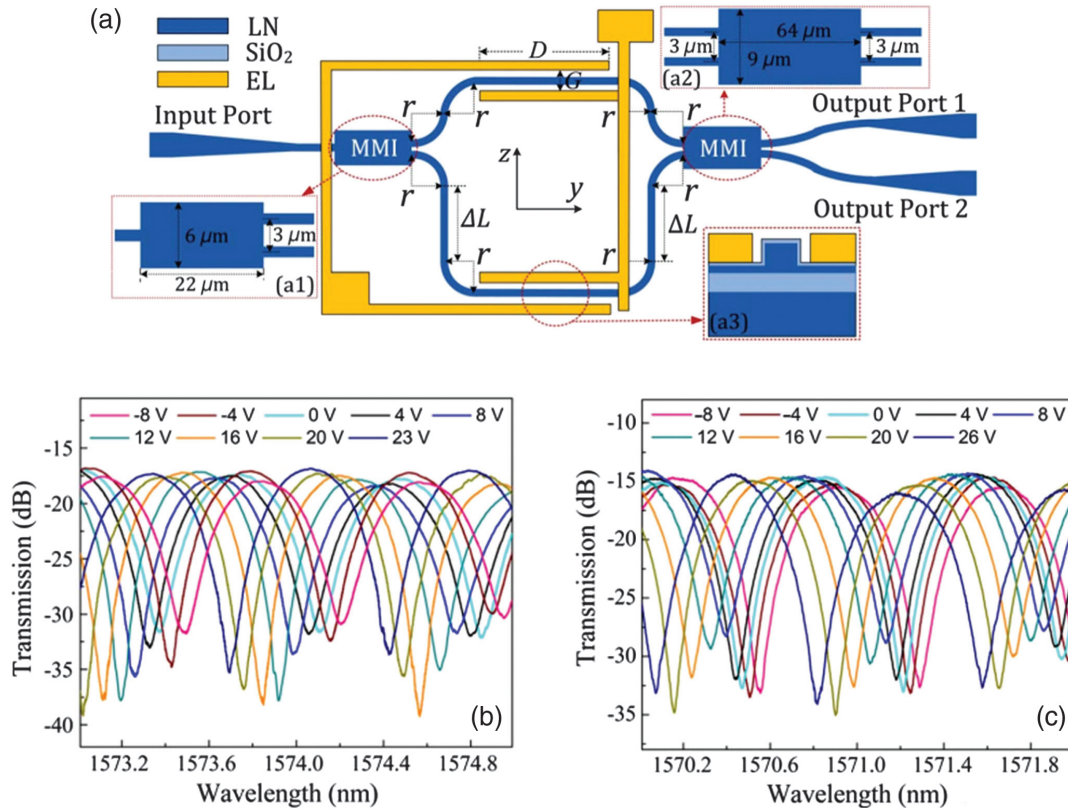


**Fig. 12** EO tunable interleaver in TFLN. (a) Schematic structure of TFLN waveguide interleaver, and its measured tunable transmission spectra for (b) TE and (c) TM polarized input light. (a)–(c) Adapted with permission from Ref. 297 © 2018 OSA.

shown in Fig. 13(b).<sup>298</sup> Benefits from the low loss TFLN ring resonator and cointegrated microwave electrode, the authors have demonstrated >30 GHz electrical bandwidth, around 0.5 GHz/V modulation efficiency, and ~2 ns photon lifetime.<sup>298</sup> Figures 13(c)–13(e) show another example of an on-chip EO frequency shifter for frequency controlling using only a single-tone microwave signal.<sup>299</sup> In that work, the authors have realized frequency shifts as high as 28 GHz with an approximately 90% on-chip conversion efficiency (CE) and >0.99 shift ratio (defined as the ratio of the output power at the shifted frequency and the output power inside the bus waveguide). Both works pave the way of efficiently and precisely manipulating light on gigahertz frequency, and open doors to many application scenarios.

Third, an LN-based microwave to optical transducer for quantum networks is another application scenario, especially under the conditions of rapidly developed quantum computation and long-haul quantum communication systems.<sup>300–302</sup> The typical microwave to optical conversion is based on electro-optomechanics (EOM) in a bulk optical cavity, which is difficult to operate at the quantum ground state as the mechanical cavity has a limited frequency.<sup>302,303</sup> An LN with the large Pockels effect enables GHz microwave to optical photons conversion and thus attracts significant attention. Holzgrafe et al. used the EO effect in coupled TFLN microrings, realizing an efficient microwave-to-optical transducer [Fig. 14(a)].<sup>300</sup> Its measured on-chip transduction efficiency is up to  $(2.7 \pm 0.3) \times 10^{-5}$  [Fig. 14(b)], which can be used to link up superconducting quantum devices

with optical fibers. McKenna et al. demonstrated a similar microwave-to-optical transducer,<sup>301</sup> and the TFLN sits on a sapphire platform. Its device structure is shown in Fig. 14(c), which consists of triple resonators. According to the measured results shown in Fig. 14(d), such a device converts microwave photons to optical photons with an on-chip efficiency of around  $6.6 \times 10^{-6}$ . More recently, Xu et al. demonstrated an improved CE up to 1.02% in coupled ring resonators,<sup>302</sup> as shown in Figs. 14(e) and 14(f). Such an improvement is realized using an air-cladding structure to mitigate the prominent photorefractive (PR) effect, which is supposed to be the main limiting factor of CE.<sup>302</sup> Even though the highest CE in TFLN is still under expectation considering its high Pockels effects, we believe the gap between a typical EOM-based scheme (highest CE of 47%<sup>305</sup>) and a TFLN-based EO structure [currently of  $(2.7 \pm 0.3) \times 10^{-5}$ <sup>300</sup> or  $6.6 \times 10^{-6}$ <sup>301</sup>] can be further narrowed down by optimizing the design and fabrication technology. TFLN-based integrated transducers will play a significant role in future quantum networks.

The last example is a dynamic integrated Fourier-transform spectroscopy based heterogeneously integrated SiN on LN hybrid structure (detail about such integration technology can be found in Sec. 3.3), and its device details are shown in Fig. 15,<sup>171</sup> where the EO properties of TFLN have been exploited for retrieving a complete spatial interferogram. This prototype device is capable of completely sampling the standing waves from signals over a 500-nm bandwidth. Using such a device, the authors have demonstrated a measured interferogram

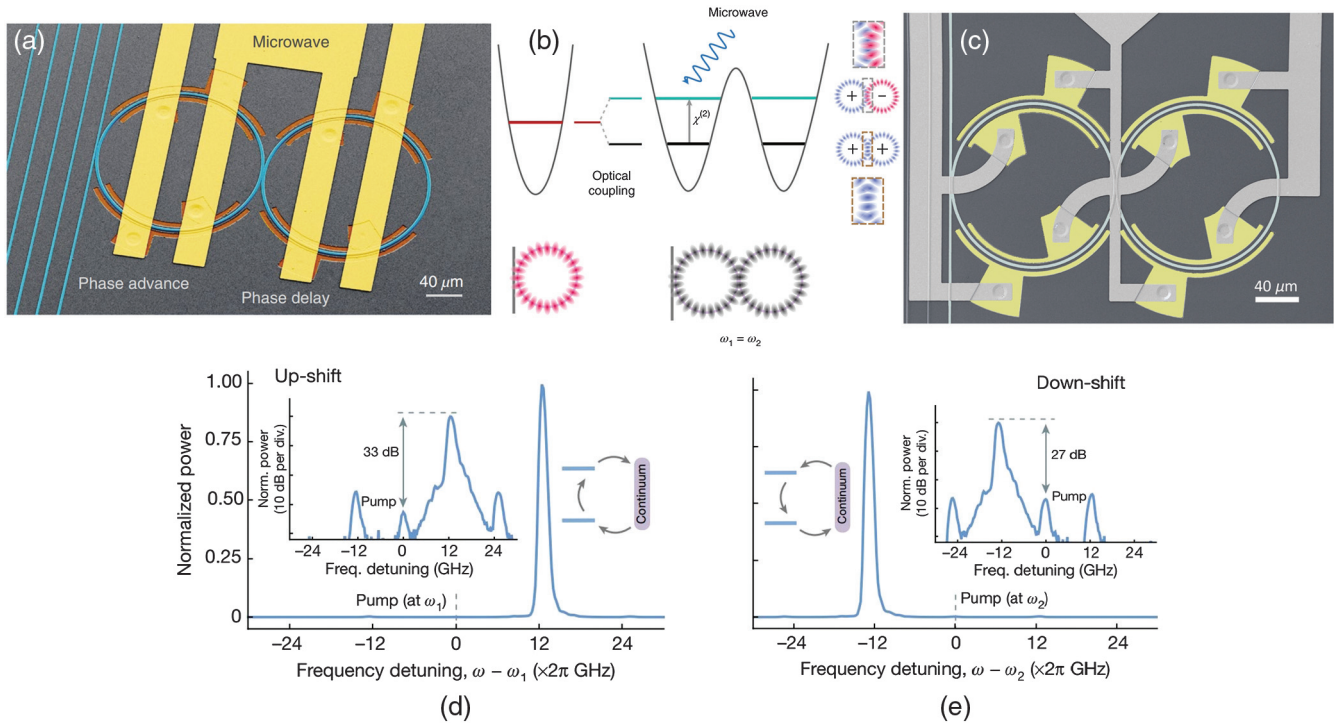


**Fig. 13** TFLN-based EO devices for optical frequency controlling. (a) False colored SEM image of an EO tunable coupled microring resonator. (b) The programmable photonic molecule consists of a pair of identical coupled rings (resonant frequency  $\omega_1 = \omega_2$ ). Such a system has two distinct energy levels: symmetric (blue/blue shading) and antisymmetric (red/blue) optical modes are spatially out of phase by  $\pi$ . The microwave field interacts with the two-level system through the large EO effect of TFLN. (a) and (b) Adapted with permission from Ref. 298 © The Author(s), under exclusive license to SNL 2018. (c) SEM image of a reconfigurable electro-optic frequency shifter. (d) Upshift and (e) downshift under 12.5 GHz microwave frequency and at 1601.2 nm wavelength ( $\omega_1$ ) show measured 80% CE and >0.99 shift ratio (defined as the ratio of the output power at the shifted frequency and the output power inside the bus waveguide). Inset shows the directions of energy flow and the spectra in dB scale. (c)–(e) Adapted with permission from Ref. 299 © The Author(s), under exclusive license to SNL 2021.

for a broadband optical signal from a super-luminescent light emitting diode, which has a 1550 nm center wavelength and a 50 nm 3 dB bandwidth. The above-discussed results are just a few examples based on the EO effect of LN for extended applications. We believe the applications are not limited to these and more advanced devices/PICs will be demonstrated in the future.

#### 4.3 Nonlinear and Quantum Photonic Devices

LN is also an excellent platform for various nonlinear and quantum photonic applications due to its significant nonlinear effects. In typical bulk LN, nonlinear applications are mainly limited to areas of frequency conversion. For TFLN, on the other hand, due to the convenience of dispersion engineering, some applications such as optical frequency comb and supercontinuum generations typically demonstrated on silicon photonics platforms can also be realized with superior performance contributed by its improved confinement and better overlap with light.

The nonlinear dynamics in both bulk LN and TFLN need to satisfy the phase-matching condition for conservation of momentum, which can be achieved using birefringent phase

matching.<sup>80</sup> Such a method is difficult to realize in both bulk LN and TFLN waveguide structures and has lots of challenges, such as low effective nonlinear effects and inconvenient phase-matching temperatures and angles.<sup>304</sup> An alternative method is called quasiphasematching (QPM) and can be realized by periodically inverting (poling) LN ferroelectric domains to point alternatively to the  $+c$  and  $-c$  directions to form PPLN.<sup>80</sup> Compared with bulk LN, an advantage of TFLN structures is their flexibility in dispersion engineering by varying the waveguide dimension,<sup>55,79</sup> which provides an additional degree of freedom for fine-tuning the phase-matching condition.

LN-based devices for nonlinear and quantum photonic applications are summarized in Table 6. One of the main categories is frequency conversion, which can be realized either by frequency upconversion with SHG,<sup>12,13,54–56,58–61,63,65,66</sup> SFG,<sup>67,68</sup> and THG<sup>62,69</sup> or by frequency downconversion with DFG.<sup>44</sup> In bulk LN-based devices, their bending loss is typically large due to the small refractive index contrast available, and thus results in a large device size and also degrades the interaction between the light and nonlinear medium. For example, the CE of SHG in bulk PPLN is usually at the level of 600%/( $W \cdot \text{cm}^2$ ).<sup>12</sup> In contrast, a nanophotonic thin film periodically poled lithium

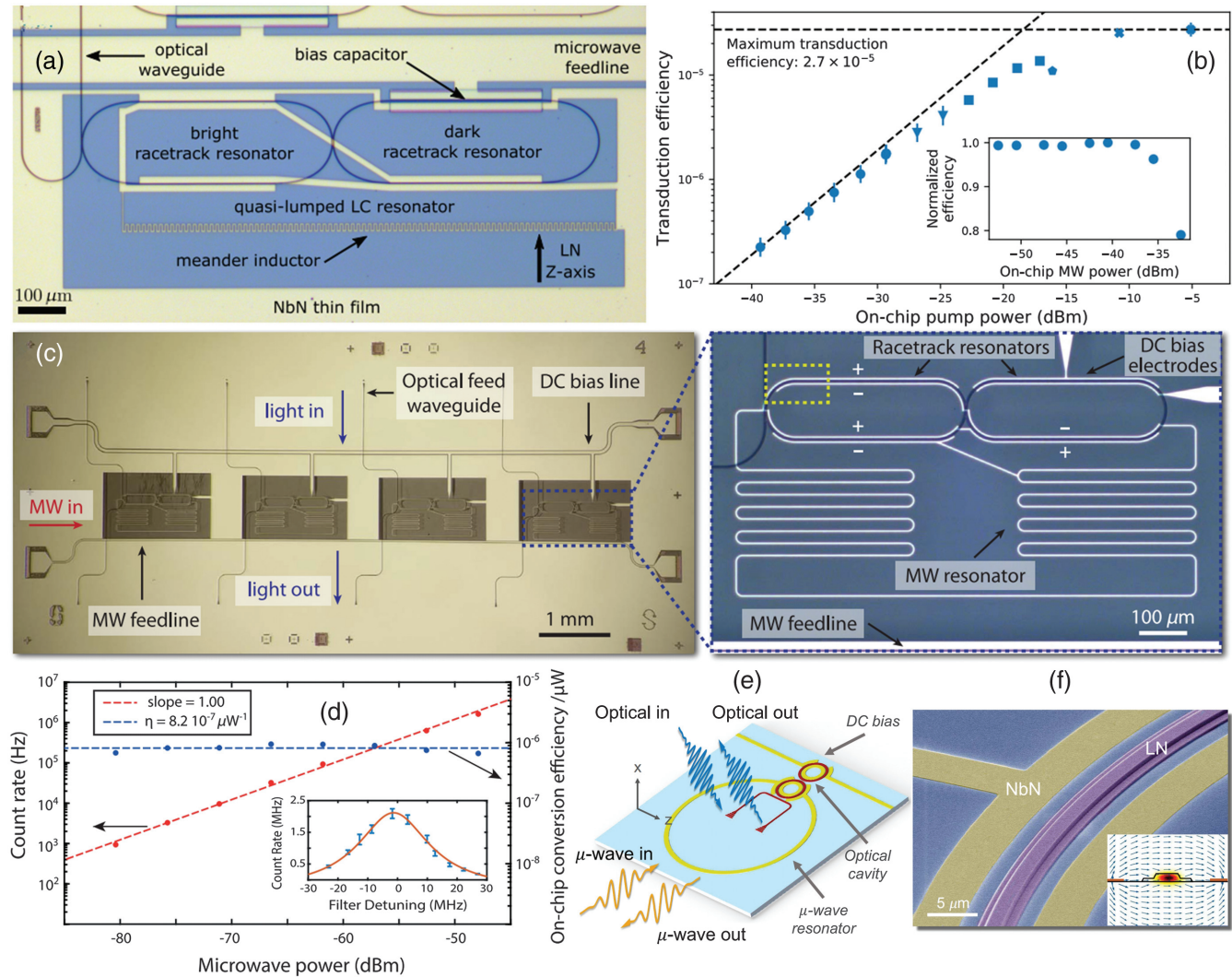


**Fig. 14** EO-based microwave to optical transducer in TFLN. (a) Microscopic image of a TFLN-based transducer, and (b) its corresponding measured maximum transduction efficiency with respect to optical pump powers. (a) and (b) Adapted with permission from Ref. 300 © 2020 OSA. (c) Microscopic image of a triply resonant LN on sapphire transducer (zoom in: device details), and (d) its measured photon count rate versus microwave drive frequency with respect to different input microwave powers. (c) and (d) Adapted with permission from Ref. 301 © 2020 OSA. (e) Schematic of an EO converter in TFLN based on two coupled microring resonators (red) and a cointegrated superconducting resonator (yellow). DC bias is applied for optical mode tuning. (f) False color SEM image of the EO converter detail. Inset is the electric field distribution. (e) and (f) Adapted with permission from Ref. 302.

niobate (TFPPLN) waveguide can have CE as high as  $2600\%/(\text{W} \cdot \text{cm}^2)$ .<sup>58</sup> Assisted by a high- $Q$  cavity, a high CE of  $250,000\%/W$  SHG has been demonstrated in a periodically poled TFLN microring,<sup>63</sup> as shown in Figs. 16(a)–16(c). Such a record ultrahigh CE is achievable from the ultralow loss/ultrahigh  $Q$  factor ( $\sim 10^5$ ) microring resonator fabricated on a TFLN wafer with a large refractive index contrast. With future development of LN patterning and etching technologies, as well as material quality, an even higher CE can be expected on LN platforms. For example, as discussed in Sec. 4.1.1, the  $Q$  factor can be improved up to around  $10^8$  using an optimized patterning technology,<sup>224</sup> which would enable a greater nonlinear interaction of the optical field with the LN crystal. In

addition, metasurface structures can also be used to improve nonlinear conversion in TFLN.<sup>306</sup> Some experimental results will be summarized and introduced in Sec. 4.6.2. It is worth mentioning that devices in thicker (several micron-thick) LN films have some advantages in high-power frequency conversion, such as watt-level frequency generation, as they exhibit a higher power damaging threshold compared with submicron film-based devices. As shown in Table 6, around 1 W of second harmonic can be generated in a thicker LN film,<sup>153,154</sup> using the lapping and polishing method (details in Sec. 3.2.2). The larger waveguide core also enables high global efficiency (considering insertion loss) due to its larger mode profile.<sup>29,30,148–154</sup>

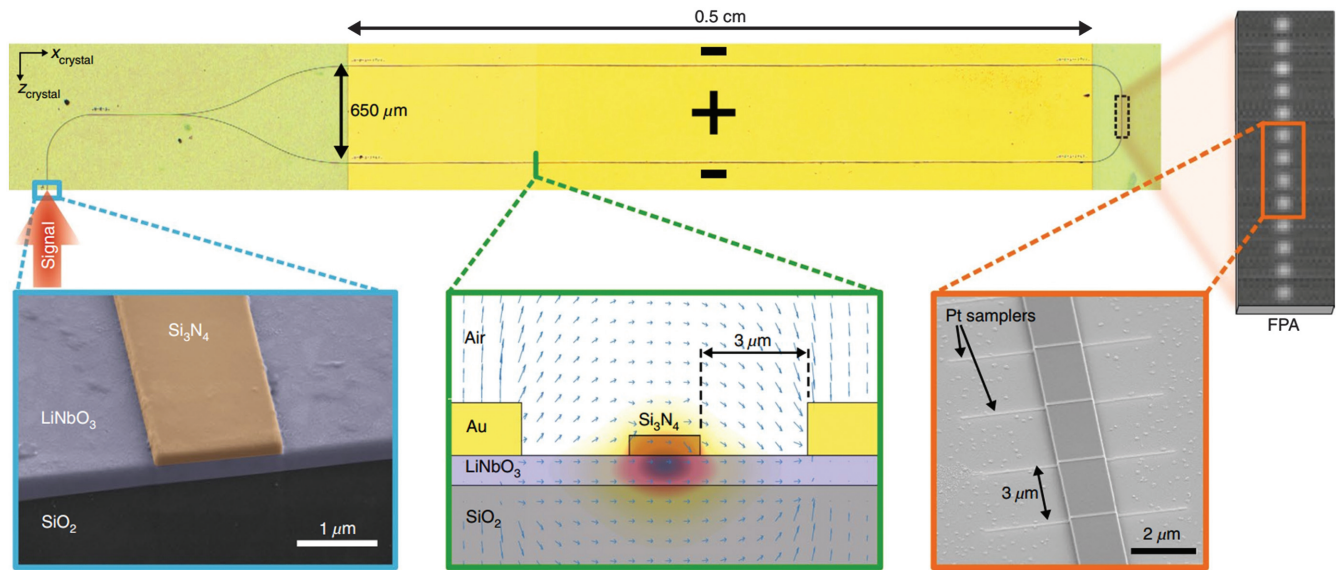


**Fig. 15** EO waveguide spectrometer in TFLN. Microscopic image and device details of an EO TFLN waveguide spectrometer. Adapted with permission from Ref. 171 © The Author(s), under exclusive license to SNL 2019.

The optical frequency comb with periodic optical frequency lines has also been demonstrated in the TFLN platform<sup>77</sup> while it is typically difficult to realize in bulk LN. Based on a dispersion-engineered microring with a high  $Q$  factor, Kerr comb generation has been demonstrated in the TFLN platform.<sup>63,74,75</sup> Figure 16(d) shows one example of an on-chip photonic integrated circuit (PIC) containing both Kerr comb generation and filtering.<sup>76</sup> The microresonator frequency comb generator is based on the third order ( $\chi^{(3)}$ ) nonlinear effect, while the add-drop filter is based on the second-order ( $\chi^{(2)}$ ) EO effect. Its generated comb has a line spacing of  $\sim 250$  GHz, and spans of  $\sim 300$  and  $\sim 700$  nm for TM and TE modes, respectively. Compared with a third-order nonlinearity-based comb, an EO phase modulation-based comb features high stability and controllability, which has also been demonstrated in the TFLN platform.<sup>77</sup> Such an EO comb is based on ring modulators and has over 80 nm bandwidth and more than 900 comb lines with a slope of 1 dB/nm, as shown in Fig. 16(e). Both the Kerr and EO combs show that TFLN is an excellent platform for comb generation.

TFLN can also be used for supercontinuum generation based on its second- and third-order nonlinear effects. Figure 16(f) shows an example of a supercontinuum spanning 2.58 octaves using dispersion-engineered TFLN waveguides. Its performance is highly related to the waveguide geometries. Benefiting from its large refractive index contrast, dispersion engineering becomes easy and more demonstrations on comb and supercontinuum generations can thus be expected.

Based on the strong second-order nonlinearity in TFLN, a broadband OPA<sup>70</sup> and an ultralow threshold OPO<sup>71</sup> have also been realized in dispersion-engineered TFLN devices. Figure 16(g) shows the principle of OPA in dispersion-engineered periodically poled TFLN waveguides. The general idea is to do engineering on the waveguide for low group velocity dispersion and group velocity mismatch, and thus maximize OPA performance.<sup>70</sup> According to the measured results, broadband phase-sensitive amplification is larger than 45 dB/cm for a 2.5-mm long waveguide with pump pulse energy of only

0.8 pJ. Such a result paves the way for chip-based light sources.<sup>70</sup> Raman scattering is another important nonlinearity and has been widely explored in other materials systems. Yu et al. demonstrated multiwavelength Raman lasing in a TFLN microring and analyzed the underlying physical process,<sup>73</sup> which provides guidance for TFLN-based SRS dynamics.

In addition to the above classical applications, LN is ideally suited for quantum applications based on its large nonlinearity, such as photon pair generation.<sup>15,80–83,149</sup> Although bulk LN has been used for quantum applications for a long time, the recently developed TFLN makes integrated and higher-efficiency devices possible. Figures 16(h)–16(j) show an example of a quantum photon source based on a TFLN microring.<sup>81</sup> Its measured photon pair generation rate (PGR) is around 36.3 MHz using 13.4  $\mu$ W pump power, while its measured coincidence to accidental ratio (CAR) is above 100 at high rates and reaches  $14,682 \pm 4427$  at a low pump power. Both of these values are much higher than previous reported results, and such benefits mainly come from having highly confined TFLN devices together with the superior nonlinear effect. In general, with the development of recent advances in the TFLN platform, advantages of LN with its large  $\chi^{(2)}$  and  $\chi^{(3)}$  are increasingly being exploited. It is believed that many new phenomena and applications will be demonstrated based on the unique nonlinear properties of LN and will further contribute to the development of quantum photonic devices.

#### 4.4 AO Devices

LN is also an ideal platform for the demonstration of AO devices due to its large photo-elastic constant,<sup>2</sup> as such devices can be used in the area of optical networking and signal processing.<sup>16</sup> For a long time, surface acoustic wave (SAW) derived AO devices have been extensively explored in bulk LN in combination with Ti diffusion/PE technology.<sup>307</sup> Due to the weak mode confinement caused by the poor refractive index contrast available with those technologies, the interaction between the

**Table 6** Summary of LN-based devices for nonlinear and quantum photonic applications. MgLN, MgO-doped lithium niobate; ZnLN, Zn-doped lithium niobate; ZnOLN, ZnO-doped lithium niobate; PE, proton exchange; HI, heterogeneous integration; PIC, photonic integrated circuit; N.A., not available/applicable.

Year	Cut	Type	Application	Performance	Fabrication	Ref.
1993	Z-cut	Bulk PPLN WG	SHG	CE: 600%/(W · cm <sup>2</sup> )	PE and electrical poling	12
1996	Z-MgLN	Bulk PPLN WG	SHG	CE: 4.5%/(W · cm <sup>2</sup> ) <sup>a</sup>	Wet etching and electrical poling	13
2002	N.A.	Bulk PPLN WG	Photon-pair	CE: 2 × 10 <sup>-6</sup>	PE and electrical poling	80
2004	N.A.	Bulk PPLN WG	SFG	CE: 330 ± 10%/(W · cm <sup>2</sup> )	PE	67
2006	Z-ZnLN	TFPPLN ridge	SHG	CE: 370%/(W · cm <sup>2</sup> )	Lapping and polishing, dicing	29
2009	Z-MgLN	Bulk PPLN disk	THG	CE: 1.5%/W <sup>2</sup>	Mechanical polishing	69
2010	Z-ZnOLN	TFPPLN ridge	SHG	CE: 2400%/W	Lapping and polishing, dry etching	30
2016	Y-MgLN	TFPPLN ridge	SHG	CE: 189%/(W · cm <sup>2</sup> ); output power: 0.86 W	Lapping and polishing	152
2016	X-cut	TFPPLN WG	SHG	CE: 160%/(W · cm <sup>2</sup> )	HI and electrical poling	54
2016	ZnLN	TFPPLN ridge	Photon-pair	Rate: 1456 Hz/μW; efficiency: 64.1%	Lapping and polishing	149
2016	Z-cut	TFPPLN ridge	SHG	CE: 204%/W	Lapping and polishing, dicing	148
2017	Z-MgLN	TFPPLN	SFG	CE: 3.3%/W; BW: 15.5 nm	HI and bonding	305
2017	X-cut	TFLN WG	SHG	CE: 1660%/(W · cm <sup>2</sup> ); phase matching free	Ar ICP-RIE	55
2017	X-cut	TFLN WG	SHG	CE: 41%/(W · cm <sup>2</sup> )	Ar ICP-RIE	56
2018	N.A.	TFPPLN ridge	Comb	Mid-infrared span	Lapping and polishing	150
2018	X-MgLN	TFPPLN WG	SHG	CE: 2600%/(W · cm <sup>2</sup> )	Ar ICP-RIE and electrical poling	58
2019	X-cut	TFLN WG	SHG	CE: 1160%/(W · cm <sup>2</sup> )	HI	59
2019	X-MgLN	TFPPLN ring	SHG	CE: 230,000%/W	Ion-milling and electrical poling	60
2019	X-cut	TFLN WG	SHG	CE: 2200%/(W · cm <sup>2</sup> )	Ion-milling and electrical poling	61
2019	X-cut	TFLN disk	SHG; THG	SHG: 9.9%/mW; THG: 1.05%/mW <sup>2</sup>	Femtosecond-laser ablation and FIB polishing	62
2019	Z-cut	TFPPLN ring	SHG	CE: 250,000%/W	Ar etching and electrical poling	63
2019	Z-cut	TFLN WG	SCG	Span: 1.5 octaves	Ar ICP	78
2019	Z-cut	TFPPLN ridge	SFG	CE: 85%/W	Lapping and polishing, dicing	151
2019	X-cut	TFLN PIC	Comb	Comb generation and modulation (PIC)	Ar ICP-RIE	76
2019	X-cut	TFLN WG	SCG	Span: 2.58 octaves	Ar ICP-RIE	79
2019	X-cut	TFLN ring	Comb	Span: >80 nm	Ar ICP-RIE	77
2019	MgLN	TFPPLN ridge	SHG	CE: 6.29%/(W · cm <sup>2</sup> ); output power: 1.1 W	Lapping and polishing, dicing	154
2020	N.A.	TFLN disk	SHG	CE: 10 <sup>-2</sup> % (282.7 nm)	Simulation	306
2020	Z-cut	TFPPLN ring	Photon-pair	PGR: 36.3 MHz; CAR: >100	Ion-milling and electrical poling	81
2020	X-cut	TFLN WG	SHG	CE: 3061%/(W · cm <sup>2</sup> )	ICP and electrical poling	65
2020	Z-cut	TFLN disk	SFG	CE: 2.22 × 10 <sup>-6</sup> /mW	FIB and wet etching	68
2020	X-cut	TFLN ring	SRS	Pump-to-Stokes CE: 46%	Ar ICP-RIE	73
2020	X-MgLN	TFPPLN WG	Photon-pair	PCR: 11.4 MHz; CAR: 668	Electrical poling	82
2021	X-MgLN	TFPPLN WG	OPA	Amplification: >45 dB/cm	Ar etching and electrical poling	70
2021	Z-cut	TFPPLN ring	OPO	Threshold: ~30 μW; CE: 11%	Ar ICP-RIE and electrical poling	71
2021	Z-cut	TFPPLN ridge	SHG	CE: 22%/(W · cm <sup>2</sup> ); output power: 1 W	Lapping and polishing, dicing	153
2021	X-MgLN	TFPPLN WG	DFG	CE: 200%/(W · cm <sup>2</sup> )	Ar etching and electrical poling	44
2021	X-cut	TFPPLN WG	SHG	CE: 435.5%/(W · cm <sup>2</sup> )	ICP and electrical poling	66
2021	X-cut	TFPPLN WG	Photon-pair	Rate: 2.79 × 10 <sup>11</sup> Hz/mW; SHG: 2270%/(W · cm <sup>2</sup> )	ICP and electrical poling	83

<sup>a</sup>Calculated based on reported data.

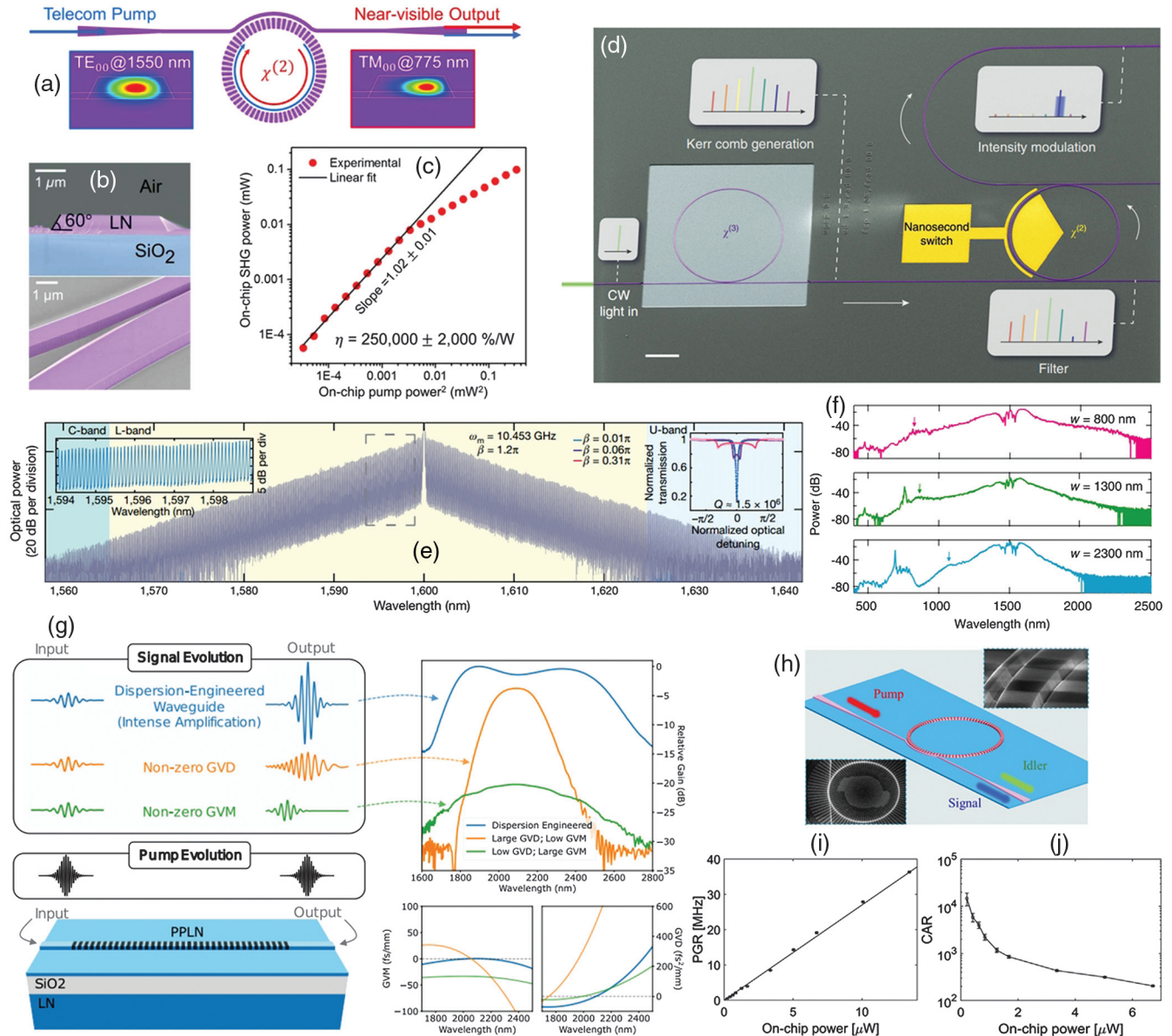


**Fig. 16** LN-based nonlinear and quantum photonic devices. (a) Schematic structure of the TFPPN microring. (b) False-color SEM images of the device cross section and coupling region detail. (c) Experimentally measured SHG power versus pump power. (a)–(c) Adapted with permission from Ref. 63 © 2019 OSA. (d) False color SEM image of TFLN PIC containing Kerr comb and EO add-drop filter. Adapted with permission from Ref. 76. (e) Measured transmission spectrum of the EO comb. Left inset shows a magnified view of several comb lines. Right inset shows measured transmission spectrum for several different modulation indices. Adapted with permission from Ref. 77 © The Author(s), under exclusive license to SNL 2019. (f) Measured transmission spectra with respect to different waveguide width. Adapted with permission from Ref. 79 © 2019 OSA. (g) Principle of OPA in dispersion engineered PPLN waveguide and simulated relative gain spectrum for three dispersion cases. Adapted with permission from Ref. 70 © 2022 OPTICA. (h) Schematic structure of the PPLN microring. Insets are the SEM images of the device details. Measured (i) PGR and (j) CAR. (h)–(j) Adapted with permission from Ref. 81 © 2020 American Physical Society (APS).

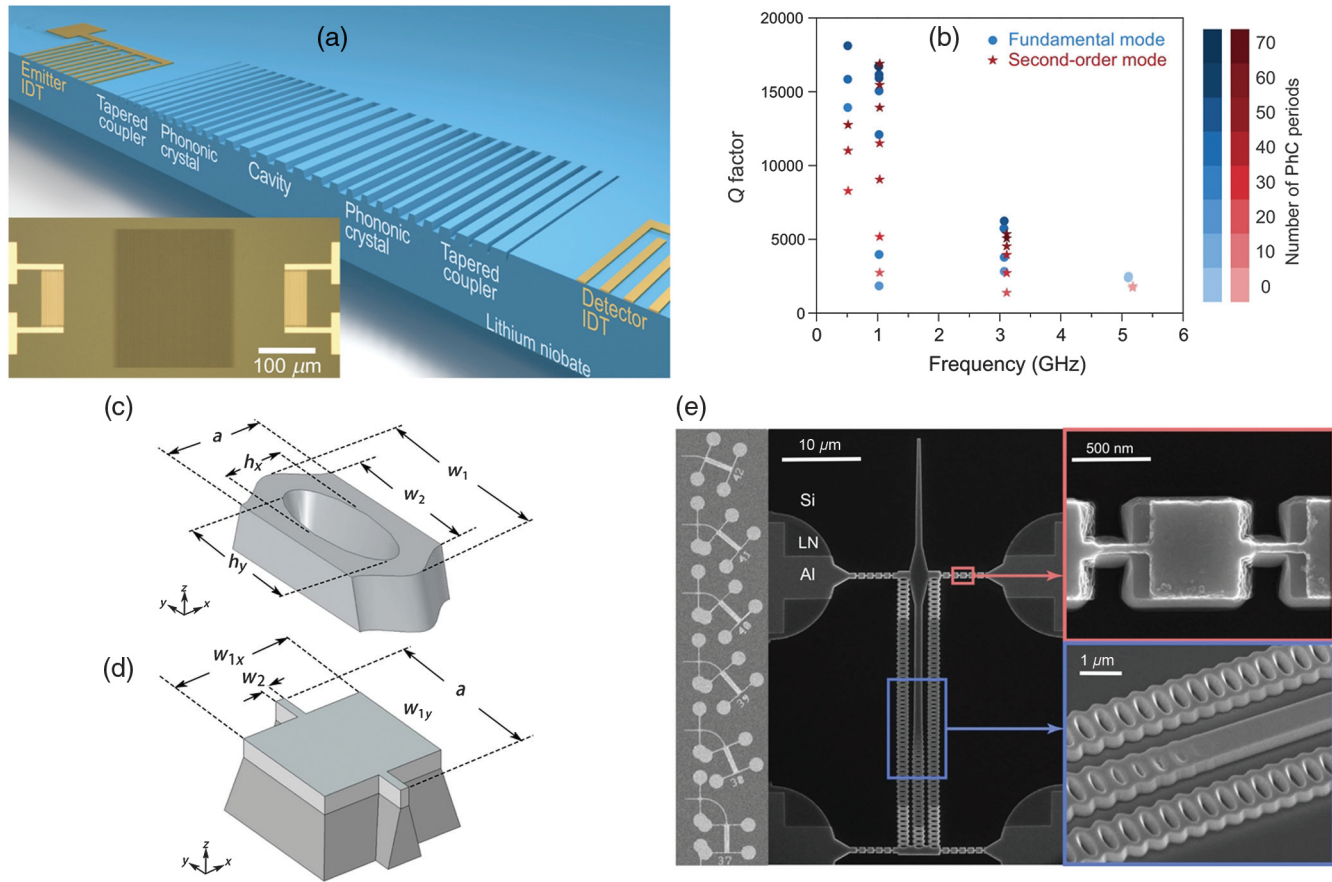


**Fig. 17** Cavity optomechanics devices in LN. (a) Schematic of a band structure engineered surface acoustic resonator on TFLN. Inset is the microscopic image of the fabricated device. (b) Measured  $Q$  factor with respect to different resonator frequencies. (a) and (b) Adapted with permission from Ref. 311 © 2019 APS. Unit cell geometries of the (c) nanobeam optomechanical crystal and (d) 1D photonic shield. (e) SEM image of a 1D PhC cavity resonator for optomechanical mode generation. Left: full view of the device. Middle: top view of one device. Top right: top view of the 1D photonic shield region. Bottom right: SEM image of the nanobeam reflector coupling region. (c)–(e) Adapted with permission from Ref. 310 © 2019 OSA.

transmitted light and acoustic waves is not as high as desired. The recently developed TFLN platform provides an attractive choice for integrated AO devices. In 2010, Kadota et al. realized a high-frequency (4.5 and 6.3 GHz) Lamb wave resonator using direct  $c$ -axis TFLN by the CVD method,<sup>308</sup> which validates TFLN's advantages for AO devices. In this part, we will focus on the latest results about TFLN-based AO devices. Selected bulk LN-based results will also be covered for comparison.

#### 4.4.1 Cavity optomechanics

Benefiting from commercially available high-quality TFLN and well-developed LN etching technologies, high  $Q$  factor and small phonon mode size SAW resonators at gigahertz frequencies have been demonstrated by the engineering of photonic band structures,<sup>197,309–311</sup> something that is inapplicable in the typical bulk LN platform. Figure 17(a) shows an SAW resonator based on chirping a quasi-1D PhC period, and its measured  $Q$  factor is 6240 at a fundamental mode frequency of 3.07 GHz [Fig. 17(b)], which results in an  $f \cdot Q$  product of  $2 \times 10^{13}$  Hz.<sup>311</sup> In another optimized PhC structure, as shown in Figs. 17(c)–17(e), a mechanical mode frequency close to

2 GHz with a  $Q$  factor of around 17,000 at 4 K was obtained, which corresponds to around  $3.4 \times 10^{13}$  Hz.<sup>310</sup> These demonstrated high  $f \cdot Q$  product optomechanics resonators pave the way toward hybrid quantum systems, enabling the control of solid-state electronic spins, AO modulators, gigahertz frequency optical comb generation, and performing microwave to optical conversion.<sup>17,311</sup>

#### 4.4.2 Acousto-optic modulators

AO modulators have already been demonstrated in LN platforms.<sup>16,17,312,313</sup> Different from high speed EO modulators, AO modulators can be enhanced by a mechanical quality factor with bandpass frequency selectivity and also have no critical requirement of placing interdigitated transducers (IDTs) close to the optical waveguide, since acoustic waves have a low propagation loss.<sup>312</sup> Thus, AO modulators can be a good complement to existing EO modulators.

Surface elastic waves can be generated by mechanical coupling of a shear or compressional wave transducer.<sup>314</sup> However, for better interaction between acoustic and optical waves, the IDT structure is more frequently used.<sup>314</sup> Figure 18(a) shows

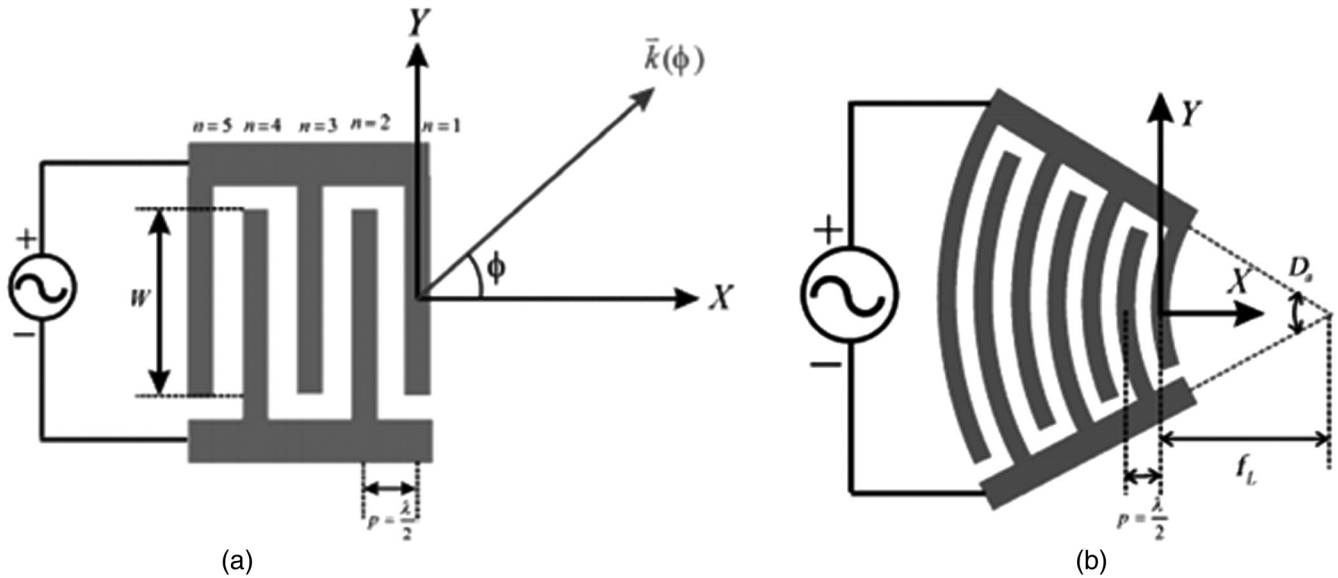


**Fig. 18** Design of IDTs. Schematics of (a) straight and (b) concentric IDTs. (a) and (b) Adapted with permission from Ref. 315 © 2005 IEEE.

a typical straight IDT structure, which consists of spatially periodic electrodes. Its key metrics involve the finger length ( $W$ ), finger number ( $n$ ), and finger period ( $p$ ). Based on the angular spectrum of plane wave theory, the amplitude field of the IDT can be calculated.<sup>315</sup> To further improve the acoustic–photonic interaction, a concentric IDT is proposed, as shown in Fig. 18(b). In such a structure, the interdigitated electrodes are designed with circular arc shapes and hence can achieve higher intensity acoustic fields.<sup>315,316</sup>

AO devices have been demonstrated in bulk LN platform. In 1992, Cheng et al. demonstrated an AO frequency shifter with a measured 121 MHz tunable bandwidth (center frequency is 0 MHz) in the visible band based on Y-cut bulk LN.<sup>317</sup> Passive waveguides are formed through Ti diffusion; thus, the device volume is typically in the cubic centimeter range. Kakio et al. demonstrated an AO modulator in a 128-deg rotated Y-cut LN crystal. Under a 17 V and 195 MHz driving voltage, about 84% diffractive efficiency was obtained.<sup>318</sup> Similarly, such a device is based on a Ti diffused waveguide and thus presents a large device size (with an IDT length of 2 or 3 mm). In addition, due to the large device size in bulk LN, the modulation frequency is typically limited to several hundreds of megahertz. The TFLN platform can compensate for these drawbacks and thus realize more compact and efficient AO devices.<sup>312,313,319,320</sup>

Figures 19(a)–19(c) show both MZI and microring-based AO modulators in a TFLN platform, which uses IDTs for launching the SAW to reduce reflection losses.<sup>16</sup> The photoelastic coefficient  $p_{\text{eff}}$  was extracted to be 0.053 from experimental data, which agrees well with the theoretical value. Based on the acoustic optic resonator/modulator, high-performance microwave to optical conversion has been demonstrated in TFLN.<sup>17</sup> As shown in Figs. 19(d) and 19(e), in a suspended IDT-coupled TFLN MZI AO resonator, enhanced microwave to optical conversion at 2.24 and 3.33 GHz acoustic resonance modes is observed. From such an experimental result, the  $V_{\pi}$  is estimated to be around 4.6 V, and  $V_{\pi}L$  is around 0.046 V · cm (acoustic resonator length is 100  $\mu\text{m}$ ). It is known that the introduction of a resonant acoustic cavity will degrade the bandwidth of an AO

modulator, and Hassanien et al. demonstrated a wideband (140 MHz) operation AO modulator without using any acoustic cavity.<sup>312</sup> Its principle is shown in Fig. 19(f), which consists of a PhC waveguide for light confinement, and a split IDT designed to generate  $S_0$  mode Lamb waves. Such a device is power efficient, with phase shifts up to 0.0166 rad/ $\sqrt{\text{mW}}$  over a 45- $\mu\text{m}$  modulation length, and its measured bandwidth is up to 140 MHz under a 1.9 GHz center frequency [Fig. 19(g)]. More recently, photonics BIC has also been demonstrated to realize high-performance AO modulation.<sup>319,320</sup> As discussed in Sec. 3.3, BIC structures can realize low loss light transmission without the need for etching of TFLN and thus enable various integrated devices/circuits. Figure 19(h) shows an example of GHz AO modulation based on a photonics BIC waveguide.<sup>320</sup> Compared with a typical bulk LN device, the improved modulation frequency is a consequence of the reduced device size and enhanced acoustic–phonics interaction.

#### 4.4.3 Acoustic delay line

In addition, TFLN is also suitable for the fabrication of an acoustic delay line (ADL) that can be used for radio frequency (RF) acoustic signal processing.<sup>321</sup> By choosing the fundamental symmetrical ( $S_0$ ) mode, low IL and large fractional bandwidth (FBW) at a high frequency can be realized,<sup>321–323</sup> which overcomes the drawback of fundamental shear horizontal ( $SH_0$ ) mode<sup>313</sup> or first order antisymmetric ( $A_1$ ) mode-based devices.<sup>308</sup> Figures 20(a) and 20(b) show an optical image of a fabricated ADL in TFLN operating in the  $S_0$  mode, which realized 1 dB IL and 4.1% FBW at 300 MHz [Fig. 20(c)].<sup>321</sup>

#### 4.5 Rare Earth Doped Devices

Rare earth doped optical fibers (silica) have been used as optical amplifiers and lasers, which makes the great success of current fiber-optic communications systems possible.<sup>324,325</sup> Similarly, LN crystals can be doped with rare earth ions to realize integrated amplifiers and laser sources. Compared with the oxide materials, rare earth doped LN has more advantages as LN

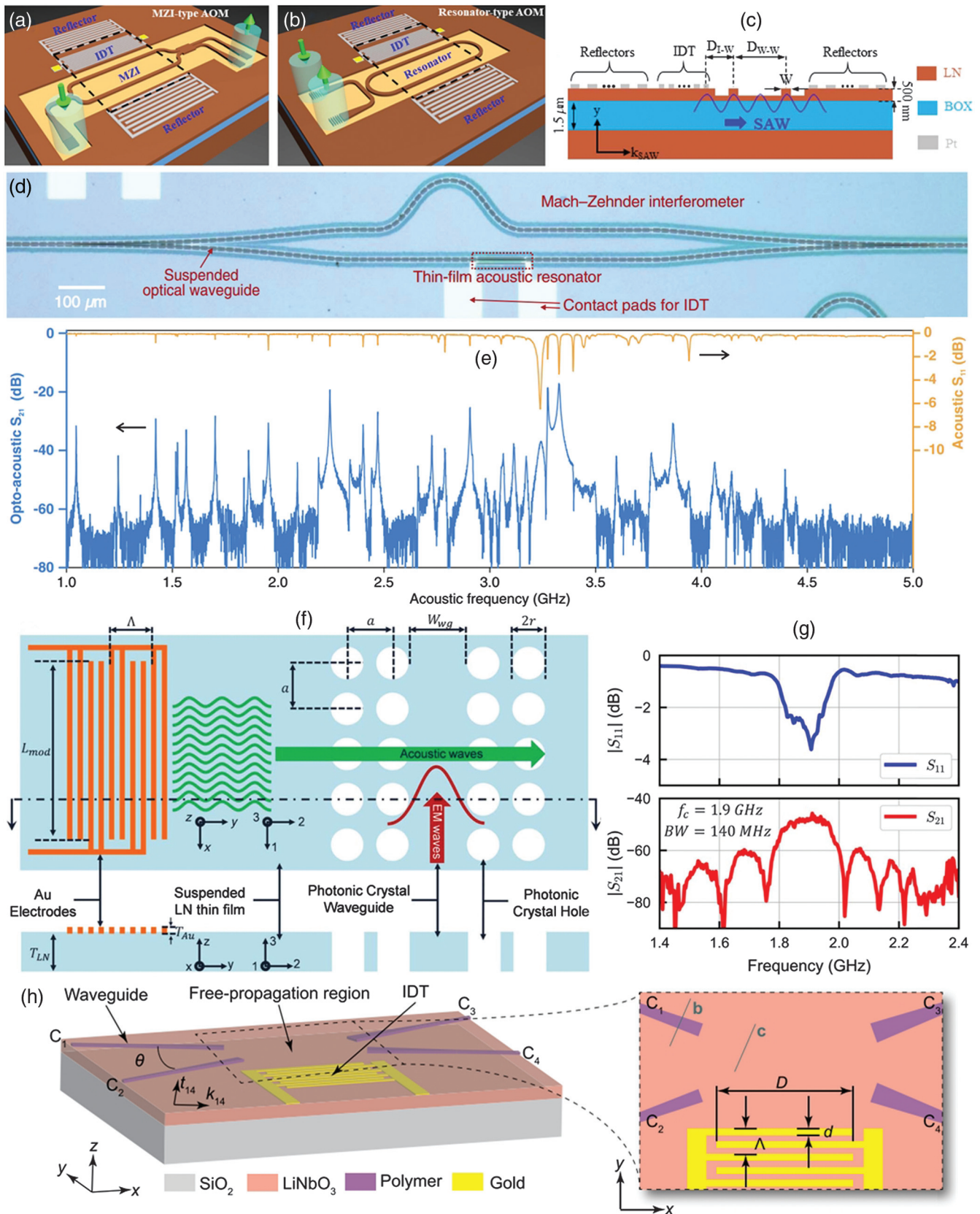


**Fig. 19** LN-based AO modulators. Schematics of (a) MZI and (b) microring type AO modulators. (c) Cross section of the AO modulator. (a)–(c) Adapted with permission from Ref. 16 © 2019 Chinese Laser Press (CLP). (d) Microscopic image of a suspended AO MZI. (e) S<sub>11</sub> and S<sub>21</sub> spectra of microwave to optical conversion. The optical power detected by photodetector (PD) is

**Fig. 19** (Continued) 0.25 mW. (d) and (e) Adapted with permission from Ref. 17 © 2019 OSA. (f) Principal illustration of one AO modulator without resonator cavity. (g) Measured  $S_{11}$  and  $S_{21}$  spectra. (f) and (g) Adapted with permission from Ref. 312 © 2021 CLP. (h) Schematic of AO frequency shifter based on photonic BIC. Adapted with permission from Ref. 320 © 2021 American Chemical Society (ACS).

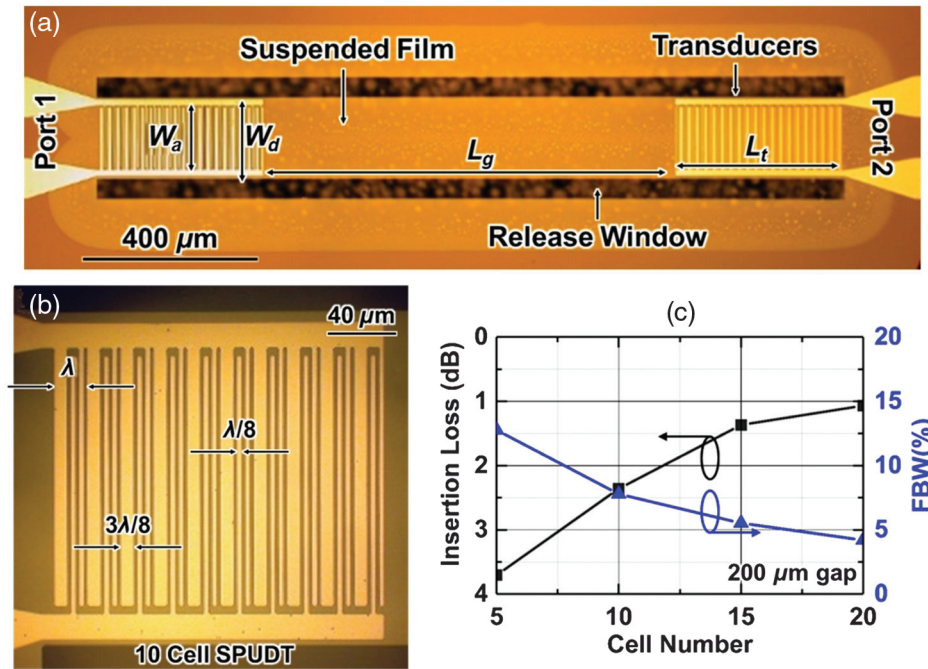


**Fig. 20** LN-based ADL. (a) Microscopic image of the fabricated ADL. (b) Microscopic image of zoomed in view of the device. (c) Extracted IL and FBW of ADLs with respect to cell numbers. (a)–(c) Adapted with permission from Ref. 321 © 2018 IEEE.

has various other unique features, as introduced in Sec. 2. By incorporating these functions together, many different devices can be fabricated on the same chip. With recently developed TFLN technology, a chip scale PIC simultaneously containing integrated lasers/light emission, light modulation, amplification, routing, etc. is foreseeable in the near future.

#### 4.5.1 Rare earth doped bulk devices

In bulk LN crystals, rare earth doping has been explored for a long time.  $\text{Nd}^{3+}$  and  $\text{Er}^{3+}$  are the two main ions used for doping in Ti-diffused or PE bulk LN devices.<sup>91</sup> For a  $\text{Nd}^{3+}$  doped bulk LN device, the amplifier gain has been measured to be around 7.5 dB<sup>326</sup> and with a lasing threshold near 1.5 mW,<sup>327</sup> while in  $\text{Er}^{3+}$  doped and Ti-diffused bulk LN waveguides, a 13.8 dB gain<sup>328</sup> at 1531 nm and 8 mW<sup>329</sup> lasing threshold has been demonstrated. In these reported results, the device performance was not as good as expected and the main reason is likely poor optical mode confinement caused by a low refractive index contrast. TFLN provides an alternative for improved device performance in the future.

#### 4.5.2 Rare earth doped TFLN devices

Dutta et al.<sup>94</sup> demonstrated that  $\text{Tm}^{3+}$  doped TFLN exhibits identical optical lifetimes to those measured in bulk crystals,

as shown in Figs. 21(a)–21(c). Such a result opens the door to applications in rare earth doped TFLN. Many types of integrated amplifiers/lasers based either on microresonators or straight waveguides have been demonstrated successively.<sup>33,92,93,95,238,330–334</sup> Doping of rare earth ions can be either by implantation<sup>95</sup> or can take place during LN crystal growth.<sup>33,92–94,238,330–334</sup> Figures 21(d)–21(f) show one example of an  $\text{Er}^{3+}$  implanted TFLN device.<sup>95</sup> The researchers have shown that ion implantation damage can be repaired by postannealing. As can be seen from the measured results shown in Fig. 21(e), a  $Q$  factor up to  $9.2 \times 10^5$  can be measured after 550°C postannealing, and its mean value is  $5 \times 10^5$ . Other reports rely on high-quality TFLN with  $\text{Er}^{3+}$  doping achieved during crystal growth using CIS technology, which has been introduced in Sec. 2. Both high-performance amplifiers<sup>33,92,333</sup> and chip scale laser sources<sup>93,238,330–332,334</sup> have been realized in such a platform. On-chip optical amplification with an 18-dB internal net gain was obtained using a 3.6-cm TFLN waveguide [Figs. 21(g)–21(i)], where the pump wavelength is 980 nm.<sup>33</sup> Benefiting from the microring with an ultra-high  $Q$  factor ( $1.25 \times 10^6$  near 971.5 nm,  $4.27 \times 10^5$  near 1531.8 nm) in TFLN, an on-chip laser with  $\sim 20 \mu\text{W}$  threshold is realized [Figs. 21(j) and 21(k)], and differential CE was around  $6.61 \times 10^{-5}\%$ .<sup>330</sup> In addition, these chip scale lasers also enable an emission wavelength tuning either by changing the pump power<sup>93</sup> or using the EO effect of LN.<sup>334</sup> Wang et al.

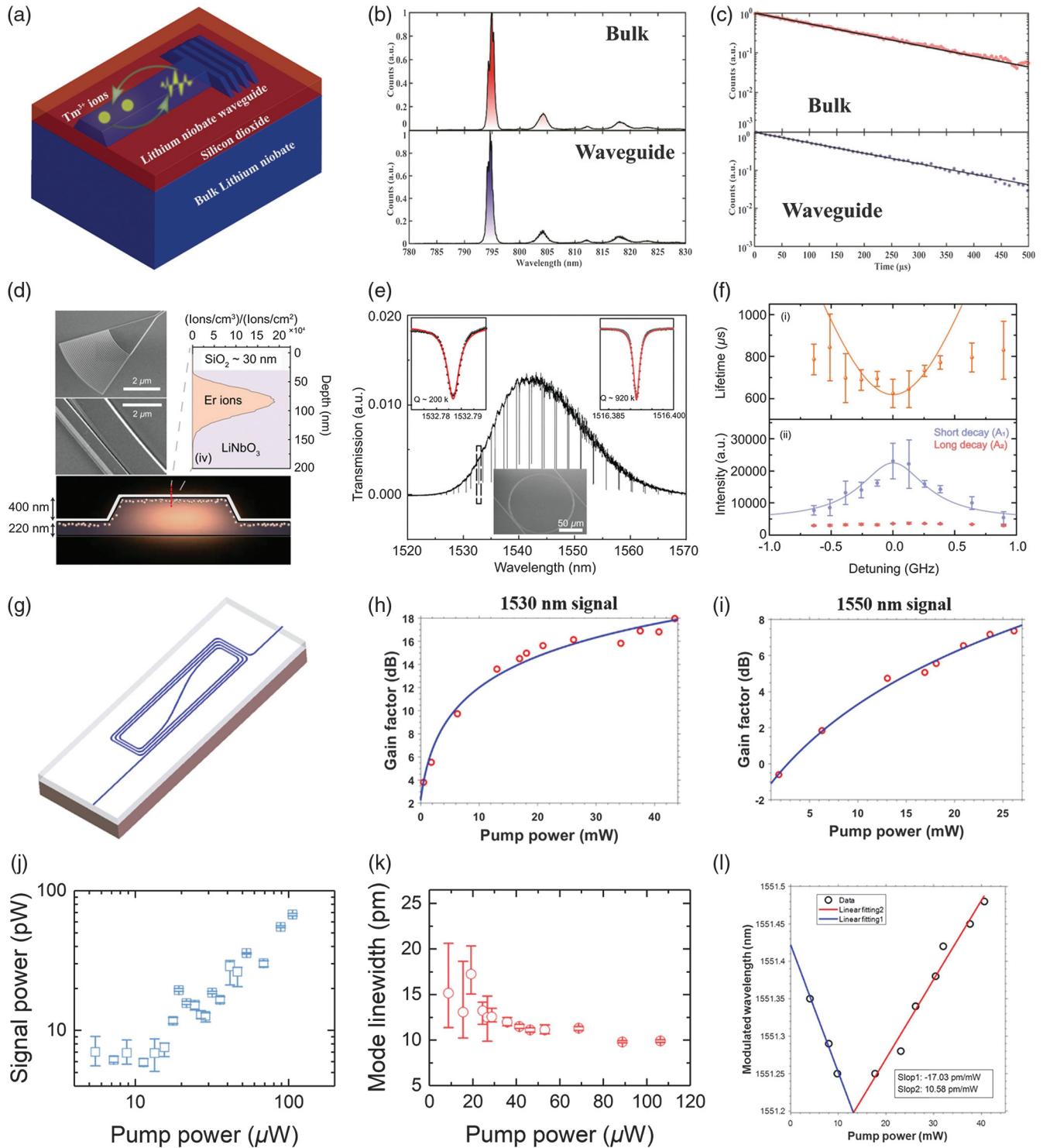


**Fig. 21** Rare-earth-doped devices in LN. (a) Schematic structure of a  $\text{Tm}^{3+}$  doped TFLN device. Measured (b) photoluminescence spectra and (c) time-resolved photoluminescence in  $\text{Tm}^{3+}$  doped bulk LN and TFLN, respectively. (a)–(c) Adapted with permission from Ref. 94 © 2019 ACS. (d) Top left: SEM images of GC and microring patterned in TFLN. Top right: the stopping and range of ions in matter (SRIM) simulation of  $\text{Er}^{3+}$  implantation depth distribution. Bottom: schematic electrical field distribution. (e) Transmission spectrum of a TFLN microring. (f) Measured fluorescence decay when the pumping frequency is detuned from the ring resonance. (d)–(f) Adapted from Ref. 95. (g) Schematic structure of an  $\text{Er}^{3+}$  doped TFLN waveguide-based amplifier. Gain characterization with respect to different pump power when signal wavelength is (h) 1530 nm and (i) 1550 nm. (g)–(i) Adapted with permission from Ref. 33 © 2021

**Fig. 21** (Continued) Wiley-VCH GmbH. (j) Signal power and (k) mode linewidth with respect to different pump powers. (j) and (k) Adapted with permission from Ref. 330 © 2021 OSA. (l) Modulated wavelength of microdisk laser with respect to pump power. Adapted with permission from Ref. 93 © 2021 OSA.

measured a  $\sim -17.03$  pm/mW tuning efficiency with a pump power below 13 mW, and 10.58 pm/mW with a pump power above 13 mW,<sup>93</sup> as shown in Fig. 21(l). Another example of a monolithically integrated electrical tunable microring laser is based on the EO effect of LN with estimated EO coefficient of around 0.33 pm/V.<sup>334</sup> It is worth noting that there is also a heterogeneously integrated III-V laser recently demonstrated on TFLN based on transfer printing.<sup>335</sup> Benefiting from a mature design in III-V semiconductors generally, its performance is better than that of rare earth doped devices. However, the reduced fabrication complexity and monolithic integration features make rare earth doped device a promising alternative.

In summary, rare earth doping of LN is an interesting topic for both research and industrial applications. Combined with other effects (demonstrated in Sec. 2) of LN, more chip scale PIC functionality can be realized.

#### 4.6 Other Devices

In addition to the above major device categories, LN is also used for other applications as well. With the rapid development of TFLN, some devices that have been conventionally hard to realize in bulk LN, such as metasurface structures, can be realized in TFLN with greater ease. Therefore, we will introduce the latest results demonstrated in TFLN in this section.

##### 4.6.1 Pyroelectric devices

As discussed in Sec. 2, LN has a strong pyroelectric coefficient, which is suitable for the fabrication of a pyroelectric PD.<sup>48,336</sup> As the pyroelectric current is inversely proportional to the dielectric thickness,<sup>337</sup> a thinner LN thickness is preferred in such devices.<sup>338</sup> However, in the typical bulk LN platform, it is challenging to reduce the LN thickness down to several micrometers,<sup>339</sup> whereas this will be quite easy when transferring this technology to the TFLN platform. For example, Chauvet et al. demonstrated improved pyroelectric effect-based beam self-trapping in an 8- $\mu$ m-thick LN thin film made using the lapping and polishing method.<sup>338</sup> The recently developed thinner LN film using CIS technology enables the reliability of some more functional pyroelectric devices. As shown in Fig. 22, Suen et al. demonstrated a type of metamaterial absorber-based pyroelectric detector in TFLN, which works over a wide wavelength range from 8 to 11  $\mu$ m.<sup>18</sup> The metamaterial structure contributes a high field concentration and thus has a better performance. Such an advantage can be clearly seen from the measured results shown in Fig. 22(d), where pyroelectric PD without the metamaterial pattern has no response, while with a metamaterial pattern it shows a strong response peak. Through appropriate design of the metamaterial absorber, the working wavelength of the pyroelectric detector could be tuned. More recently, Guan et al. combined the pyroelectric effect of X-cut LN with graphene and realized a broadband (405 to 2000 nm) and high detectivity ( $\sim 8.65 \times 10^{14}$  Jones) graphene PD.<sup>336</sup> Compared with other pyroelectric material platforms, the high pyroelectric

coefficient feature of LN will continually get attention, especially for some applications such as gas sensing.

##### 4.6.2 Nonlinear metasurface devices

Another research topic in LN photonics is the nonlinear metasurface devices.<sup>340–343</sup> As discussed in Secs. 2.3 and 4.3, LN has large second- and third-order nonlinear coefficients and therefore has been used for various nonlinear functionalities with both bulk LN<sup>12,13,67,69,80</sup> and TFLN waveguide devices.<sup>55,56,59,61</sup> Metasurfaces, consisting of subwavelength elements, can manipulate light–matter interaction with compact forms. Very recently, metasurfaces also provide another pathway for nonlinear devices.<sup>344–346</sup> Due to the recent developments in high-quality TFLN and patterning technology, nonlinear optical conversions have seen enhancement effects with resonator metasurface structures, and they also enrich the research of meta-optics in general. Figures 23(a) and 23(b) illustrate the schematic and experimental results of a metasurface made of TFLN for enhanced SHG.<sup>341</sup> Such a device exhibits Mie-type resonance at a 1550 nm wavelength. According to the measured SHG shown in Fig. 23(b), its CE is round  $10^{-6}$  for 0.88 mW average input power (3.3 kW peak power/4.3 GW/cm<sup>2</sup> peak intensity). As described in Sec. 2, LN has a wide transparency window, ranging from visible to mid-infrared, so that Carletti et al. were able to demonstrate nonlinear meta-optics in the visible range using a TFLN metasurface.<sup>342</sup> The diffraction mechanism of such a

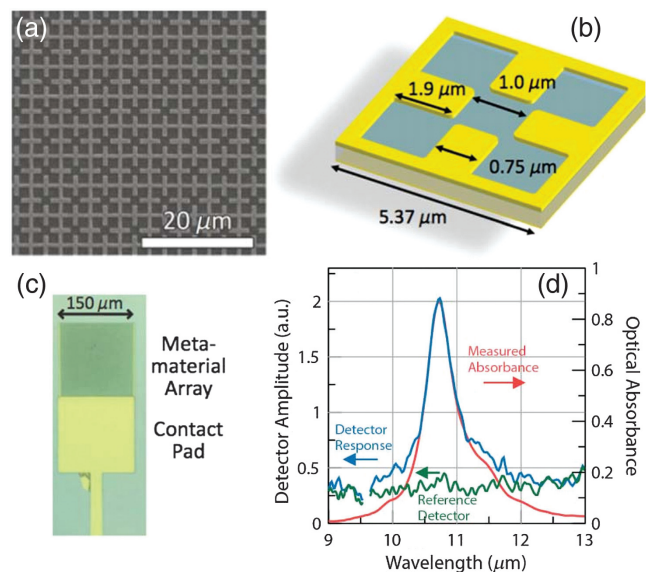


**Fig. 22** TFLN-based pyroelectric infrared detector. (a) SEM image of the metamaterial top surface. (b) Schematic of the unit cell. (c) Microscopic image of the pyroelectric PD. (d) Measured detector response and optical absorption of pyroelectric PD with and without metamaterial structure. (a)–(d) Adapted with permission from Ref. 18 © 2017 OSA.

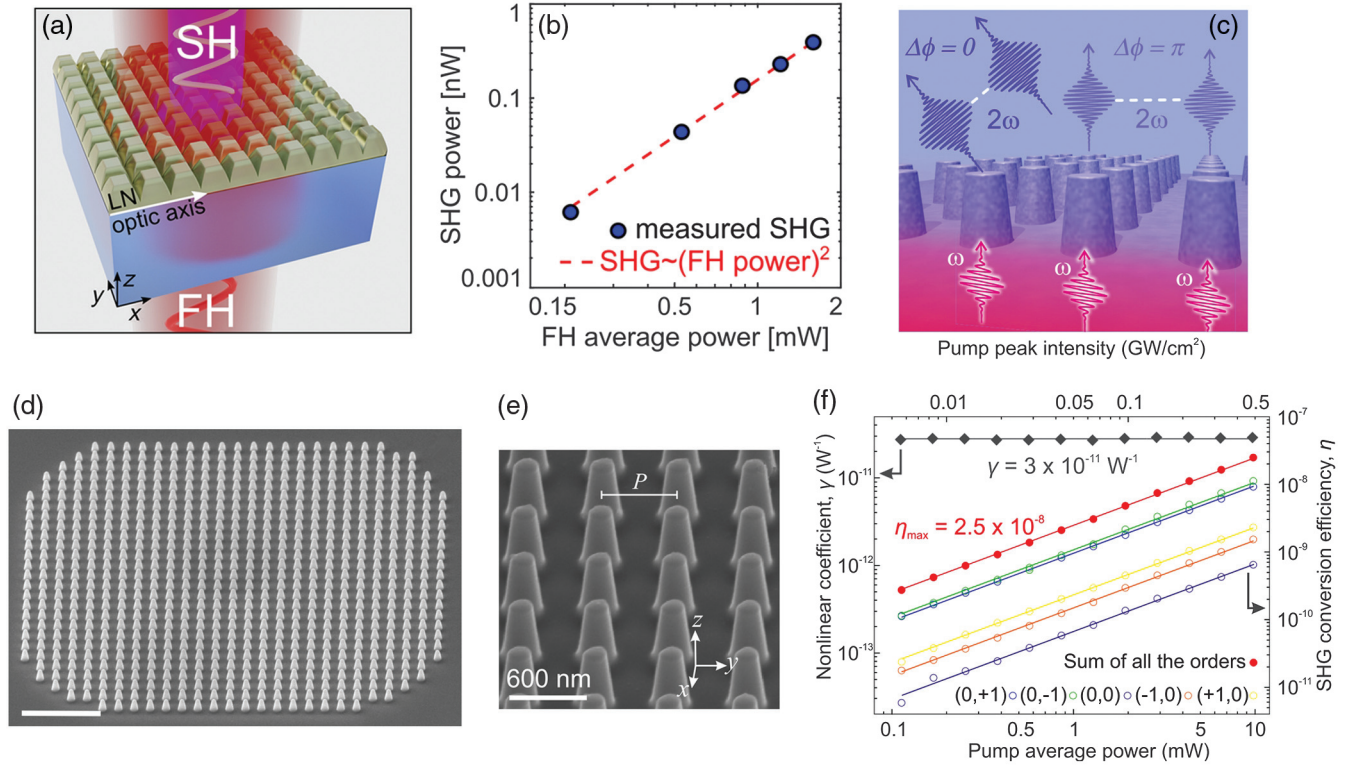


**Fig. 23** Nonlinear metasurface devices in LN. (a) Schematic structure of TFLN metasurface for SHG. (b) Measured SHG power with respect to fundamental harmonic average power. (a) and (b) Adapted with permission from Ref. 341 © 2020 ACS. (c) Schematic structure of the diffraction mechanism in the metasurface. SEM images of the (d) full view metasurface (scale bar is 3  $\mu\text{m}$ ) and (e) zoom in nanopillars. (f) SHG CE of the diffraction orders with respect to pump power. (c)–(f) Adapted with permission from Ref. 342.

metasurface structure is shown in Fig. 23(c). Their device is fabricated by ion beam milling, which enables high aspect-ratio structures as well as very fine feature sizes. SEM images of their fabricated device are shown in Figs. 23(d) and 23(e). According to the measured results shown in Fig. 23(f), the SHG CE is about  $2.4 \times 10^{-8}$  at a pump intensity as low as 0.5  $\text{GW}/\text{cm}^2$ . Hence, more results combining the advantages of LN and metasurface design can be expected in the future.

#### 4.6.3 Visible photonics devices

Most of the reported LN-based devices so far are operating in the near-infrared regime, especially for EO devices. This is mainly due to the fact that it matches the current telecom/datacom wavelength range. Compared with other material platforms, such as Si and InP, the transparency window of LN is broad (400 nm to 5  $\mu\text{m}$ ) and notably covers the entire visible wavelength range. Therefore, LN is an attractive material platform for visible photonics, which is of great interest for applications ranging from consumer electronics, quantum optics, metrology, to biosensing and biomedicine. Recently, Desiatov et al. have demonstrated both passive and active blocks operated at visible wavelengths based on the TFLN platform.<sup>42</sup> Figures 24(a)–24(c) show an example of their demonstrated TFLN EO modulator operating at visible wavelength range. According to the measured results, the  $V_\pi$  is 8 V for a 2-mm long device (corresponding to  $V_\pi L$  of 1.6  $\text{V} \cdot \text{cm}$ ), and its

3-dB EO bandwidth is around 10 GHz. The researchers attribute the lower bandwidth to limitations in the measurement setup. Although the currently reported device performance in the visible range is still not as good as that in the near-infrared range, we believe it can be improved by design and process optimization. Integrated LN-based visible photonics devices will become an area of significant interest in the foreseeable future.

#### 4.6.4 Superconducting nanowire single-photon detector

As discussed in Sec. 4.3, the rich nonlinear effects in LN in combination with its EO property make it an attractive platform for quantum applications. Integrating an efficient single photon detector in LN will broaden such application scenarios in the quantum area. Recently, superconducting nanowire-based SPDs (SNSPDs) have been successfully integrated on Ti diffused LN<sup>347</sup> and TFLN platforms.<sup>172,348,349</sup> Figures 25(a)–25(c) show an example of integrated amorphous tungsten silicide SNSPD on Ti in-diffused LN waveguide, which validates the possibility of evanescent coupled SNSPD in LN. In TFLN, both niobium nitride (NbN)<sup>172,348</sup> and niobium titanium nitride (NbTiN)<sup>349</sup> have been deposited onto LN passive circuits. Figure 25(d) shows an example of a waveguide integrated SNSPD on TFLN, which consists of a 1D GC, a TFLN waveguide, and a U-shaped NbN SNSPD.<sup>172</sup> Its measured on-chip detection efficiency (OCDE), dark count rate (DCR), and noise equivalent power (NEP) are shown in Figs. 25(e) and 25(f). When biased at a 95% switching

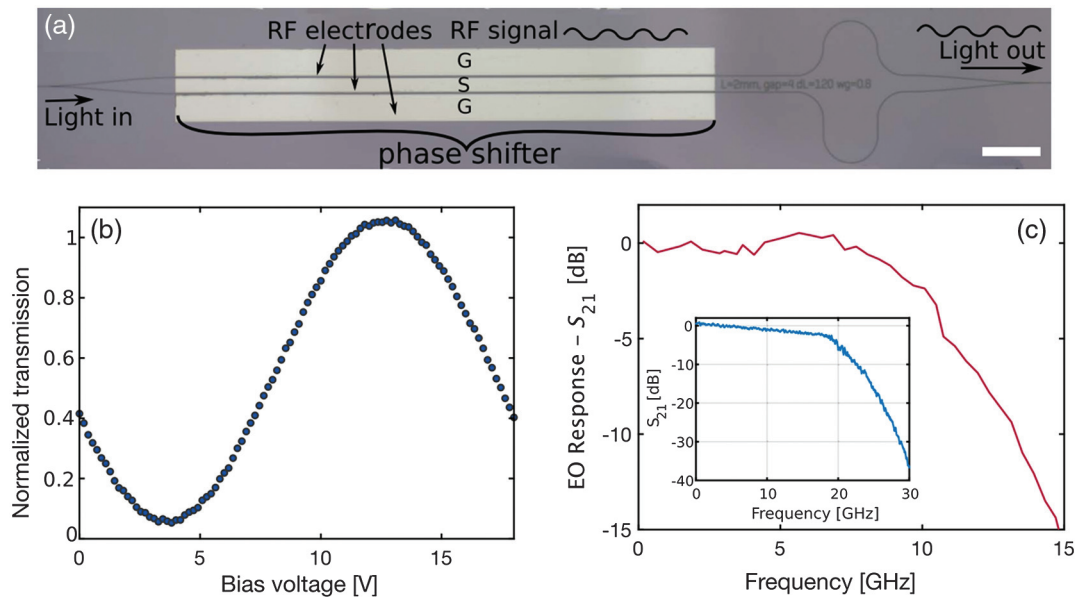


**Fig. 24** TFLN modulator operated at visible wavelength range. (a) Microscopic image of the TFLN EO modulator. (b) Measured transmission spectrum and (c)  $S_{21}$  curve. (a)–(c) Adapted with permission from Ref. 42 © 2019 OSA.

current of the nanowire ( $I_{SW}$ ), the DCR is measured to be around 13 Hz with 46% OCDE. While at 95%  $I_{SW}$  (switching current), the NEP is measured to be  $1.42 \times 10^{-18}$  W/ $\sqrt{\text{Hz}}$ . All these measured results are close to other kinds of waveguide-integrated SNSPDs.<sup>350</sup> Another example realized a more functional PIC,<sup>349</sup> as shown in Fig. 25(g), which integrated an EO MZI modulator (MZM) together with two waveguide SNSPDs. Here, the researchers use U-shaped NbTiN nanowires as the detection material. The measured OCDEs for the two SNSPDs are 24% and 27%, respectively, under a critical current of 14 and 12.5  $\mu\text{A}$ . Such a performance is worse than that of an NbN SNSPD mainly due to the process technology, although NbTiN has a lower kinetic inductance compared with NbN.<sup>349</sup> The researchers also characterized the PIC performance (simultaneous operation of EO modulator and SNSPDs). Figure 25(h) shows the count rate traces from two SNSPDs placed at the two output ports of the MZM while MZM is driven with a 1-kHz sawtooth wave. A small reduction of the EO coefficient of the TFLN waveguide at cryogenic temperatures is observed, which is consistent with what has been observed in bulk LN modulators.<sup>351,352</sup> High-performance SNSPD is an essential building block for constructing a fully chip-scale integrated quantum photonic circuit. Current reports with limited performance provide a direction and show the emerging trend for integrated SNSPDs on both bulk LN and TFLN platforms.

#### 4.6.5 Heterogeneously integrated photodetector

Compared with bulk LN devices, the TFLN platform not only can realize better device performance but also enables the integration of different photonic components together on the same chip to realize versatile functional PIC. There are already many examples that have been demonstrated, such as a Kerr comb generation and filtering PIC demonstrated by Wang et al.<sup>76</sup> Although LN by itself cannot realize detection, an on-chip detector is possible by integrating another material on it.<sup>34,172,349</sup>

As discussed in Sec. 4.6.4, NbN and NbTiN can be deposited onto TFLN to form SNSPDs for quantum applications, while for telecommunication-related applications operated in the near-infrared or visible wavelength window, one possible solution is by HI of Si, germanium or III–V absorber layers.<sup>22,34,270,353,354</sup> Figures 26(a) and 26(b) show an example of the integration of a Si metal–semiconductor–metal PD with LN passive devices, with a measured 37-mA/W responsivity at 850 nm wavelength.<sup>34</sup> In Sec. 4.5, we discussed chip scale amplifier and laser emitter based on rare earth doped TFLN devices. Therefore, all the functions, including light emission, modulation, signal processing, transmission, and detection, can be integrated on the same TFLN chip, which paves the way for large-scale PIC in TFLN.

#### 4.6.6 Wafer scale fabricated devices

Most of currently reported LN photonics devices (both bulk LN and TFLN) are fabricated in the laboratory (Lab). With the rapid development of integrated LN photonics, wafer scale fabrication/production (from Lab to Fab) is already on the agenda. There are already some pioneering works based on TFLN/LNOI, which is very similar to typical SOI. Luke et al. demonstrated a measured propagation loss as low as 0.27 dB/cm using wafer-scale deep ultraviolet lithography.<sup>355</sup> Safian et al. demonstrated a platform for fabricating TFLN devices bonded on top of silicon photonics chips—a method that has a good compatibility with silicon foundry.<sup>356</sup> Both works pave the way for large-scale production of integrated LN devices in foundry mode. As most of the process flows of TFLN devices are compatible with CMOS (can be fabricated using CMOS line equipment), the biggest challenge is the TFLN wafer size. In current CMOS lines, most advanced machines can only handle 8/12-inch wafers for low-cost mass production. We believe high quality and large size TFLN wafers will be available in the near future with technology development. From there, TFLN devices fabricated in foundry mode can be expected.

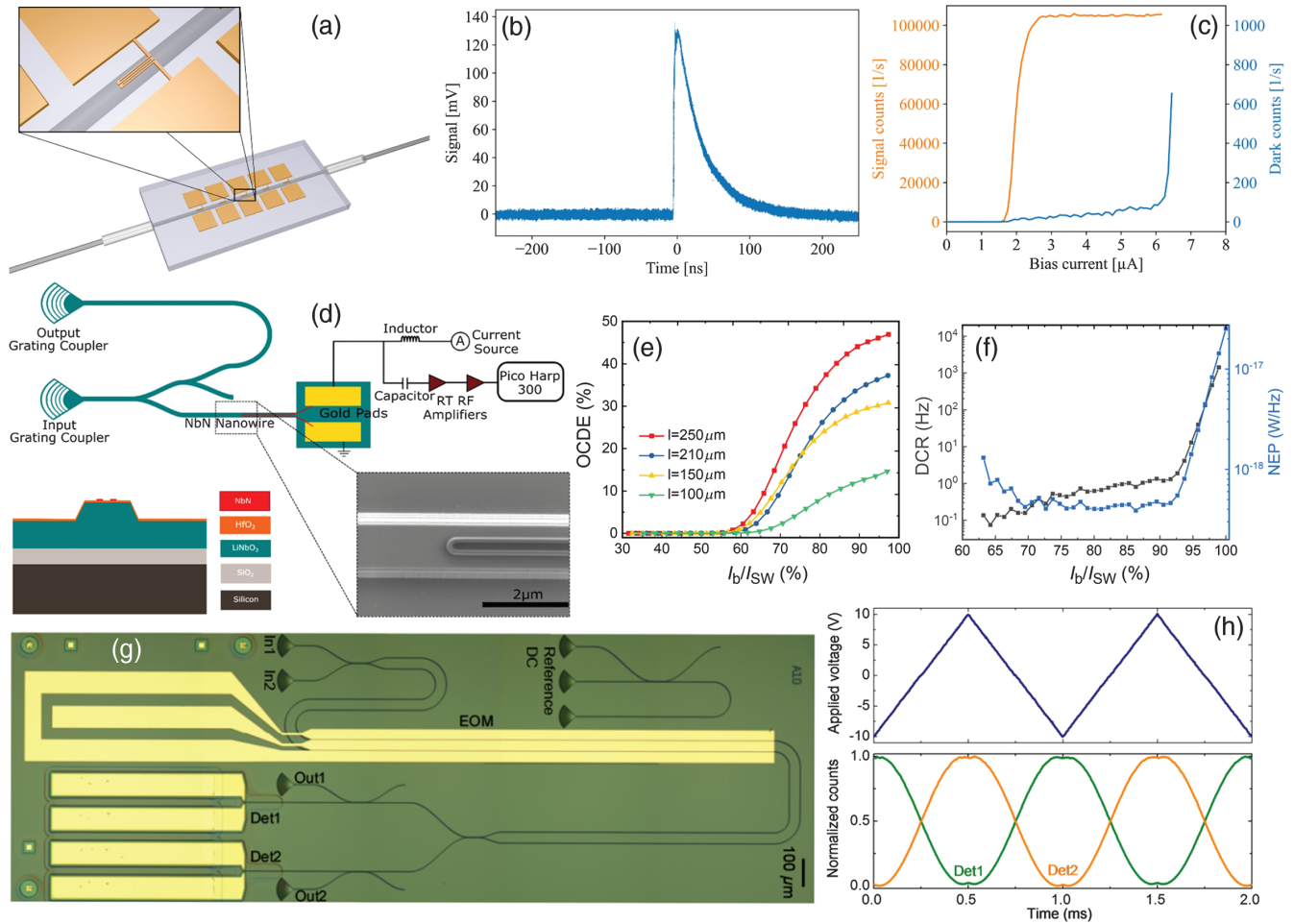


**Fig. 25** Integrated SNSPD in LN. (a) Schematic structure of Ti diffused LN waveguide integrated with five in-line SNSPDs. Inset shows the detail of single SNSPD, which has 400  $\mu\text{m}$  length and 160 nm width. (b) Measured response time of an integrated SNSPD. (c) Measured signal and dark counts of the integrated SNSPD under different bias current. (a)–(c) Adapted with permission from Ref. 347. Published by IOP Publishing Ltd. (d) Top: schematic of a TFLN GC coupling light into an integrated U-shaped NbN SNSPD. Bottom left: device cross section. Bottom right: SEM image of the device detail. (e) Measured OCDE, (f) DCR and NEP with respect to  $I_b/I_{SW}$  for a 250- $\mu\text{m}$  long detector.  $I_{SW}$ , switching current;  $I_b$ , bias current. (d)–(f) Adapted from Ref. 172. (g) Microscopic image of the on-chip integrated circuit containing one TFLN EO modulator and two NbTiN SNSPDs. (h) Measured count rates collected from the SNSPDs with a time tagging module (bottom) when EO modulator is driven with a ramp function with an amplitude of 20  $V_{pp}$  and frequency of 1 kHz (top). (g) and (h) Adapted with permission from Ref. 349.

## 5 Summary and Outlook

We have given a comprehensive review of advances in LN photonics, involving material properties, key processing technologies, and functional devices based on both bulk LN and TFLN. Compared with Si, LN has a large EO coefficient, which is its most significant feature and advantage. In addition, the presence of large second- and third-order nonlinear coefficients of LN also makes it a suitable platform for various nonlinear applications. LN can also be used for fabrication of AO devices due to its large AO coefficient. With the development of TFLN, integrated AO devices with enhanced performance make it more attractive. Rare earth doped LN can provide integrated solutions for optical amplification and laser emission. Some other properties of LN were also discussed along with their

corresponding fabricated devices. All of them prove that LN is an excellent platform for photonics applications. With the rapid development of large wafer sizes and high-quality TFLN, more compact and integrable devices are preferred. LN photonics has experienced great development during the past decades, especially when TFLN recently became commercially available. We have tried to cover different aspects of LN-related researches in this review. However, some of the work in the literature will probably not be included in this paper for many reasons, such as publication date after we prepare this paper. We believe these excellent noncited results are also based on the basic properties discussed in Sec. 2.

Looking forward to the development of LN photonics, there are several key directions that can be considered.

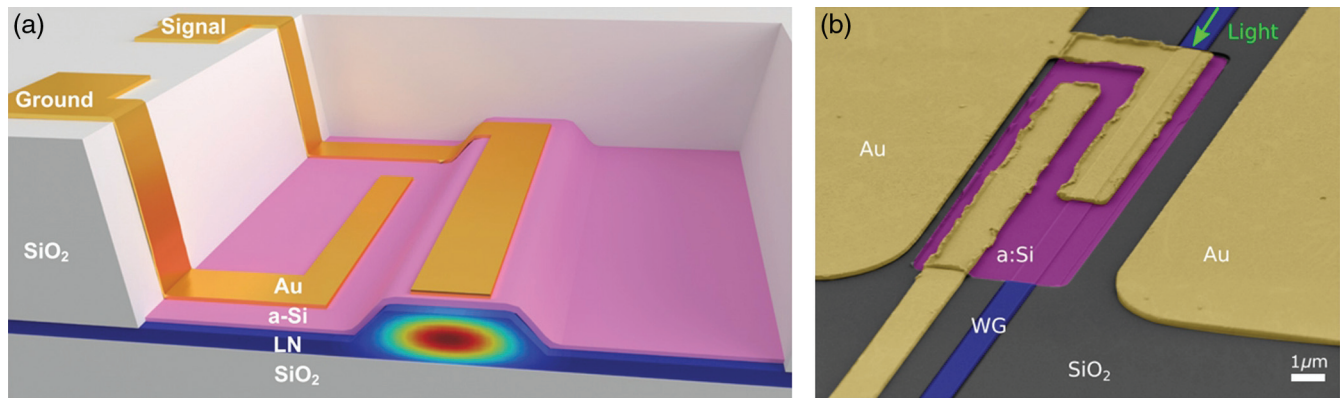


**Fig. 26** Integrated Si PD onto LN passive circuit. (a) Schematic structure and (b) false colored SEM image of a TFLN waveguide with integrated Si PD. (a) and (b) Adapted from Ref. 34.

### 5.1 Integrated LN Photonics

Integrated TFLN photonics will still be one of the best supplements to bulk LN devices due to the large refractive index contrast available. With the high quality of commercially available TFLN, functional blocks with an increasingly greater capability will be demonstrated using a similar design methodology to that of existing material platforms, such as silicon photonics. Such a trend is ongoing and will continue in the foreseeable future as evidenced by the various kinds of passive and active blocks demonstrated in Sec. 4.1. New design methods or structures demonstrated in other material platforms can be transferred into the integrated LN platform, such as inverse design<sup>357,358</sup> and deep learning.<sup>359</sup>

With high performance device-level demonstration, integrating different functional blocks (relying on multiple properties) on the same chip to realize a truly chip-scale PIC system will be another interesting trend. There are already some good attempts, and a part of them have been discussed in Sec. 4.<sup>34,76</sup> We believe denser PIC will be demonstrated in the future and some integration methods can be adopted from other material systems. For example, heterogeneous integration of III–V semiconductors with TFLN is still seldom explored so far and will be an interesting area in the future.

It is worth mentioning that TFLN devices will not completely replace bulk LN devices, as bulk LN devices have certain noteworthy advantages. For example, there is still a gap between bulk LN- and TFLN-based EO devices for CE, as discussed in Sec. 4.2.2. Bulk LN is also regarded as an integrated platform even though its integration density is low.<sup>352</sup> Therefore, we believe both the bulk and TFLN will exist together and complement each other to make integrated LN photonics more attractive in research and applicable in industry.

### 5.2 High Performance Electro-Optic Devices

One of the most unique features of LN is its large EO coefficient, which makes it a good material of choice for an EO modulator. Although numerous LN-based EO modulators have been demonstrated during the past year, there is still plenty of room for improvements in the reported device performance. For example, even though TFLN modulators with speeds up to 100 Gb/s NRZ have been demonstrated,<sup>31</sup> the speed can be

further improved either by shortening the MZI arm length or using more advanced modulation schemes.<sup>88,360</sup> In addition, as shown in the discussion of Sec. 4.2.1, there are many performance metrics to characterize a modulator. It is usually difficult to achieve all the best metrics at the same time. There is a lot of work that can be done to optimize the overall performance or enhance one specific metric to adapt these devices to different application scenarios. It is also worth mentioning that the strong EO effect of LN can not only be used for realizing high performance modulators but it can also be used for other areas where EO modulation shows advantages, such as the EO frequency comb.<sup>77</sup> Some more examples can be found in Sec. 4.2.

### 5.3 Nonlinear and Quantum Photonics

Based on high second- and third-order nonlinear effects inside LN, various nonlinear applications have been demonstrated in both bulk LN and TFLN. Compared with bulk LN, stronger mode confinement inside TFLN, better interaction between light and the LN medium is achieved, thus enabling a greater nonlinear converting efficiency. Challenges remain on how to further improve the nonlinear CE. Possible solutions include optimizing the phase-matching condition by either new designs or processes,<sup>54</sup> waveguide dispersion engineering,<sup>79</sup> and using optical field enhancement structures such as metasurfaces.<sup>55</sup>

LN can also play a significant role in quantum photonics (quantum communication, computing, etc.) based on its nonlinear effects. For a long time, bulk LN has been used for quantum application demonstrations.<sup>15,361</sup> The emerging TFLN makes more compact devices reality. We have discussed certain heterogeneously integrated high-performance SNSPDs in TFLN.<sup>172,349</sup> At the current stage, the challenges are with how to implement new concepts and ideas based on LN platforms with better performance, especially for TFLN. Some related results have already been demonstrated recently.<sup>81,82</sup> We believe chip-scale fully integrated quantum circuits can be expected in the near future.

### 5.4 Acousto-Optic Devices

LN is also a good material platform for AO devices due to its significant photoelastic effect, which can be used in microwave photonics and quantum information processing. In the typical

bulk LN device, the performance of AO devices has been mainly restricted due to its weak light confinement. The newly developed TFLN compensates for such a drawback. Looking forward to the further development, ultrahigh  $Q$  factor optomechanics microcavities and highly efficient AO modulators/frequency shifters based on TFLN should be able to attract more interest and attention.

### 5.5 Rare Earth Doped Devices

Rare earth doped devices have not received enough attention, although there is a potential for integrated amplifiers/lasers, and some results have been demonstrated recently.<sup>33,330,331</sup> Compared with heterogeneously integrated III-V amplifiers/lasers, there are still some gaps to be closed in the development of rare earth doped LN devices. This issue can be addressed by optimizing the fabrication process or device designs.<sup>33,92,330,331</sup>

### 5.6 Wafer Scale Fabrication

With the development of LN photonics, wafer-scale fabrication of LN devices using foundry pilot will receive much more attention, especially for industrial applications. Meanwhile, there will undoubtedly be some technology challenges that must be overcome. Currently, there are already some attempts in such areas as discussed in Sec. 4.6.6, and there will be more effort devoted in the near future. It is believed that with more mature process technologies and advanced theory, LN photonics will be further developed in the near future.

### Acknowledgments

This work was supported by the National Research Foundation, Singapore, under its Competitive Research Programme (CRP Award No. NRF-CRP24-2020-0003). This work was also supported by the program for HUST Academic Frontier Youth Team (2018QYTD08). This work was partially supported by A\*STAR (Agency for Science, Technology and Research), Singapore, under the RIE2020 Advanced Manufacturing and Engineering (AME) IAF-PP Grant, No. A19B3a0008. The authors thank Dr. Di Zhu for useful discussions. The authors declare no conflicts of interest.

### References

1. B. Matthias and J. Remeika, "Ferroelectricity in the ilmenite structure," *Phys. Rev.* **76**(12), 1886–1887 (1949).
2. R. Weis and T. Gaylord, "Lithium niobate: summary of physical properties and crystal structure," *Appl. Phys. A* **37**(4), 191–203 (1985).
3. E. L. Wooten et al., "A review of lithium niobate modulators for fiber-optic communications systems," *IEEE J. Sel. Top. Quantum Electron.* **6**(1), 69–82 (2000).
4. L. Arizmendi, "Photonic applications of lithium niobate crystals," *Phys. Stat. Solidi A* **201**(2), 253–283 (2004).
5. D. Janner et al., "Micro-structured integrated electro-optic LiNbO<sub>3</sub> modulators," *Laser Photonics Rev.* **3**(3), 301–313 (2009).
6. G. Poberaj et al., "Lithium niobate on insulator (LNOI) for micro-photonic devices," *Laser Photonics Rev.* **6**(4), 488–503 (2012).
7. A. Boes et al., "Status and potential of lithium niobate on insulator (LNOI) for photonic integrated circuits," *Laser Photonics Rev.* **12**(4), 1700256 (2018).
8. A. Honardoost, K. Abdelsalam, and S. Fathpour, "Rejuvenating a versatile photonic material: thin-film lithium niobate," *Laser Photonics Rev.* **14**(9), 2000088 (2020).
9. Y. Jia, L. Wang, and F. Chen, "Ion-cut lithium niobate on insulator technology: recent advances and perspectives," *Appl. Phys. Rev.* **8**(1), 011307 (2021).
10. G. T. Reed et al., "Silicon optical modulators," *Nat. Photonics* **4**(8), 518–526 (2010).
11. M. Smit et al., "An introduction to InP-based generic integration technology," *Semicond. Sci. Technol.* **29**(8), 083001 (2014).
12. M. Yamada et al., "First-order quasi-phase matched LiNbO<sub>3</sub> waveguide periodically poled by applying an external field for efficient blue second-harmonic generation," *Appl. Phys. Lett.* **62**(5), 435–436 (1993).
13. K. Mizuuchi, K. Yamamoto, and M. Kato, "Harmonic blue light generation in bulk periodically poled MgO:LiNbO<sub>3</sub>," *Electron. Lett.* **32**(22), 2091–2092 (1996).
14. K. R. Parameswaran et al., "Highly efficient second-harmonic generation in buried waveguides formed by annealed and reverse proton exchange in periodically poled lithium niobate," *Opt. Lett.* **27**(3), 179–181 (2002).
15. S. Saravi, T. Pertsch, and F. Setzpfandt, "Lithium niobate on insulator: an emerging platform for integrated quantum photonics," *Adv. Opt. Mater.* **9**(22), 2100789 (2021).
16. L. Cai et al., "Acousto-optical modulation of thin film lithium niobate waveguide devices," *Photonics Res.* **7**(9), 1003–1013 (2019).
17. L. Shao et al., "Microwave-to-optical conversion using lithium niobate thin-film acoustic resonators," *Optica* **6**(12), 1498–1505 (2019).
18. J. Y. Suen et al., "Multifunctional metamaterial pyroelectric infrared detectors," *Optica* **4**(2), 276–279 (2017).
19. R. Schmidt and I. Kaminow, "Metal-diffused optical waveguides in LiNbO<sub>3</sub>," *Appl. Phys. Lett.* **25**(8), 458–460 (1974).
20. J. Jackel and C. Rice, "Topotactic LiNbO<sub>3</sub> to cubic perovskite structural transformation in LiNbO<sub>3</sub> and LiTaO<sub>3</sub>," *Ferroelectrics* **38**(1), 801–804 (1981).
21. J. L. Jackel, C. Rice, and J. Veselka, "Proton exchange for high-index waveguides in LiNbO<sub>3</sub>," *Appl. Phys. Lett.* **41**(7), 607–608 (1982).
22. G. Chen et al., "High speed and high power polarization insensitive germanium photodetector with lumped structure," *Opt. Express* **24**(9), 10030–10039 (2016).
23. G. Chen et al., "Switchable in-line monitor for multi-dimensional multiplexed photonic integrated circuit," *Opt. Express* **24**(13), 14841–14850 (2016).
24. G. Chen, Y. Yu, and X. Zhang, "Monolithically mode division multiplexing photonic integrated circuit for large-capacity optical interconnection," *Opt. Lett.* **41**(15), 3543–3546 (2016).
25. M. Ye et al., "On-chip WDM mode-division multiplexing interconnection with optional demodulation function," *Opt. Express* **23**(25), 32130–32138 (2015).
26. D. Zhou et al., "Germanium photodetector with distributed absorption regions," *Opt. Express* **28**(14), 19797–19807 (2020).
27. Y. Yu et al., "Intra-chip optical interconnection based on polarization division multiplexing photonic integrated circuit," *Opt. Express* **25**(23), 28330–28336 (2017).
28. G. Chen, Y. Yu, and X. Zhang, "Optical phase erasure and wavelength conversion using silicon nonlinear waveguide with reverse biased PIN junctions," *IEEE Photonics J.* **7**(5), 7102808 (2015).
29. S. Kurimura et al., "Quasi-phase-matched adhered ridge waveguide in LiNbO<sub>3</sub>," *Appl. Phys. Lett.* **89**(19), 191123 (2006).
30. T. Umeki, O. Tadanaga, and M. Asobe, "Highly efficient wavelength converter using direct-bonded PPZnLN ridge waveguide," *IEEE J. Quantum Electron.* **46**(8), 1206–1213 (2010).
31. C. Wang et al., "Integrated lithium niobate electro-optic modulators operating at CMOS-compatible voltages," *Nature* **562**(7725), 101–104 (2018).

32. P. De Nicola et al., "Fabrication of smooth ridge optical waveguides in LiNbO<sub>3</sub> by ion implantation-assisted wet etching," *J. Lightwave Technol.* **31**(9), 1482–1487 (2013).
33. J. Zhou et al., "On-chip integrated waveguide amplifiers on erbium-doped thin-film lithium niobate on insulator," *Laser Photonics Rev.* **15**(8), 2100030 (2021).
34. B. Desiatov and M. Lončar, "Silicon photodetector for integrated lithium niobate photonics," *Appl. Phys. Lett.* **115**(12), 121108 (2019).
35. Z. Yu et al., "High-dimensional communication on etchless lithium niobate platform with photonic bound states in the continuum," *Nat. Commun.* **11**, 2602 (2020).
36. K. Nassau, H. Levinstein, and G. Loiacono, "Ferroelectric lithium niobate. 1. Growth, domain structure, dislocations and etching," *J. Phys. Chem. Solids* **27**(6-7), 983–988 (1966).
37. K. Nassau, H. Levinstein, and G. Loiacono, "Ferroelectric lithium niobate. 2. Preparation of single domain crystals," *J. Phys. Chem. Solids* **27**(6-7), 989–996 (1966).
38. S. Abrahams, J. M. Reddy, and J. Bernstein, "Ferroelectric lithium niobate. 3. Single crystal X-ray diffraction study at 24°C," *J. Phys. Chem. Solids* **27**(6-7), 997–1012 (1966).
39. S. Abrahams, W. C. Hamilton, and J. Reddy, "Ferroelectric lithium niobate. 4. Single crystal neutron diffraction study at 24°C," *J. Phys. Chem. Solids* **27**(6-7), 1013–1018 (1966).
40. S. Abrahams, H. Levinstein, and J. Reddy, "Ferroelectric lithium niobate. 5. Polycrystal X-ray diffraction study between 24° and 1200°C," *J. Phys. Chem. Solids* **27**(6-7), 1019–1026 (1966).
41. R. W. Boyd, "The electrooptic and photorefractive effects," in *Nonlinear Optics*, pp. 511–541, 3rd ed., Academic Press, Elsevier, Inc. (2008).
42. B. Desiatov et al., "Ultra-low-loss integrated visible photonics using thin-film lithium niobate," *Optica* **6**(3), 380–384 (2019).
43. T.-J. Wang, C.-H. Chu, and C.-Y. Lin, "Electro-optically tunable microring resonators on lithium niobate," *Opt. Lett.* **32**(19), 2777–2779 (2007).
44. J. Mishra et al., "Mid-infrared nonlinear optics in thin-film lithium niobate on sapphire," *Optica* **8**(6), 921–924 (2021).
45. C. Thierfelder et al., "Do we know the band gap of lithium niobate?" *Phys. Stat. Solidi C* **7**(2), 362–365 (2010).
46. V. G. Dmitriev, G. G. Gurzadyan, and D. N. Nikogosyan, *Handbook of Nonlinear Optical Crystals*, Vol. **64**, Springer (2013).
47. M. Bache and R. Schiek, "Review of measurements of Kerr nonlinearities in lithium niobate: the role of the delayed Raman response," arXiv:1211.1721 (2012).
48. A. Savage, "Pyroelectricity and spontaneous polarization in LiNbO<sub>3</sub>," *J. Appl. Phys.* **37**(8), 3071–3072 (1966).
49. S. Yao et al., "Growth, optical and thermal properties of near-stoichiometric LiNbO<sub>3</sub> single crystal," *J. Alloys Compd.* **455**(1-2), 501–505 (2008).
50. L. Moretti et al., "Temperature dependence of the thermo-optic coefficient of lithium niobate, from 300 to 515 K in the visible and infrared regions," *J. Appl. Phys.* **98**(3), 036101 (2005).
51. A. W. Warner, M. Onoe, and G. A. Coquin, "Determination of elastic and piezoelectric constants for crystals in class (3m)," *J. Acoust. Soc. Am.* **42**(6), 1223–1231 (1967).
52. M. He et al., "High-performance hybrid silicon and lithium niobate Mach-Zehnder modulators for 100 Gbit s<sup>-1</sup> and beyond," *Nat. Photonics* **13**(5), 359–364 (2019).
53. L. Gui et al., "Local periodic poling of ridges and ridge waveguides on X- and Y-cut LiNbO<sub>3</sub> and its application for second harmonic generation," *Opt. Express* **17**(5), 3923–3928 (2009).
54. L. Chang et al., "Thin film wavelength converters for photonic integrated circuits," *Optica* **3**(5), 531–535 (2016).
55. C. Wang et al., "Metasurface-assisted phase-matching-free second harmonic generation in lithium niobate waveguides," *Nat. Commun.* **8**, 2098 (2017).
56. C. Wang et al., "Second harmonic generation in nano-structured thin-film lithium niobate waveguides," *Opt. Express* **25**(6), 6963–6973 (2017).
57. R. Luo et al., "Highly tunable efficient second-harmonic generation in a lithium niobate nanophotonic waveguide," *Optica* **5**(8), 1006–1011 (2018).
58. C. Wang et al., "Ultrahigh-efficiency wavelength conversion in nanophotonic periodically poled lithium niobate waveguides," *Optica* **5**(11), 1438–1441 (2018).
59. A. Boes et al., "Improved second harmonic performance in periodically poled LNOI waveguides through engineering of lateral leakage," *Opt. Express* **27**(17), 23919–23928 (2019).
60. J.-Y. Chen et al., "Ultra-efficient frequency conversion in quasi-phase-matched lithium niobate microrings," *Optica* **6**(9), 1244–1245 (2019).
61. J.-Y. Chen et al., "Efficient parametric frequency conversion in lithium niobate nanophotonic chips," *OSA Continuum* **2**(10), 2914–2924 (2019).
62. J. Lin et al., "Broadband quasi-phase-matched harmonic generation in an on-chip monocrystalline lithium niobate microdisk resonator," *Phys. Rev. Lett.* **122**(17), 173903 (2019).
63. J. Lu et al., "Periodically poled thin-film lithium niobate microring resonators with a second-harmonic generation efficiency of 250,000%/W," *Optica* **6**(12), 1455–1460 (2019).
64. M. Jankowski et al., "Ultrabroadband nonlinear optics in nanophotonic periodically poled lithium niobate waveguides," *Optica* **7**(1), 40–46 (2020).
65. Y. Niu et al., "Optimizing the efficiency of a periodically poled LNOI waveguide using in situ monitoring of the ferroelectric domains," *Appl. Phys. Lett.* **116**(10), 101104 (2020).
66. B. Mu et al., "Locally periodically poled LNOI ridge waveguide for second harmonic generation," *Chin. Opt. Lett.* **19**(6), 060007 (2021).
67. R. V. Roussev et al., "Periodically poled lithium niobate waveguide sum-frequency generator for efficient single-photon detection at communication wavelengths," *Opt. Lett.* **29**(13), 1518–1520 (2004).
68. X. Ye et al., "Sum-frequency generation in lithium-niobate-on-insulator microdisk via modal phase matching," *Opt. Lett.* **45**(2), 523–526 (2020).
69. K. Sasagawa and M. Tsuchiya, "Highly efficient third harmonic generation in a periodically poled MgO:LiNbO<sub>3</sub> disk resonator," *Appl. Phys. Express* **2**(12), 122401 (2009).
70. L. Ledezma et al., "Intense optical parametric amplification in dispersion-engineered nanophotonic lithium niobate waveguides," *Optica* **9**(3), 303–308 (2022).
71. J. Lu et al., "Ultralow-threshold thin-film lithium niobate optical parametric oscillator," *Optica* **8**(4), 539–544 (2021).
72. M. Leidinger et al., "Strong forward-backward asymmetry of stimulated Raman scattering in lithium-niobate-based whispering gallery resonators," *Opt. Lett.* **41**(12), 2823–2826 (2016).
73. M. Yu et al., "Raman lasing and soliton mode-locking in lithium niobate microresonators," *Light Sci. Appl.* **9**(1), 9 (2020).
74. Z. Gong et al., "Soliton microcomb generation at 2 μm in z-cut lithium niobate microring resonators," *Opt. Lett.* **44**(12), 3182–3185 (2019).
75. Y. He et al., "Self-starting bi-chromatic LiNbO<sub>3</sub> soliton microcomb," *Optica* **6**(9), 1138–1144 (2019).
76. C. Wang et al., "Monolithic lithium niobate photonic circuits for Kerr frequency comb generation and modulation," *Nat. Commun.* **10**, 978 (2019).
77. M. Zhang et al., "Broadband electro-optic frequency comb generation in a lithium niobate microring resonator," *Nature* **568**(7752), 373–377 (2019).
78. J. Lu et al., "Octave-spanning supercontinuum generation in nanoscale lithium niobate waveguides," *Opt. Lett.* **44**(6), 1492–1495 (2019).

79. M. Yu et al., “Coherent two-octave-spanning supercontinuum generation in lithium-niobate waveguides,” *Opt. Lett.* **44**(5), 1222–1225 (2019).
80. S. Tanzilli et al., “PPLN waveguide for quantum communication,” *Eur. Phys. J. D* **18**(2), 155–160 (2002).
81. Z. Ma et al., “Ultrabright quantum photon sources on chip,” *Phys. Rev. Lett.* **125**(26), 263602 (2020).
82. J. Zhao et al., “High quality entangled photon pair generation in periodically poled thin-film lithium niobate waveguides,” *Phys. Rev. Lett.* **124**(16), 163603 (2020).
83. G.-T. Xue et al., “Ultrabright multiplexed energy-time-entangled photon generation from lithium niobate on insulator chip,” *Phys. Rev. Appl.* **15**(6), 064059 (2021).
84. W. B. Tiffany, “Introduction and review of pyroelectric detectors,” *Proc. SPIE* **0062**, 153–158 (1976).
85. X. Liu et al., “Highly efficient thermo-optic tunable microring resonator based on an LNOI platform,” *Opt. Lett.* **45**(22), 6318–6321 (2020).
86. G. Chen et al., “Integrated thermally tuned mach-zehnder interferometer in Z-cut lithium niobate thin film,” *IEEE Photonics Technol. Lett.* **33**(13), 664–667 (2021).
87. G. Chen, H.-L. Lin, and A. Danner, “Highly efficient thermal tuning interferometer in lithium niobate thin film using air bridge,” *IEEE Photonics J.* **13**(3), 6600409 (2021).
88. M. Xu et al., “High-performance coherent optical modulators based on thin-film lithium niobate platform,” *Nat. Commun.* **11**, 3911 (2020).
89. E. S. Magden et al., “Frequency domain spectroscopy in rare-earth-doped gain media,” *IEEE J. Sel. Top. Quantum Electron.* **24**(5), 3000110 (2018).
90. M. Xin et al., “Optical frequency synthesizer with an integrated erbium tunable laser,” *Light Sci. Appl.* **8**(1), 122 (2019).
91. W. Sohler, “Rare earth doped LiNbO<sub>3</sub> waveguide amplifiers and lasers,” in *Waveguide Optoelectronics*, J. H. Marsh and R. M. De La Rue, Eds., pp. 361–394, Springer, Dordrecht (1992).
92. Z. Chen et al., “Efficient erbium-doped thin-film lithium niobate waveguide amplifiers,” *Opt. Lett.* **46**(5), 1161–1164 (2021).
93. Z. Wang et al., “On-chip tunable microdisk laser fabricated on Er<sup>3+</sup>-doped lithium niobate on insulator,” *Opt. Lett.* **46**(2), 380–383 (2021).
94. S. Dutta et al., “Integrated photonic platform for rare-earth ions in thin film lithium niobate,” *Nano Lett.* **20**(1), 741–747 (2020).
95. S. Wang et al., “Incorporation of erbium ions into thin-film lithium niobate integrated photonics,” *Appl. Phys. Lett.* **116**(15), 151103 (2020).
96. M. Armenise, “Fabrication techniques of lithium niobate waveguides,” *IEE Proc.* **135**(2), 85–91 (1988).
97. I. Kaminow and J. Carruthers, “Optical waveguiding layers in LiNbO<sub>3</sub> and LiTaO<sub>3</sub>,” *Appl. Phys. Lett.* **22**(7), 326–328 (1973).
98. J. Noda et al., “Electro-optic amplitude modulation using three-dimensional LiNbO<sub>3</sub> waveguide fabricated by TiO<sub>2</sub> diffusion,” *Appl. Phys. Lett.* **27**(1), 19–21 (1975).
99. J. R. Carruthers, I. P. Kaminow, and L. W. Stulz, “Diffusion kinetics and optical waveguiding properties of outdiffused layers in lithium niobate and lithium tantalate,” *Appl. Opt.* **13**(10), 2333–2342 (1974).
100. R. L. Holman, P. J. Cressman, and J. F. Revelli, “Chemical control of optical damage in lithium niobate,” *Appl. Phys. Lett.* **32**(5), 280–283 (1978).
101. G. D. Boyd, R. V. Schmidt, and F. Storz, “Characteristics of metal-diffused LiNbO<sub>3</sub> for acoustic devices,” *J. Appl. Phys.* **48**(7), 2880–2881 (1977).
102. M. Fukuma, J. Noda, and H. Iwasaki, “Optical properties in titanium-diffused LiNbO<sub>3</sub> strip waveguides,” *J. Appl. Phys.* **49**(7), 3693–3698 (1978).
103. M. Minakata et al., “Precise determination of refractive-index changes in Ti-diffused LiNbO<sub>3</sub> optical waveguides,” *J. Appl. Phys.* **49**(9), 4677–4682 (1978).
104. J. Campbell, “Coupling of fibers to Ti-diffused LiNbO<sub>3</sub> waveguides by butt-joining,” *Appl. Opt.* **18**(12), 2037–2040 (1979).
105. A. Neyer and W. Sohler, “High-speed cutoff modulator using a Ti-diffused LiNbO<sub>3</sub> channel waveguide,” *Appl. Phys. Lett.* **35**(3), 256–258 (1979).
106. M. Feit, J. Fleck, and L. McCaughan, “Comparison of calculated and measured performance of diffused channel-waveguide couplers,” *J. Opt. Soc. Am.* **73**(10), 1296–1304 (1983).
107. J. Ctyroky et al., “3-D analysis of LiNbO<sub>3</sub>:Ti channel waveguides and directional couplers,” *IEEE J. Quantum Electron.* **20**(4), 400–409 (1984).
108. P.-K. Wei and W.-S. Wang, “A TE-TM mode splitter on lithium niobate using Ti, Ni, and MgO diffusions,” *IEEE Photonics Technol. Lett.* **6**(2), 245–248 (1994).
109. W.-L. Chen et al., “Lithium niobate ridge waveguides by nickel diffusion and proton-exchanged wet etching,” *IEEE Photonics Technol. Lett.* **7**(11), 1318–1320 (1995).
110. Y.-P. Liao et al., “Nickel-diffused lithium niobate optical waveguide with process-dependent polarization,” *IEEE Photonics Technol. Lett.* **8**(4), 548–550 (1996).
111. R. Nevado and G. Lifante, “Characterization of index profiles of Zn-diffused LiNbO<sub>3</sub> waveguides,” *J. Opt. Soc. Am. A* **16**(10), 2574–2580 (1999).
112. D. Ciplys et al., “Guided-wave acousto-optic diffraction in Zn:LiNbO<sub>3</sub>,” *Electron. Lett.* **42**(22), 1294–1295 (2006).
113. M. Fukuma and J. Noda, “Optical properties of titanium-diffused LiNbO<sub>3</sub> strip waveguides and their coupling-to-a-fiber characteristics,” *Appl. Opt.* **19**(4), 591–597 (1980).
114. W. Minford, S. Korotky, and R. Alferness, “Low-loss Ti:LiNbO<sub>3</sub> waveguide bends at  $\lambda = 1.3 \mu\text{m}$ ,” *IEEE J. Quantum Electron.* **18**(10), 1802–1806 (1982).
115. D. White et al., “Atomically-thin quantum dots integrated with lithium niobate photonic chips,” *Opt. Mater. Express* **9**(2), 441–448 (2019).
116. G. Sia et al., “Fabrication and characterization of proton-exchanged waveguide on x-cut LiNbO<sub>3</sub>,” in *IEEE Photonics Global@Singapore*, IEEE (2008).
117. K. Ito and K. Kawamoto, “Dependence of lattice constant deviation and refractive index on proton concentration in proton-exchanged optical waveguides on a single crystal of LiNbO<sub>3</sub>,” *Jpn. J. Appl. Phys.* **31**, 3882–3887 (1992).
118. V. M. Passaro et al., “LiNbO<sub>3</sub> optical waveguides formed in a new proton source,” *J. Lightwave Technol.* **20**(1), 71–77 (2002).
119. W. J. Liao et al., “Proton-exchanged optical waveguides fabricated by glutaric acid,” *Opt. Laser Technol.* **36**(8), 603–606 (2004).
120. T. Fujiwara et al., “Comparison of photorefractive index change in proton-exchanged and Ti-diffused LiNbO<sub>3</sub> waveguides,” *Opt. Lett.* **18**(5), 346–348 (1993).
121. L. Cai, Y. Kang, and H. Hu, “Electric-optical property of the proton exchanged phase modulator in single-crystal lithium niobate thin film,” *Opt. Express* **24**(5), 4640–4647 (2016).
122. P. Suchoski, T. K. Findakly, and F. Leonberger, “Stable low-loss proton-exchanged LiNbO<sub>3</sub> waveguide devices with no electro-optic degradation,” *Opt. Lett.* **13**(11), 1050–1052 (1988).
123. S. T. Vohra, A. R. Mickelson, and S. E. Asher, “Diffusion characteristics and waveguiding properties of proton-exchanged and annealed LiNbO<sub>3</sub> channel waveguides,” *J. Appl. Phys.* **66**(11), 5161–5174 (1989).
124. J. Rams, F. Agullo-Rueda, and J. Cabrera, “Structure of high index proton exchange LiNbO<sub>3</sub> waveguides with undegraded nonlinear optical coefficients,” *Appl. Phys. Lett.* **71**(23), 3356–3358 (1997).
125. O. Stepanenko et al., “Highly confining proton exchanged waveguides on Z-cut LiNbO<sub>3</sub> with preserved nonlinear coefficient,” *IEEE Photonics Technol. Lett.* **26**(15), 1557–1560 (2014).
126. L. Cai et al., “Channel waveguides and y-junctions in x-cut single-crystal lithium niobate thin film,” *Opt. Express* **23**(22), 29211–29221 (2015).

127. M. L. Shah, "Optical waveguides in LiNbO<sub>3</sub> by ion exchange technique," *Appl. Phys. Lett.* **26**(11), 652–653 (1975).
128. J. Jackel, "High- $\Delta n$  optical waveguides in LiNbO<sub>3</sub>:thallium-lithium ion exchange," *Appl. Phys. Lett.* **37**(8), 739–741 (1980).
129. Y. X. Chen et al., "Characterization of LiNbO<sub>3</sub> waveguides exchanged in TiNO<sub>3</sub> solution," *Appl. Phys. Lett.* **40**(1), 10–12 (1982).
130. J. L. Jackel and C. Rice, "Variation in waveguides fabricated by immersion of LiNbO<sub>3</sub> in AgNO<sub>3</sub> and TiNO<sub>3</sub>: the role of hydrogen," *Appl. Phys. Lett.* **41**(6), 508–510 (1982).
131. M. Zhang et al., "Electro-optic reconfigurable two-mode (de-)multiplexer on thin-film lithium niobate," *Opt. Lett.* **46**(5), 1001–1004 (2021).
132. G. Destefanis, P. Townsend, and J. Gailliard, "Optical waveguides in LiNbO<sub>3</sub> formed by ion implantation of helium," *Appl. Phys. Lett.* **32**(5), 293–294 (1978).
133. G. Destefanis et al., "The formation of waveguides and modulators in LiNbO<sub>3</sub> by ion implantation," *J. Appl. Phys.* **50**(12), 7898–7905 (1979).
134. G. Destefanis, J. Gailliard, and P. Townsend, "Optical waveguides in LiNbO<sub>3</sub> formed by ion implantation," *Radiat. Eff.* **48**(1-4), 63–67 (1980).
135. H. Karge et al., "Radiation damage and refractive index of ion-implanted LiNbO<sub>3</sub>," *Nucl. Instrum. Methods* **182–183**(Part 2), 777–780 (1981).
136. S. Al-Chalabi, "Transient annealing of planar waveguides formed by <sup>4</sup>He<sup>+</sup> ion implantation into LiNbO<sub>3</sub>," *Radiat. Eff.* **98**(1-4), 227–231 (1986).
137. I. Skinner et al., "The modelling of lithium outdiffusion in He<sup>+</sup> implanted optical waveguides in LiNbO<sub>3</sub>," *Solid-State Electron.* **30**(1), 85–88 (1987).
138. G. Si et al., "Suspended slab and photonic crystal waveguides in lithium niobate," *J. Vac. Sci. Technol. B* **28**(2), 316–320 (2010).
139. G. Griffel, S. Ruschin, and N. Croitoru, "Linear electro-optic effect in sputtered polycrystalline LiNbO<sub>3</sub> films," *Appl. Phys. Lett.* **54**(15), 1385–1387 (1989).
140. D. K. Fork and G. B. Anderson, "Epitaxial MgO on GaAs(111) as a buffer layer for z-cut epitaxial lithium niobate," *Appl. Phys. Lett.* **63**(8), 1029–1031 (1993).
141. Y. Sakashita and H. Segawa, "Preparation and characterization of LiNbO<sub>3</sub> thin films produced by chemical-vapor deposition," *J. Appl. Phys.* **77**(11), 5995–5999 (1995).
142. M. Levy et al., "Fabrication of single-crystal lithium niobate films by crystal ion slicing," *Appl. Phys. Lett.* **73**(16), 2293–2295 (1998).
143. A. Radojevic et al., "Large etch-selectivity enhancement in the epitaxial liftoff of single-crystal LiNbO<sub>3</sub> films," *Appl. Phys. Lett.* **74**(21), 3197–3199 (1999).
144. T. A. Ramadan, M. Levy, and R. Osgood Jr., "Electro-optic modulation in crystal-ion-sliced z-cut LiNbO<sub>3</sub> thin films," *Appl. Phys. Lett.* **76**(11), 1407–1409 (2000).
145. P. Rabiei and P. Gunter, "Optical and electro-optical properties of submicrometer lithium niobate slab waveguides prepared by crystal ion slicing and wafer bonding," *Appl. Phys. Lett.* **85**(20), 4603–4605 (2004).
146. G. Poberaj et al., "Ion-sliced lithium niobate thin films for active photonic devices," *Opt. Mater.* **31**(7), 1054–1058 (2009).
147. T. Volk and M. Wöhlecke, *Lithium Niobate: Defects, Photorefractive and Ferroelectric Switching*, Vol. **115**, Springer Science and Business Media, Springer-Verlag, Berlin (2008).
148. M. Chauvet et al., "High efficiency frequency doubling in fully diced LiNbO<sub>3</sub> ridge waveguides on silicon," *J. Opt.* **18**(8), 085503 (2016).
149. M. Bock et al., "Highly efficient heralded single-photon source for telecom wavelengths based on a PPLN waveguide," *Opt. Express* **24**(21), 23992–24001 (2016).
150. A. S. Kowligy et al., "Mid-infrared frequency comb generation via cascaded quadratic nonlinearities in quasi-phase-matched waveguides," *Opt. Lett.* **43**(8), 1678–1681 (2018).
151. L. Lehmann et al., "Single photon MIR upconversion detector at room temperature with a PPLN ridge waveguide," *Opt. Express* **27**(14), 19233–19241 (2019).
152. R. Bege et al., "Watt-level second-harmonic generation at 589 nm with a PPMgO:LN ridge waveguide crystal pumped by a DBR tapered diode laser," *Opt. Lett.* **41**(7), 1530–1533 (2016).
153. V. Pecheur et al., "Watt-level SHG in undoped high step-index PPLN ridge waveguides," *OSA Continuum* **4**(5), 1404–1414 (2021).
154. S. A. Berry et al., "Zn-indiffused diced ridge waveguides in MgO:PPLN generating 1 watt 780 nm SHG at 70% efficiency," *OSA Continuum* **2**(12), 3456–3464 (2019).
155. M. E. Solmaz et al., "Vertically integrated As<sub>2</sub>S<sub>3</sub> ring resonator on LiNbO<sub>3</sub>," *Opt. Lett.* **34**(11), 1735–1737 (2009).
156. Y. S. Lee et al., "Hybrid Si-LiNbO<sub>3</sub> microring electro-optically tunable resonators for active photonic devices," *Opt. Lett.* **36**(7), 1119–1121 (2011).
157. L. Chen and R. M. Reano, "Compact electric field sensors based on indirect bonding of lithium niobate to silicon microrings," *Opt. Express* **20**(4), 4032–4038 (2012).
158. P. Rabiei et al., "Heterogeneous lithium niobate photonics on silicon substrates," *Opt. Express* **21**(21), 25573–25581 (2013).
159. L. Cao et al., "Hybrid amorphous silicon (a-Si:H)-LiNbO<sub>3</sub> electro-optic modulator," *Opt. Commun.* **330**, 40–44 (2014).
160. L. Chen et al., "Hybrid silicon and lithium niobate electro-optical ring modulator," *Optica* **1**(2), 112–118 (2014).
161. F. Bo et al., "Lithium-niobate-silica hybrid whispering-gallery-mode resonators," *Adv. Mater.* **27**(48), 8075–8081 (2015).
162. S. Jin et al., "LiNbO<sub>3</sub> thin-film modulators using silicon nitride surface ridge waveguides," *IEEE Photonics Technol. Lett.* **28**(7), 736–739 (2016).
163. S. Li et al., "Waveguides consisting of single-crystal lithium niobate thin film and oxidized titanium stripe," *Opt. Express* **23**(19), 24212–24219 (2015).
164. A. Rao et al., "Heterogeneous microring and Mach-Zehnder modulators based on lithium niobate and chalcogenide glasses on silicon," *Opt. Express* **23**(17), 22746–22752 (2015).
165. A. Rao et al., "High-performance and linear thin-film lithium niobate Mach-Zehnder modulators on silicon up to 50 GHz," *Opt. Lett.* **41**(24), 5700–5703 (2016).
166. L. Chang et al., "Heterogeneous integration of lithium niobate and silicon nitride waveguides for wafer-scale photonic integrated circuits on silicon," *Opt. Lett.* **42**(4), 803–806 (2017).
167. J. D. Witmer et al., "High-Q photonic resonators and electro-optic coupling using silicon-on-lithium-niobate," *Sci. Rep.* **7**, 46313 (2017).
168. A. N. R. Ahmed et al., "Subvolt electro-optical modulator on thin-film lithium niobate and silicon nitride hybrid platform," *Opt. Lett.* **45**(5), 1112–1115 (2020).
169. A. N. R. Ahmed et al., "High-efficiency lithium niobate modulator for K band operation," *APL Photonics* **5**(9), 091302 (2020).
170. N. Boynton et al., "A heterogeneously integrated silicon photonic/lithium niobate travelling wave electro-optic modulator," *Opt. Express* **28**(2), 1868–1884 (2020).
171. D. Pohl et al., "An integrated broadband spectrometer on thin-film lithium niobate," *Nat. Photonics* **14**(1), 24–29 (2020).
172. A. A. Sayem et al., "Lithium-niobate-on-insulator waveguide-integrated superconducting nanowire single-photon detectors," *Appl. Phys. Lett.* **116**(15), 151102 (2020).
173. Z. Yu et al., "Photonic integrated circuits with bound states in the continuum," *Optica* **6**(10), 1342–1348 (2019).
174. Y. Yu et al., "Ultralow-loss etchless lithium niobate integrated photonics at near-visible wavelengths," *Adv. Opt. Mater.* **9**(19), 2100060 (2021).
175. G. Chen et al., "Analysis of perovskite oxide etching using argon inductively coupled plasmas for photonics applications," *Nanoscale Res. Lett.* **16**(1), 32 (2021).

176. J. Jian et al., "High-efficiency hybrid amorphous silicon grating couplers for sub-micron-sized lithium niobate waveguides," *Opt. Express* **26**(23), 29651–29658 (2018).
177. Z. Ruan et al., "Metal based grating coupler on a thin-film lithium niobate waveguide," *Opt. Express* **28**(24), 35615–35621 (2020).
178. J. L. Jackel et al., "Reactive ion etching of LiNbO<sub>3</sub>," *Appl. Phys. Lett.* **38**(11), 907–909 (1981).
179. H. Nagata et al., "Growth of crystalline LiF on CF<sub>4</sub> plasma etched LiNbO<sub>3</sub> substrates," *J. Cryst. Growth* **187**(3-4), 573–576 (1998).
180. H. Nagata et al., "Chemical deterioration of Al film prepared on CF<sub>4</sub> plasma-etched LiNbO<sub>3</sub> surface," *J. Mater. Res.* **15**(2), 476–482 (2000).
181. A. Guarino et al., "Electro-optically tunable microring resonators in lithium niobate," *Nat. Photonics* **1**(7), 407–410 (2007).
182. Z. Ren et al., "Etching characteristics of LiNbO<sub>3</sub> in reactive ion etching and inductively coupled plasma," *J. Appl. Phys.* **103**(3), 034109 (2008).
183. S. Benchabane et al., "Highly selective electroplated nickel mask for lithium niobate dry etching," *J. Appl. Phys.* **105**(9), 094109 (2009).
184. H. Hu, R. Ricken, and W. Sohler, "Lithium niobate photonic wires," *Opt. Express* **17**(26), 24261–24268 (2009).
185. J. Deng, G. Si, and A. J. Danner, "Dry etching of LiNbO<sub>3</sub> using inductively coupled plasma," in *Photonics Global Conf.*, IEEE (2010).
186. G. Si et al., "Nanoscale arrays in lithium niobate fabricated by interference lithography and dry etching," *Int. J. Nanosci.* **9**(4), 311–315 (2010).
187. G. Ulliac et al., "Ultra-smooth LiNbO<sub>3</sub> micro and nano structures for photonic applications," *Microelectron. Eng.* **88**(8), 2417–2419 (2011).
188. D. Jun et al., "Deep anisotropic LiNbO<sub>3</sub> etching with SF<sub>6</sub>/Ar inductively coupled plasmas," *J. Vac. Sci. Technol. B* **30**(1), 011208 (2012).
189. C.-M. Chang et al., "A parametric study of ICP-RIE etching on a lithium niobate substrate," in *10th IEEE Int. Conf. Nano/Micro Eng. and Mol. Syst.*, IEEE (2015).
190. G. Ulliac et al., "Argon plasma inductively coupled plasma reactive ion etching study for smooth sidewall thin film lithium niobate waveguide application," *Opt. Mater.* **53**, 1–5 (2016).
191. I. Krasnokutskaya et al., "Ultra-low loss photonic circuits in lithium niobate on insulator," *Opt. Express* **26**(2), 897–904 (2018).
192. M. Zhang et al., "Monolithic ultra-high-*Q* lithium niobate microring resonator," *Optica* **4**(12), 1536–1537 (2017).
193. M. Bahadori et al., "High performance fully etched isotropic microring resonators in thin-film lithium niobate on insulator platform," *Opt. Express* **27**(15), 22025–22039 (2019).
194. A. A. Osipov, S. E. Alexandrov, and G. A. Iankevich, "The effect of a lithium niobate heating on the etching rate in SF<sub>6</sub> ICP plasma," *Mater. Res. Express* **6**(4), 046306 (2019).
195. C. Shen et al., "A comparative study of dry-etching nanophotonic devices on a LiNbO<sub>3</sub>-on-insulator material platform," *Proc. SPIE* **11781**, 117810X (2021).
196. A. A. Osipov et al., "Deep etching of LiNbO<sub>3</sub> using inductively coupled plasma in SF<sub>6</sub>-based gas mixture," *J. Microelectromech. Syst.* **30**(1), 90–95 (2021).
197. H. Liang et al., "High-quality lithium niobate photonic crystal nanocavities," *Optica* **4**(10), 1251–1258 (2017).
198. T. L. Ting, L. Y. Chen, and W. S. Wang, "Wet etching X-cut LiNbO<sub>3</sub> using diluted joint proton source," *Microwave Opt. Technol. Lett.* **48**(10), 2108–2111 (2006).
199. F. Laurell et al., "Wet etching of proton-exchanged lithium niobate—a novel processing technique," *J. Lightwave Technol.* **10**(11), 1606–1609 (1992).
200. H. Lee and S.-Y. Shin, "Lithium niobate ridge waveguides fabricated by wet etching," *Electron. Lett.* **31**(4), 268–269 (1995).
201. R.-S. Cheng, T.-J. Wang, and W.-S. Wang, "Wet-etched ridge waveguides in Y-cut lithium niobate," *J. Lightwave Technol.* **15**(10), 1880–1887 (1997).
202. T.-J. Wang et al., "A novel wet-etching method using electric-field-assisted proton exchange in LiNbO<sub>3</sub>," *J. Lightwave Technol.* **22**(7), 1764–1771 (2004).
203. I. Azanova et al., "Chemical etching technique for investigations of a structure of annealed and unannealed proton exchange channel LiNbO<sub>3</sub> waveguides," *Ferroelectrics* **374**(1), 110–121 (2008).
204. Y. Li et al., "Research of selective etching in LiNbO<sub>3</sub> using proton-exchanged wet etching technique," *Mater. Res. Express* **7**(5), 056202 (2020).
205. H. Hu et al., "Lithium niobate ridge waveguides fabricated by wet etching," *IEEE Photonics Technol. Lett.* **19**(6), 417–419 (2007).
206. L. Wang et al., "Selective etching in LiNbO<sub>3</sub> combined of MeV O and Si ion implantation with wet-etch technique," *Surf. Coat. Technol.* **201**(9-11), 5081–5084 (2007).
207. H. Hartung et al., "Ultra thin high index contrast photonic crystal slabs in lithium niobate," *Opt. Mater.* **33**(1), 19–21 (2010).
208. F. Lacour et al., "Nanostructuring lithium niobate substrates by focused ion beam milling," *Opt. Mater.* **27**(8), 1421–1425 (2005).
209. G. Si et al., "Photonic crystal structures with ultrahigh aspect ratio in lithium niobate fabricated by focused ion beam milling," *J. Vac. Sci. Technol. B* **29**(2), 021205 (2011).
210. R. Geiss et al., "Photonic crystals in lithium niobate by combining focused ion beam writing and ion-beam enhanced etching," *Phys. Stat. Solidi A* **211**(10), 2421–2425 (2014).
211. M. Qu et al., "Homogenous and ultra-shallow lithium niobate etching by focused ion beam," *Precis. Eng.* **62**, 10–15 (2020).
212. N. Courjal et al., "High aspect ratio lithium niobate ridge waveguides fabricated by optical grade dicing," *J. Phys. D Appl. Phys.* **44**(30), 305101 (2011).
213. M. F. Volk et al., "Low loss ridge waveguides in lithium niobate thin films by optical grade diamond blade dicing," *Opt. Express* **24**(2), 1386–1391 (2016).
214. J. Lin et al., "Fabrication of high-*Q* lithium niobate microresonators using femtosecond laser micromachining," *Sci. Rep.* **5**, 8072 (2015).
215. Z. Fang et al., "Fabrication of high quality factor lithium niobate double-disk using a femtosecond laser," *Int. J. Optomechatron.* **11**(1), 47–54 (2017).
216. S. Liu, Y. Zheng, and X. Chen, "Cascading second-order nonlinear processes in a lithium niobate-on-insulator microdisk," *Opt. Lett.* **42**(18), 3626–3629 (2017).
217. M. Wang et al., "On-chip electro-optic tuning of a lithium niobate microresonator with integrated in-plane microelectrodes," *Opt. Express* **25**(1), 124–129 (2017).
218. R. Wu et al., "Lithium niobate micro-disk resonators of quality factors above 10<sup>7</sup>," *Opt. Lett.* **43**(17), 4116–4119 (2018).
219. R. Wu et al., "Long low-loss-lithium niobate on insulator waveguides with sub-nanometer surface roughness," *Nanomaterials* **8**(11), 910 (2018).
220. M. Wang et al., "Chemo-mechanical polish lithography: a pathway to low loss large-scale photonic integration on lithium niobate on insulator," *Quantum Eng.* **1**(1), e9 (2019).
221. J. Zhang et al., "Fabrication of crystalline microresonators of high quality factors with a controllable wedge angle on lithium niobate on insulator," *Nanomaterials* **9**(9), 1218 (2019).
222. Z. Fang et al., "Real-time electrical tuning of an optical spring on a monolithically integrated ultrahigh *Q* lithium niobate microresonator," *Opt. Lett.* **44**(5), 1214–1217 (2019).
223. N. Yao et al., "Efficient light coupling between an ultra-low loss lithium niobate waveguide and an adiabatically tapered single mode optical fiber," *Opt. Express* **28**(8), 12416–12423 (2020).
224. R. Gao et al., "Lithium niobate microring with ultra-high *Q* factor above 10<sup>8</sup>," *Chin. Opt. Lett.* **20**(1), 011902 (2022).

225. X. C. Tong, "Characterization methodologies of optical waveguides," in *Advanced Materials for Integrated Optical Waveguides*, pp. 53–102, Springer, New York City (2014).
226. S. Y. Siew et al., "Rib microring resonators in lithium niobate on insulator," *IEEE Photonics Technol. Lett.* **28**(5), 573–576 (2016).
227. J. Moore et al., "Continuous-wave cascaded-harmonic generation and multi-photon Raman lasing in lithium niobate whispering-gallery resonators," *Appl. Phys. Lett.* **99**(22), 221111 (2011).
228. C. Wang et al., "Integrated high quality factor lithium niobate microdisk resonators," *Opt. Express* **22**(25), 30924–30933 (2014).
229. C. Wang et al., "Integrated lithium niobate nonlinear optical devices," in *Conf. Lasers and Electro-Opt., IEEE* (2015).
230. J. Wang et al., "High- $Q$  lithium niobate microdisk resonators on a chip for efficient electro-optic modulation," *Opt. Express* **23**(18), 23072–23078 (2015).
231. Y. He et al., "Dispersion engineered high quality lithium niobate microring resonators," *Opt. Express* **26**(13), 16315–16322 (2018).
232. L. Ge et al., "Quality improvement and mode evolution of high- $Q$  lithium niobate micro-disk induced by 'light annealing'," *Opt. Mater. Express* **9**(4), 1632–1639 (2019).
233. S. Liu et al., "Effective four-wave mixing in the lithium niobate on insulator microdisk by cascading quadratic processes," *Opt. Lett.* **44**(6), 1456–1459 (2019).
234. L. Zhang et al., "Microdisk resonators with lithium-niobate film on silicon substrate," *Opt. Express* **27**(23), 33662–33669 (2019).
235. Y. Zheng et al., "High- $Q$  exterior whispering-gallery modes in a double-layer crystalline microdisk resonator," *Phys. Rev. Lett.* **122**(25), 253902 (2019).
236. J. Ling et al., "Athermal lithium niobate microresonator," *Opt. Express* **28**(15), 21682–21691 (2020).
237. R. Wang and S. A. Bhave, "Lithium niobate optomechanical disk resonators," in *Joint Conf. IEEE Int. Freq. Control Symp. and Int. Symp. Appl. Ferroelectr.*, IEEE (2020).
238. R. Gao et al., "On-chip ultra-narrow-linewidth single-mode microlaser on lithium niobate on insulator," *Opt. Lett.* **46**(13), 3131–3134 (2021).
239. B. Pan et al., "Compact racetrack resonator on LiNbO<sub>3</sub>," *J. Lightwave Technol.* **39**(6), 1770–1776 (2021).
240. Y. Xu et al., "Mitigating photorefractive effect in thin-film lithium niobate microring resonators," *Opt. Express* **29**(4), 5497–5504 (2021).
241. M. Li et al., "Lithium niobate photonic-crystal electro-optic modulator," *Nat. Commun.* **11**, 4123 (2020).
242. M. Xu et al., "Integrated thin film lithium niobate Fabry–Perot modulator," *Chin. Opt. Lett.* **19**(6), 060003 (2021).
243. D. Pohl et al., "100-GBd waveguide Bragg grating modulator in thin-film lithium niobate," *IEEE Photonics Technol. Lett.* **33**(2), 85–88 (2021).
244. Z. Gong et al., "Optimal design of DC-based polarization beam splitter in lithium niobate on insulator," *Opt. Commun.* **396**, 23–27 (2017).
245. L. Cai and G. Piazza, "Low-loss chirped grating for vertical light coupling in lithium niobate on insulator," *J. Opt.* **21**(6), 065801 (2019).
246. L. He et al., "Low-loss fiber-to-chip interface for lithium niobate photonic integrated circuits," *Opt. Lett.* **44**(9), 2314–2317 (2019).
247. A. Kar et al., "Realization of alignment-tolerant grating couplers for z-cut thin-film lithium niobate," *Opt. Express* **27**(11), 15856–15867 (2019).
248. I. Krasnokutska et al., "High coupling efficiency grating couplers on lithium niobate on insulator," *Opt. Express* **27**(13), 17681–17685 (2019).
249. I. Krasnokutska, J.-L. J. Tambarco, and A. Peruzzo, "Nanostructuring of LNOI for efficient edge coupling," *Opt. Express* **27**(12), 16578–16585 (2019).
250. A. Pan et al., "Fundamental mode hybridization in a thin film lithium niobate ridge waveguide," *Opt. Express* **27**(24), 35659–35669 (2019).
251. Q. Xu et al., "A theoretical study on rib-type photonic wires based on LiNbO<sub>3</sub> thin film on insulator," *Adv. Theor. Simul.* **2**(10), 1900115 (2019).
252. Z. Chen, Y. Ning, and Y. Xun, "Chirped and apodized grating couplers on lithium niobate thin film," *Opt. Mater. Express* **10**(10), 2513–2521 (2020).
253. Z. Gong et al., "Tunable microwave photonic filter based on LNOI polarization beam splitter and waveguide grating," *IEEE Photonics Technol. Lett.* **32**(13), 787–790 (2020).
254. C. C. Kores, M. Fokine, and F. Laurell, "UV-written grating couplers on thin-film lithium niobate ridge waveguides," *Opt. Express* **28**(19), 27839–27849 (2020).
255. Y. Liu et al., "TE/TM-pass polarizers based on lateral leakage in a thin film lithium niobate–silicon nitride hybrid platform," *Opt. Lett.* **45**(17), 4915–4918 (2020).
256. D. Pohl et al., "Tunable Bragg grating filters and resonators in lithium niobate-on-insulator waveguides," in *CLEO: Sci. and Innov.*, Optical Society of America (2020).
257. A. Prencipe, M. A. Baghban, and K. Gallo, "Ultra-narrowband Bragg grating filters in LiNbO<sub>3</sub> on insulator photonic wires," in *Integrated Photonics Res., Silicon and Nanophotonics*, Optical Society of America (2020).
258. G. Qian et al., "Design and fabrication of cantilevered fiber-to-waveguide mode size converter for thin-film lithium niobate photonic integrated circuits," *Proc. SPIE* **11455**, 1145587 (2020).
259. K. Shuting et al., "High-efficiency chirped grating couplers on lithium niobate on insulator," *Opt. Lett.* **45**(24), 6651–6654 (2020).
260. S. Tan et al., "Two-dimensional beam steering based on LNOI optical phased array," in *CLEO: Science and Innov.*, Optical Society of America (2020).
261. H. Xu et al., "Proposal for an ultra-broadband polarization beam splitter using an anisotropy-engineered Mach–Zehnder interferometer on the x-cut lithium-niobate-on-insulator," *Opt. Express* **28**(8), 10899–10908 (2020).
262. L. Zhang, X. Fu, and L. Yang, "Polarization-independent, lithium-niobate-on-insulator directional coupler based on a combined coupling-sections design," *Appl. Opt.* **59**(28), 8668–8673 (2020).
263. J.-X. Zhou et al., "Electro-optically switchable optical true delay lines of meter-scale lengths fabricated on lithium niobate on insulator using photolithography assisted chemo-mechanical etching," *Chin. Phys. Lett.* **37**(8), 8084201 (2020).
264. K. Abdelsalam et al., "Tunable dual-channel ultra-narrowband Bragg grating filter on thin-film lithium niobate," *Opt. Lett.* **46**(11), 2730–2733 (2021).
265. B. Chen et al., "Two-dimensional grating coupler on an X-cut lithium niobate thin-film," *Opt. Express* **29**(2), 1289–1295 (2021).
266. C. Hu et al., "High-efficient coupler for thin-film lithium niobate waveguide devices," *Opt. Express* **29**(4), 5397–5406 (2021).
267. Y. Liu et al., "Ultra-compact mode-division multiplexed photonic integrated circuit for dual polarizations," *J. Lightwave Technol.* **39**(18), 5925–5932 (2021).
268. E. Lomonte, F. Lenzini, and W. H. P. Pernice, "Efficient self-imaging grating couplers on a lithium-niobate-on-insulator platform at near-visible and telecom wavelengths," *Opt. Express* **29**(13), 20205–20216 (2021).
269. S. Yang et al., "Low loss ridge-waveguide grating couplers in lithium niobate on insulator," *Opt. Mater. Express* **11**(5), 1366–1376 (2021).
270. G. Chen, Y. Yu, and X. Zhang, "A dual-detector optical receiver for PDM signals detection," *Sci. Rep.* **6**, 26469 (2016).
271. R. Alferness et al., "Efficient single-mode fiber to titanium diffused lithium niobate waveguide coupling for  $\lambda = 1.32 \mu\text{m}$ ," *IEEE J. Quantum Electron.* **18**(10), 1807–1813 (1982).
272. C. Wang et al., "Nanophotonic lithium niobate electro-optic modulators," *Opt. Express* **26**(2), 1547–1555 (2018).

273. J. Jian et al., "High modulation efficiency lithium niobate Michelson interferometer modulator," *Opt. Express* **27**(13), 18731–18739 (2019).
274. M. Jin et al., "High-extinction electro-optic modulation on lithium niobate thin film," *Opt. Lett.* **44**(5), 1265–1268 (2019).
275. T. Ren et al., "An integrated low-voltage broadband lithium niobate phase modulator," *IEEE Photonics Technol. Lett.* **31**(11), 889–892 (2019).
276. M. Xu et al., "Michelson interferometer modulator based on hybrid silicon and lithium niobate platform," *APL Photonics* **4**(10), 100802 (2019).
277. S. Sun et al., "Bias-drift-free Mach–Zehnder modulators based on a heterogeneous silicon and lithium niobate platform," *Photonics Res.* **8**(12), 1958–1963 (2020).
278. J. Hu et al., "Folded thin-film lithium niobate modulator based on a poled Mach–Zehnder interferometer structure," *Opt. Lett.* **46**(12), 2940–2943 (2021).
279. X. Huang et al., "40 GHz high-efficiency Michelson interferometer modulator on a silicon-rich nitride and thin-film lithium niobate hybrid platform," *Opt. Lett.* **46**(12), 2811–2814 (2021).
280. N. Jagatpal et al., "Thin film lithium niobate electro-optic modulator for 1064 nm wavelength," *IEEE Photonics Technol. Lett.* **33**(5), 271–274 (2021).
281. M. Jin et al., "Efficient electro-optical modulation on thin-film lithium niobate," *Opt. Lett.* **46**(8), 1884–1887 (2021).
282. P. Kharel et al., "Breaking voltage–bandwidth limits in integrated lithium niobate modulators using micro-structured electrodes," *Optica* **8**(3), 357–363 (2021).
283. X. Liu et al., "Low half-wave-voltage, ultra-high bandwidth thin-film LiNbO<sub>3</sub> modulator based on hybrid waveguide and periodic capacitively loaded electrodes," arXiv:2103.03684 (2021).
284. Y. Liu et al., "Low V<sub>π</sub> thin-film lithium niobate modulator fabricated with photolithography," *Opt. Express* **29**(5), 6320–6329 (2021).
285. B. Pan et al., "Demonstration of high-speed thin-film lithium niobate-on-insulator optical modulators at the 2-μm wavelength," *Opt. Express* **29**(12), 17710–17717 (2021).
286. X. Ye et al., "High-speed programmable lithium niobate thin film spatial light modulator," *Opt. Lett.* **46**(5), 1037–1040 (2021).
287. P. Ying et al., "Low-loss edge-coupling thin-film lithium niobate modulator with an efficient phase shifter," *Opt. Lett.* **46**(6), 1478–1481 (2021).
288. G. Chen et al., "Integrated electro-optic modulator in z-cut lithium niobate thin film with vertical structure," *IEEE Photonics Technol. Lett.* **33**(23), 1285–1288 (2021).
289. J. Kondo et al., "40-Gb/s X-cut LiNbO<sub>3</sub> optical modulator with two-step back-slot structure," *J. Lightwave Technol.* **20**(12), 2110–2114 (2002).
290. M. García-Granda et al., "Design and fabrication of novel ridge guide modulators in lithium niobate," *J. Lightwave Technol.* **27**(24), 5690–5697 (2009).
291. H. Lu et al., "Optical and RF characterization of a lithium niobate photonic crystal modulator," *IEEE Photonics Technol. Lett.* **26**(13), 1332–1335 (2014).
292. M. Mahmoud et al., "Lithium niobate electro-optic racetrack modulator etched in Y-cut LNOI platform," *IEEE Photonics J.* **10**(1), 6600410 (2018).
293. Y. Yamaguchi et al., "Experimental evaluation of wavelength-dependence of thin-film LiNbO<sub>3</sub> modulator with an extinction-ratio-tunable structure," in *24th OptoElectron. and Commun. Conf. and Int. Conf. Photonics Switch. and Comput.*, IEEE (2019).
294. M. Xu et al., "Dual-polarization thin-film lithium niobate in-phase quadrature modulators for terabit-per-second transmission," *Optica* **9**(1), 61–62 (2022).
295. X. Zhang et al., "An optical switch based on electro-optic mode deflection in lithium niobate waveguide," *IEEE Photonics Technol. Lett.* **32**(20), 1295–1298 (2020).
296. G. Chen et al., "Design and fabrication of high-performance multimode interferometer in lithium niobate thin film," *Opt. Express* **29**(10), 15689–15698 (2021).
297. X. P. Li, K. X. Chen, and L. F. Wang, "Compact and electro-optic tunable interleaver in lithium niobate thin film," *Opt. Lett.* **43**(15), 3610–3613 (2018).
298. M. Zhang et al., "Electronically programmable photonic molecule," *Nat. Photonics* **13**(1), 36–40 (2019).
299. Y. Hu et al., "On-chip electro-optic frequency shifters and beam splitters," *Nature* **599**(7886), 587–593 (2021).
300. J. Holzgrafe et al., "Cavity electro-optics in thin-film lithium niobate for efficient microwave-to-optical transduction," *Optica* **7**(12), 1714–1720 (2020).
301. T. P. McKenna et al., "Cryogenic microwave-to-optical conversion using a triply resonant lithium niobate-on-sapphire transducer," *Optica* **7**(12), 1737–1745 (2020).
302. Y. Xu et al., "Bidirectional interconversion of microwave and light with thin-film lithium niobate," *Nat. Commun.* **12**, 4453 (2021).
303. A. P. Higginbotham et al., "Harnessing electro-optic correlations in an efficient mechanical converter," *Nat. Phys.* **14**(10), 1038–1042 (2018).
304. L. E. Myers et al., "Quasi-phase-matched optical parametric oscillators in bulk periodically poled LiNbO<sub>3</sub>," *J. Opt. Soc. Am. B* **12**(11), 2102–2116 (1995).
305. G. Li et al., "Broadband sum-frequency generation using d<sub>33</sub> in periodically poled LiNbO<sub>3</sub> thin film in the telecommunications band," *Opt. Lett.* **42**(5), 939–942 (2017).
306. Y. Li et al., "Optical anapole mode in nanostructured lithium niobate for enhancing second harmonic generation," *Nanophotonics* **9**(11), 3575–3585 (2020).
307. S. Kakio et al., "Diffraction properties and beam-propagation analysis of waveguide-type acousto-optic modulator driven by surface acoustic wave," *Jpn. J. Appl. Phys.* **44**(6B), 4472–4476 (2005).
308. M. Kadota et al., "High-frequency lamb wave device composed of MEMS structure using LiNbO<sub>3</sub> thin film and air gap," *IEEE Trans. Ultrason. Ferroelectr. Freq. Control* **57**(11), 2564–2571 (2010).
309. W. C. Jiang and Q. Lin, "Chip-scale cavity optomechanics in lithium niobate," *Sci. Rep.* **6**, 36920 (2016).
310. W. Jiang et al., "Lithium niobate piezo-optomechanical crystals," *Optica* **6**(7), 845–853 (2019).
311. L. Shao et al., "Phononic band structure engineering for high-Q gigahertz surface acoustic wave resonators on lithium niobate," *Phys. Rev. Appl.* **12**(1), 014022 (2019).
312. A. E. Hassanien et al., "Efficient and wideband acousto-optic modulation on thin-film lithium niobate for microwave-to-photonic conversion," *Photonics Res.* **9**(7), 1182–1190 (2021).
313. C. J. Sarabalis et al., "Acousto-optic modulation of a wavelength-scale waveguide," *Optica* **8**(4), 477–483 (2021).
314. R. M. White and F. W. Voltmer, "Direct piezoelectric coupling to surface elastic waves," *Appl. Phys. Lett.* **7**(12), 314–316 (1965).
315. T.-T. Wu et al., "Analysis and design of focused interdigital transducers," *IEEE Trans. Ultrason. Ferroelectr. Freq. Control* **52**(8), 1384–1392 (2005).
316. M. S. Kharusi and G. W. Farnell, "On diffraction and focusing in anisotropic crystals," *Proc. IEEE* **60**(8), 945–956 (1972).
317. Z. Cheng and C. Tsai, "Baseband integrated acousto-optic frequency shifter," *Appl. Phys. Lett.* **60**(1), 12–14 (1992).
318. S. Kakio, "Acousto-optic modulator driven by surface acoustic waves," *Acta Phys. Pol. A* **127**(1), 15–19 (2015).
319. Z. Yu and X. Sun, "Acousto-optic modulation of photonic bound state in the continuum," *Light Sci. Appl.* **9**(1), 1 (2020).
320. Z. Yu and X. Sun, "Gigahertz acousto-optic modulation and frequency shifting on etchless lithium niobate integrated platform," *ACS Photonics* **8**(3), 798–803 (2021).
321. R. Lu et al., "S<sub>0</sub>-mode lithium niobate acoustic delay lines with 1 dB insertion loss," in *IEEE Int. Ultrason. Symp.*, IEEE (2018).

322. R. Lu et al., "Gigahertz low-loss and wideband S0 mode lithium niobate acoustic delay lines," *IEEE Trans. Ultrason. Ferroelectr. Freq. Control* **66**(8), 1373–1386 (2019).
323. R. Lu et al., "GHz broadband SH0 mode lithium niobate acoustic delay lines," *IEEE Trans. Ultrason. Ferroelectr. Freq. Control* **67**(2), 402–412 (2020).
324. R. J. Mears et al., "Low-noise erbium-doped fibre amplifier operating at 1.54  $\mu\text{m}$ ," *Electron. Lett.* **23**(19), 1026–1028 (1987).
325. G. P. Agrawal, *Fiber-Optic Communication Systems*, Vol. **222**, John Wiley and Sons, Hoboken (2010).
326. E. Lallier et al., "Nd:MgO:LiNbO<sub>3</sub> waveguide laser and amplifier," *Opt. Lett.* **15**(12), 682–684 (1990).
327. E. Lallier et al., "Laser oscillation of single-mode channel waveguide in Nd:MgO:LiNbO<sub>3</sub>," *Electron. Lett.* **25**(22), 1491–1492 (1989).
328. I. Baumann et al., "Er-doped integrated optical devices in LiNbO<sub>3</sub>," *IEEE J. Sel. Top. Quantum Electron.* **2**(2), 355–366 (1996).
329. R. Brikmann, W. Sohler, and H. Suche, "Continuous-wave erbium-diffused LiNbO<sub>3</sub> waveguide laser," *Electron. Lett.* **27**(5), 415–417 (1991).
330. Q. Luo et al., "On-chip erbium-doped lithium niobate microring lasers," *Opt. Lett.* **46**(13), 3275–3278 (2021).
331. Y. Liu et al., "On-chip erbium-doped lithium niobate microcavity laser," *SCIENCE CHINA Phys. Mech. Astron.* **64**(3), 234262 (2021).
332. Q. Luo et al., "Microdisk lasers on an erbium-doped lithium-niobate chip," *SCIENCE CHINA Phys. Mech. Astron.* **64**(3), 234263 (2021).
333. Q. Luo et al., "On-chip erbium-doped lithium niobate waveguide amplifiers," *Chin. Opt. Lett.* **19**(6), 060008 (2021).
334. D. Yin et al., "Electro-optically tunable microring laser monolithically integrated on lithium niobate on insulator," *Opt. Lett.* **46**(9), 2127–2130 (2021).
335. C. Op de Beeck et al., "III/V-on-lithium niobate amplifiers and lasers," *Optica* **8**(10), 1288–1289 (2021).
336. H. Guan et al., "Broadband, high-sensitivity graphene photodetector based on ferroelectric polarization of lithium niobate," *Adv. Opt. Mater.* **9**(16), 2100245 (2021).
337. S. Liu and D. Long, "Pyroelectric detectors and materials," *Proc. IEEE* **66**(1), 14–26 (1978).
338. M. Chauvet et al., "Fast-beam self-trapping in LiNbO<sub>3</sub> films by pyroelectric effect," *Opt. Lett.* **40**(7), 1258–1261 (2015).
339. K. K. Gopalan et al., "Mid-infrared pyroresistive graphene detector on LiNbO<sub>3</sub>," *Adv. Opt. Mater.* **5**(4), 1600723 (2017).
340. B. Gao et al., "Lithium niobate metasurfaces," *Laser Photonics Rev.* **13**(5), 1800312 (2019).
341. A. Fedotova et al., "Second-harmonic generation in resonant nonlinear metasurfaces based on lithium niobate," *Nano Lett.* **20**(12), 8608–8614 (2020).
342. L. Carletti et al., "Steering and encoding the polarization of the second harmonic in the visible with a monolithic LiNbO<sub>3</sub> metasurface," *ACS Photonics* **8**(3), 731–737 (2021).
343. J. Ma et al., "Nonlinear lithium niobate metasurfaces for second harmonic generation," *Laser Photonics Rev.* **15**(5), 2000521 (2021).
344. G. Li, S. Zhang, and T. Zentgraf, "Nonlinear photonic metasurfaces," *Nat. Rev. Mater.* **2**(5), 17010 (2017).
345. I. Staude, T. Pertsch, and Y. S. Kivshar, "All-dielectric resonant meta-optics lightens up," *ACS Photonics* **6**(4), 802–814 (2019).
346. L. Wang et al., "Nonlinear wavefront control with all-dielectric metasurfaces," *Nano Lett.* **18**(6), 3978–3984 (2018).
347. J. P. Höpker et al., "Integrated superconducting nanowire single-photon detectors on titanium in-diffused lithium niobate waveguides," *J. Phys. Photonics* **3**(3), 034022 (2021).
348. M. Colangelo et al., "Superconducting nanowire single-photon detector on thin-film lithium niobate photonic waveguide," in *CLEO: Sci. and Innov.*, Optical Society of America (2020).
349. E. Lomonte et al., "Single-photon detection and cryogenic reconfigurability in lithium niobate nanophotonic circuits," *Nat. Commun.* **12**, 6847 (2021).
350. W. H. P. Pernice et al., "High-speed and high-efficiency travelling wave single-photon detectors embedded in nanophotonic circuits," *Nat. Commun.* **3**, 1325 (2012).
351. C. Herzog, G. Poberaj, and P. Günter, "Electro-optic behavior of lithium niobate at cryogenic temperatures," *Opt. Commun.* **281**(4), 793–796 (2008).
352. F. Thiele et al., "Cryogenic electro-optic polarisation conversion in titanium in-diffused lithium niobate waveguides," *Opt. Express* **28**(20), 28961–28968 (2020).
353. G. Chen et al., "Bandwidth improvement for germanium photodetector using wire bonding technology," *Opt. Express* **23**(20), 25700–25706 (2015).
354. G. Chen et al., "Integration of high-speed GaAs metal-semiconductor-metal photodetectors by means of transfer printing for 850 nm wavelength photonic interposers," *Opt. Express* **26**(5), 6351–6359 (2018).
355. K. Luke et al., "Wafer-scale low-loss lithium niobate photonic integrated circuits," *Opt. Express* **28**(17), 24452–24458 (2020).
356. R. Safian et al., "Foundry-compatible thin-film lithium niobate electro-optic modulators," *Proc. SPIE* **11283**, 112832F (2020).
357. A. Y. Piggott et al., "Inverse design and demonstration of a compact and broadband on-chip wavelength demultiplexer," *Nat. Photonics* **9**(6), 374–377 (2015).
358. S. Molesky et al., "Inverse design in nanophotonics," *Nat. Photonics* **12**(11), 659–670 (2018).
359. Y. Shen et al., "Deep learning with coherent nanophotonic circuits," *Nat. Photonics* **11**(7), 441–446 (2017).
360. X. Chen et al., "Single-wavelength and single-photodiode 700 Gb/s entropy-loaded PS-256-QAM and 200-GBaud PS-PAM-16 transmission over 10-km SMF," in *Eur. Conf. Opt. Commun.* (2020).
361. O. Alibart et al., "Quantum photonics at telecom wavelengths based on lithium niobate waveguides," *J. Opt.* **18**(10), 104001 (2016).

**Guanyu Chen** received his PhD in optical engineering from Huazhong University of Science and Technology (HUST), China. During his PhD period, he was as a joint PhD student at Ghent University (UGent), Belgium, with a research focus on silicon photonics. After graduation, he worked as a research fellow at the National University of Singapore (NUS), Singapore, with a research focus on lithium niobate photonics. His current research interests include integrated photonics, high performance optoelectronic devices, and applications in quantum information science and engineering.

**Nanxi Li** is a scientist at Institute of Microelectronics (IME), A\*STAR. He received his BE degree (first class honors) in electrical and electronic engineering from Nanyang Technological University in 2012. In 2013, he started his graduate study at Harvard University, where he received his MS degree in 2015 and his PhD in 2018, both in applied physics. His research interests include silicon photonics, MEMS-based chemical sensors, metasurfaces, and fiber optics.

**Yu Yu** received his PhD from HUST, Wuhan, China, in 2009. From 2009 to 2010, he was with the Centre for Photonic Systems, Department of Engineering, University of Cambridge, Cambridge, United Kingdom, as a research associate. He is currently with the Wuhan National Laboratory for Optoelectronics, HUST, as a professor. His research interests include integrated device and all-optical signal processing.

**Aaron J. Danner** is an associate professor at NUS, Singapore. He received his PhD in electrical engineering from the University of Illinois at Urbana-Champaign, USA. Before joining NUS, he was with Avago Technologies.

Biographies of the other authors are not available.